國立成功大學
太空與電漿科學所
碩士論文

National Cheng Kung University
Institute of Space and Plasma Sciences
Master Thesis

利用脈衝功率系統推動錐形導線陣列產生的電漿噴流之開發

Generation of plasma jets using a conical-wire array driven by a pulsed-power system

研究生 (Author): 謝知叡 Chih-Jui Hsieh

指導老師 (Advisor): 張博宇博士 Dr. Po-Yu Chang

中華民國一百零九年四月 April, 2020

doi:10.6844/NCKU202000512

國立成功大學

碩士論文

利用脈衝功率系統推動錐形導線陣列產生的電漿噴流之開發

Generation of plasma jets using a conical-wire array driven by a pulsed-power system

研究生：謝知叡

本論文業經審查及口試合格特此證明

論文考試委員：陳彥煇 曲宏宇 張博宇

指導教授：張博宇

系(所)主管：陳淑慧

中　華　民　國　109　年　4　月　29　日

摘要

本論文的目標爲在眞空腔中製造超音速電漿噴流來模擬太陽風，其方法爲使用700MW脈衝功率系統，推動錐形導線陣列產生超音速電漿噴流。當超音速電漿噴流流過障礙物時會形成弓形震波，未來會用此方法在實驗室中模擬太陽風流過火星周圍時產生弓形震波的現象。儘管在實驗室中電漿噴流的大小與實際上的太陽風相去甚遠，但定義爲 $v\sqrt{\rho/p}$ 的尤拉數是相仿時，兩流體力學系統是相似的，因此調整適當的實驗參數使其可以在實驗環境中模擬太空的現象。此實驗將會在我們建置的脈衝功率系統上執行，該系統使用了20顆高電壓電容器，總電容值爲5 μF，當充電到20 kV時，系統儲存了1 kJ的能量。爲了量測系統的電流，我們製作了一條帶有積分器的Rogowski線圈。在建立系統過程中，我們執行了一系列的放電測試，其目的爲：測試軌道間隙開關的耐壓、用拾波線圈取得時間基準點，這是用來同步觸發未來會使用的量測儀器、測試打磨後軌道間隙開關的效能以及系統的放電特性。當系統放電時，可產生的電流峰值爲110±20 kA，上升時間爲1.5±0.1 μs的脈衝電流，相對應的系統感值爲150 ± 50 nH。論文最後會使用此脈衝電流來推動錐形導線陣列，在導線陣列中產生電漿噴流，因此我們也建立了一個簡化模型來計算未來所需要的導線的直徑。在未來會以一個X光針孔相機拍攝，此相機的零件已製作完成，下一階段會將此相機組裝完成。因此，在此論文最後是利用一般的相機拍攝噴流在可見光範圍的影像。

關鍵字: 超音速電漿噴流，脈衝功率系統，火星弓形震波，錐形導線陣列

doi:10.6844/NCKU202000512

Abstract

Supersonic plasma jets generated by driving a conical-wire array using an 700 MW pulsed-power system is used to simulate solar winds. A bow shock around an obstacle is formed when the supersonic plasma jet flows around it. It will be used to simulate the Martian bow shock in the laboratory in the future. Even the size of the plasma jet generated in the laboratory is very different from the actual solar wind, the Euler number defined as $v\sqrt{\rho/p}$ is similar between each other showing the hydrodynamic similarity between two systems. Experiments will be conducted on the pulsed-power system we built. The system uses 20 high voltage capacitors with the total capacitance of 5 μF. The whole system is charged to 20 kV storing 1 kJ of energy. A homemade Rogowski coil with the integrator was made for measuring the discharging current. When building the system, varies of discharging experiments were conducted. The purposes were to test the breakdown voltage of the rail-gap switches, to determine the time reference point for synchronizing diagnostics in the future using a pickup coil, to test the discharge performance of the rail-gap switches after polishing, and to characterize the discharge performance. Finally, when the system was discharged, a peak current of 110±20 kA with a rise time of 1.5±0.1 μs was generated. The corresponding system inductance was 150 ± 50 nH. The conical-wire array was then driven by the pulsed current and a plasma jet at the center of the wire array was generated. The wire diameter of the conical-wire array is important and it is estimated by a simplified model. In experiments, an x-ray pinhole camera will be used to take the image of the plasma jet. The components of the x-ray pinhole camera were manufactured and the x-ray pinhole camera will be assembled in the near future. Nevertheless, images taken by a regular camera in visible light of the plasma jet is shown.

Keywords: supersonic plasma jet, pulsed-power system, Martian bow shock, conical wire array

doi:10.6844/NCKU202000512

致謝

能夠來到博宇老師的實驗室真的是我上輩子修來的福氣，覺得每天能和一群對我很好的同伴一起生活真的很開心，從博宇老師身上不僅能學到許多物理與電機方面的知識，而且也能得到許多做人做事的道理，謝謝您在我碰到瓶頸時拉我一把，謝謝您在我忘了做人的細節時提醒了我，謝謝您體諒與理解我和他人格格不入的個性，謝謝您創造了一個如此友善的生活環境。實驗室中，特別感謝我的學長昇樺、名城與國益，感謝你們帶領耐心地帶領我，走過困難重重的實驗前期，讓我學會許多工作的技巧，從生疏直至熟練卻從不嫌我學的慢，後來，你們告訴我關於畢業之後的狀況，也讓我對未來的生涯有初步的看法。感謝對我很好的實驗室夥伴宜霖、宛儀、柏維、彥呈與嘉楷，你們的陪伴是讓我走下去不可或缺的動力，在許多生活小事中堆疊出這片和樂融融的氣氛，讓我心裡感受到甜甜的溫暖。最後要感謝我的家人，謝謝你們一直以來支持我念書，讓我毫無後顧之憂的走向未來，以前，我還是那個愛笑的小孩，後來，變成一個比較孤僻的青少年，現在，我拾起我的笑容，唸完了這個碩士學位，有了你們，才會有這一段故事。

doi:10.6844/NCKU202000512

Contents

doi:10.6844/NCKU202000512

doi:10.6844/NCKU202000512

List of Figures

doi:10.6844/NCKU202000512

doi:10.6844/NCKU202000512

doi:10.6844/NCKU202000512

doi:10.6844/NCKU202000512

doi:10.6844/NCKU202000512

List of Tables

doi:10.6844/NCKU202000512

1 Introduction

When the solar wind, which is a supersonic plasma jet with *Mach* number of 20, comes to Mars, it forms a bow shock at Mars' ionosphere which is called the Martian bow shock. To study this phenomenon in the laboratory, a pulsed-power system with a power of ∼700 MW is used to generate a supersonic plasma jet simulating the solar wind. A conical-wire array is a target that can generate a plasma jet when it is driven by a pulse current of ∼110 kA in the vacuum chamber with the pressure in the order of 10^{-5} torr. The Euler numbers of the Martian bow shock and the plasma jet inside the vacuum chamber are both around 20 showing the hydrodynamic similarity between two systems. Through studying the characteristics of the plasma jet in the laboratory, we can understand the physics of the Martian bow shock.

All of the key components of this thesis is briefly introduced in this chapter. In section 1.1, Martian bow shock will be briefly introduced. In section 1.2, the characteristics of the pulsed-power system that we use will be introduced. Section 1.3 is about diagnostic for measuring the current of the pulsed-power system using Rogowski coil and cameras for taking images of plasma jets. In section 1.4, the conical-wire array which is the target that can generate the plasma jet will be introduced. In section 1.5, the goal and the outline of this thesis will be given.

1.1 The Martian bow shock

In figure 1(a), the solar wind is a plasma stream of energized, charged particles, through the solar system. Mars is an unmagnetized body with an atmosphere. The upper atmosphere is ionized by the extreme ultraviolet (EUV) light from the sun, forming an ionosphere which is the main obstacle to the solar wind. When the supersonic plasma jet flows around the ionosphere, the Martian bow shock is formed at the side toward the sun and outside of the ionosphere of Mars. In figure 1(b), our final goal is to simulate the Martian bow shock in the laboratory. The scaling relation between the Martian bow shock and the laboratory plasma jet will be introduced in chapter 2.[7, 8, 9, 10, 11]

doi:10.6844/NCKU202000512

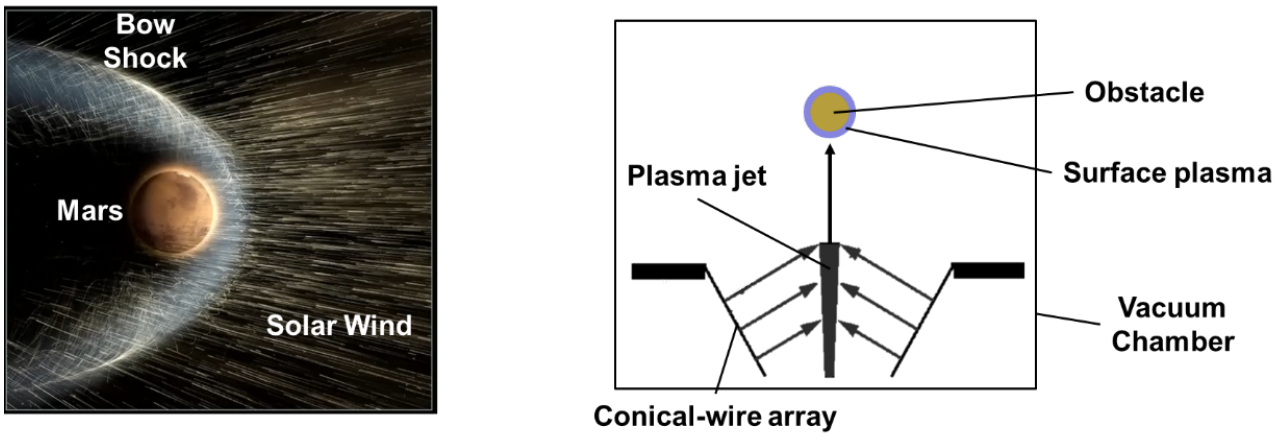

(a) (b)

Figure 1: (a) Martian bow shock. (b) The plasma jet generated by the conical-wire array.

1.2 The pulsed-power system

A pulsed-power system using the parallel-plate capacitor-bank (PPCB) configuration is used to drive the conical-wire array to generate the plasma jet. In figure 2, after the 5 μF capacitor bank is charged to 20 kV storing an energy of 1 kJ, a triggering signal is sent to the system from multistep triggering system which includes a function generator, a slow trigger-pulse generator, and a Marx generator. In addition, the triggering signal will ignite the rail-gap switches on both sides of PPCB simultaneously. Finally, the electrical energy will go through the parallel-plate transmission line into the vacuum chamber where experiments are taken place. The discharge peak current inside the vacuum chamber is 110 $\pm$ 20 kA with a rising time of 1.5 $\pm$ 0.1 μs relative to the triggering pulse and provides a discharge power of $\sim$700MW.[5, 4]

1.3 Diagnostics

To conduct experiments, we developed three diagnostics: (1) a Rogowski coil for measuring the current of the pulsed-power system; (2) a regular camera synchronize with the system for taking image in the visible light region from the plasma jet; and (3) an x-ray pinhole camera for measuring 1-μs time-integrated x-ray images of self-emitted x-rays from the plasma jet.

1.4 Plasma jet generations

A conical-wire array was used to generate the plasma jet for researching the collimated stellar outflows in 2002 by S. V. Lebedev, etc [1]. The dimension of the conical-wire array with

doi:10.6844/NCKU202000512

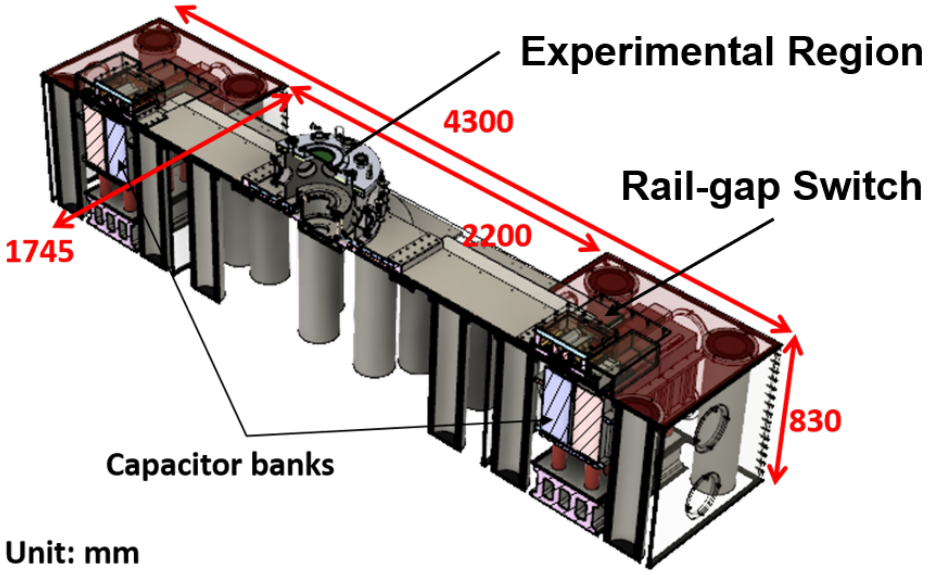

Figure 2: The pulsed-power system using parallel-plate capacitor banks

16 fine wires used in Ref.[1] is shown in figure 3. There are three mechanisms for generating a

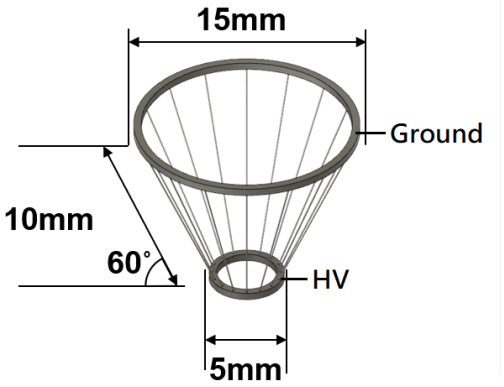

Figure 3: The dimension of the conical-wire array with 16 fine wires by Lebedev[1].

plasma jet from the conical-wire array. Figure 4 shows the explanation of the three mechanisms with the dimension that we use. The dimension that we chose is similar to the one by Lebedev. First, the top ring is at ground and a negative high voltage is applied to the bottom ring. Therefore, a high current goes through the fine wires and heats them into plasma through ohmic heating. Second, a magnetic field is generated by the current. Therefore, the plasma merges toward the center by the J×B force. Third, because the plasma closer to the bottom merges earlier than the one closer to the top, the pressure at the bottom is higher than that at the top. As a result, the plasma flows from the bottom toward the top and forms a plasma jet going upward. The experimental results by Lebedev are shown in figure 5. Different materials

doi:10.6844/NCKU202000512

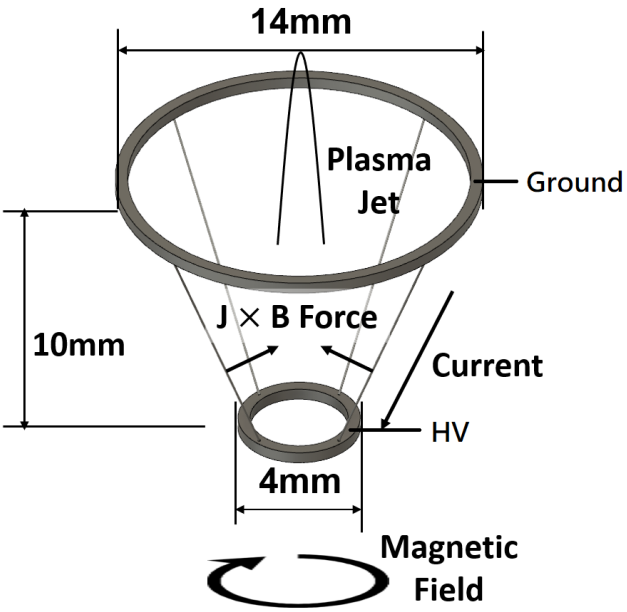

Figure 4: The explanation of the three mechanisms and the dimension of the conical-wire array that we chose.

were used in three different experiments, they were aluminum, iron, and tungsten. Sixteen fine wires were used in all experiments. The plasma jets generated by different metal wires were filmed and shown in figure 5(a). Figure 5(b) shows the plasma jet parameters and the metal wire width. The plasma density is measured around the wires. The density and the velocity of the plasma jets are $\sim 10^{17}$ cm^{-3} and $\sim$ 150 km/sec, respectively.

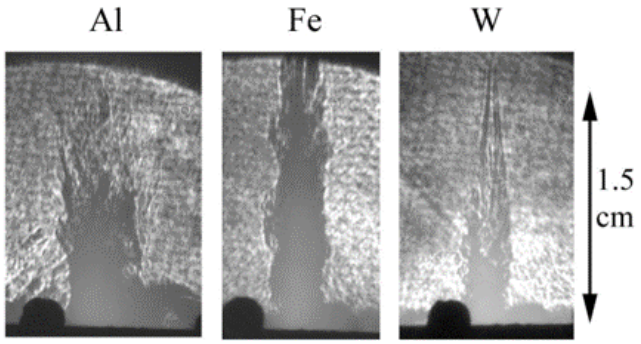

(a)

Fine Wires Number	16 wires
Plasma Density	~ 10^{17} cm^{-3}
Stream Velocity	~ 150 km/s
Metal Wire Width	Al, Fe, W 25, 25, 18μm

(b)

Figure 5: The experiment result by Lebedev.[1]

1.5 The goal and the outline of this thesis

The goal is to finish building the pulsed-power system, design and build the conical-wire array, build the diagnostics, and take an image of the plasma jet. We will show the following results:

doi:10.6844/NCKU202000512

(1) The peak current output of the system is 110±20 kA with a rise time of 1.5 ± 0.1 μs.

(2) The Rogowski coil with a conversion relation of $(2.071 \pm 0.005) \times 10^4$ s/H

(3) A 1-μs high voltage pulse with tunable amplitude from 0.1 to 1 kV for the x-ray pinhole camera

(4) A sychronize imaging system in the visible light,

(5) An image of the plasma jet.

The following thesis is structured as following: Chapter 2 will introduce the physics of the Martian bow shock. The Euler number will be introduced. Chapter 3 will describe the pulsed-power system using the parallel-plate capacitor bank and its performance. Chapter 4 will introduce the diagnostics we built. They are the Rogowski coil, the regular camera, and the x-ray Pinhole camera. Chapter 5 will describe the conical-wire array and how the plasma jet is generated. A simplified model is used to estimate the required wire diameter of the metal wires. Chapter 6 is the future work. Chapter 7 is the summery.

doi:10.6844/NCKU202000512

2 The Martian bow shock

When the solar wind comes to an unmagnetized planet with an atmosphere like Mars, a bow shock at the ionosphere is formed at the side where the solar wind comes. For the case of Mars, it is called the Martian bow shock. The process of the Martian bow shock formation will be introduced in section 2.1. The scaling relation between the solar wind and the plasma jet inside a vacuum chamber will be introduced in section 2.2[7, 8, 9, 10, 11].

2.1 The formation of the Martian bow shock

The solar wind is a plasma stream of energized, charged particles, passing through the solar system. In space, there are three types of interactions between the solar wind and an astronomical object: (1) the solar wind interacts with a magnetized object such as the Earth; (2) the solar wind interacts with an unmagnetized object without the atmosphere such as the Moon; (3) the solar wind interacts with an unmagnetized object with an atmosphere such as Mars. Figure 6 shows the differences between them[2]. In our project, case 3 is considered. Shown in figure 7, the sun emits the solar radiation I_{EUV} which contains extreme ultravoilet (EUV) light[3]. Therefore, the solar radiation excites the neutral molecules into ions and forms the ionosphere. When the solar wind comes to Mars, it exerts the solar wind dynamic pressure $P_{\mathrm{dyn,sw}}$ and the thermal pressure $P_{\mathrm{th,sw}}$ on the ionosphere. In addition, the thermal pressure $P_{\mathrm{th.i}}$ of the ionosphere resists against the solar wind. The ionosphere is formed at the total pressure balance surface, i.e, $P_{\mathrm{dyn,sw}} + P_{\mathrm{th,sw}} = P_{\mathrm{th.i}}$. The Martian bow shock is formed in front of the ionosphere which distance from the Mars center called the Martian bow shock distance.

In figure 6, the red line in the right most figure shows the Martian bow shock distance R_{bs}. The dimensionless terminator distance R_{TD} is defined by the Martian bow shock distance R_{bs} divided by the Mars' radius R_{M}, i.e, $R_{\mathrm{TD}} = \frac{R_{\mathrm{bs}}}{R_{\mathrm{M}}}$. Figure 8(a) shows that the terminator distance R_{TD} is positively correlated with the solar radiation I_{EUV} because the solar radiation can stimulate neutral particles into ions and increase the thermal pressure of the ionosphere $P_{\mathrm{th.i}}$. Besides, figure 8(b) shows the terminator distance R_{TD} is negatively correlated with the dynamic pressure of the solar wind $P_{\mathrm{th.i}}$ because the solar wind with stronger dynamic pressure pushes the ionosphere closer to the Mars surface and the Martian bow shock becomes closer to the Mars surface[11].

doi:10.6844/NCKU202000512

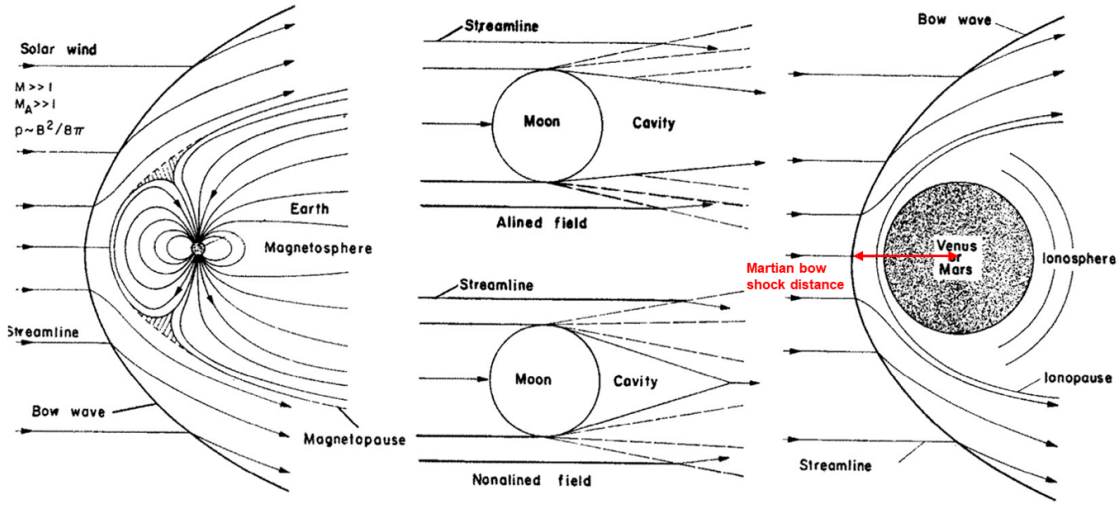

Figure 6: There are three types of the bow shock in the space form by the interaction between the solar wind and astronomical object.[2]

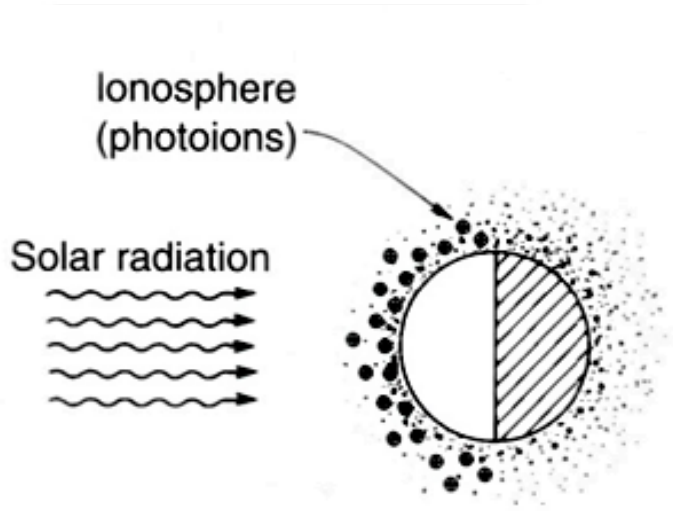

Figure 7: The solar radiation forms the ionosphere of Mars.[3]

2.2 Euler similarity

The reason that the structure of the Martian bow shock can be scaled down from the space to the laboratory is because of the hydrodynamics similarity[7]. The ideal hydrodynamic equations are as follows:

$$\frac{\partial \rho}{\partial t} + \nabla \cdot (\rho \, \vec{v}) = 0 \, , \tag{1}$$

$$\rho(\frac{\partial \vec{v}}{\partial t} + \vec{v} \cdot \nabla v) = -\nabla P \, , \tag{2}$$

doi:10.6844/NCKU202000512

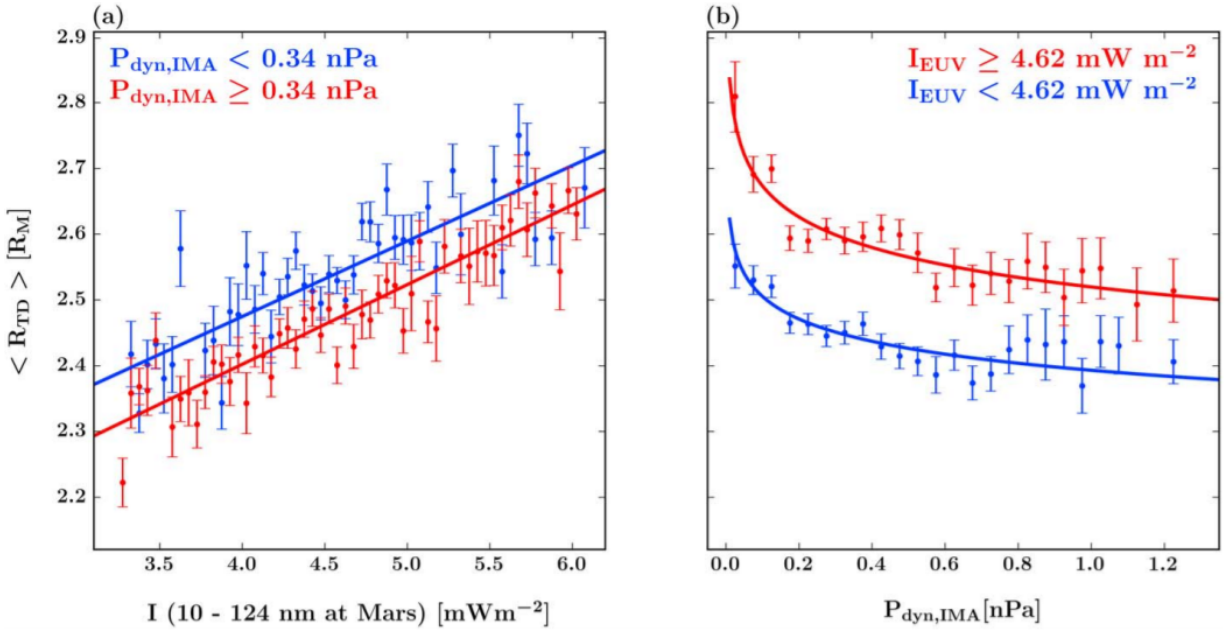

Figure 8: (a) The relation of the terminator distance against solar radiation. (b) The relation of the terminator distance against the dynamic pressure of the solar wind.

$$\frac{\partial P}{\partial t} + \vec{v} \cdot \nabla P = -\gamma \, P \, \nabla \cdot \vec{v} \ . \tag{3}$$

The first equation is the mass conservation. The second equation is the momentum equation for the ideal fluid or Euler equation. The third equation is the entropy conservation equation for a polytropic gas. Suppose two hydrodynamic systems are scalable, one is in the space and the other one is in the laboratory, all hydrodynamic equations remain unchanged under the transformation such that

$$\vec{r}_1 = a\vec{r}_2, \quad \rho_1 = b\rho_2, \quad P_1 = cP_2, \quad t_1 = a\sqrt{\frac{b}{c}}t_2, \quad \vec{v}_1 = \sqrt{\frac{c}{b}}\vec{v}_2 \tag{4}$$

where the subscripts 1 and 2 mean the physical quantities of systems 1 and 2 which refer to the hydrodynamic system in the space and in the laboratory. Consider the initial-value problem in system 1 with the following conditions

$$\rho_1(t=0) = \tilde{\rho}_1 \, f(\vec{r}_1/L_1), \quad P_1(t=0) = \tilde{P}_1 \, g(\vec{r}_1/L_1), \quad \vec{v}_1(t=0) = \tilde{v}_1 \, \vec{h}(\vec{r}_1/L_1), \tag{5}$$

where the $L_1, \tilde{\rho}_1, \tilde{p}_1, \tilde{v}_1$ are the characteristic length, mass density, pressure, velocity, respectively, of the system 1 and f, g, $\vec{h}$ are dimensionless function. On the other hand, the other

doi:10.6844/NCKU202000512

initial conditions for the system 2 are

$$\rho_2(t=0) = \tilde{\rho}_2\, f(\vec{r}_2/L_2), \quad P_2(t=0) = \tilde{P}_2\, g(\vec{r}_2/L_2), \quad \vec{v}_2(t=0) = \tilde{v}_2\, \vec{h}(\vec{r}_2/L_2) \tag{6}$$

where $L_2, \tilde{\rho}_2, \tilde{p}_2, \tilde{v}_2$ are the characteristic length, mass density, pressure, velocity, respectively, of the system 2. According to Eq 4, we get

$$\tilde{v_1}\sqrt{\frac{\tilde{\rho}_1}{\tilde{p}_1}} = \tilde{v_2}\sqrt{\frac{\tilde{\rho}_2}{\tilde{p}_2}} = Eu. \tag{7}$$

where Eu is called the Euler number which is a parameter defined in any systems. The transformation in Eq. 4 holds if two systems have the same value of Euler number $Eu = \tilde{v}\sqrt{\frac{\tilde{\rho}}{\tilde{p}}}$. This similarity is called the Euler similarity. The conclusion is that two hydrodynamic systems behave similarly if they are geometrically similar and their Euler numbers are the same. Table 1 shows the expected physical quantities of hydrodynamic systems in the space and in the laboratory[7, 1, 12]. The Euler numbers in the space and in the laboratory environments are

Table 1: The hydrodynamic quantities of the system in the space and the laboratory.

Physical quantities	Symbol	Value in space	Expected value in the laboratory
Scale height (cm)	r	7×10^8	1×10^{-2}
Drive velocity ($\frac{\mathrm{km}}{\mathrm{s}}$)	v	430	200
Timescale (s)	$\frac{r}{v}$	16	5×10^{-10}
Mass density ($\frac{\mathrm{g}}{\mathrm{cm}^3}$)	ρ	5×10^{-24}	1×10^{-3}
Pressure ($\frac{\mathrm{dyn}}{\mathrm{cm}^2}$)	p	2.5×10^{-11}	8×10^8
Euler number (dimensionless)	$v\sqrt{\frac{\rho}{p}}$	19	22

at the same order. Thus, the two systems will behave similarly based on the Euler similarity. It is the reason why we can study the Martian bow shock in the laboratory.

doi:10.6844/NCKU202000512

3 The pulsed-power system

In order to generate the plasma jet for simulating the solar wind, a pulsed-power system is used to provide the energy. The pulsed-power system has three components: (1) a parallel-plate capacitor bank, (2) a high voltage DC power supply, (3) a multi-step triggering system. The high voltage DC power provides energy that is stored in the parallel-plate capacitor bank. Then the multi-step triggering system sends a trigger pulse to activate the parallel-plate capacitor bank to release the energy to the load for experiments. The first and the second components will be introduced in section 3.1. The third components will be introduced in section 3.2. The discharging tests of the pulsed-power system will be introduced in section 3.3.

3.1 The parallel-plate capacitor bank

The parallel-plate capacitor bank (PPCB) we use is shown in figure 9. It uses 20 high-voltage capacitors and two rail-gap switches. Experiments are performed in the experimental region. The basic unit of the capacitor bank is shown in figure 10 [4]. The capacitance of each capacitor is 1 μF. One brick of capacitors has two capacitors connected in series. Therefore, the capacitance of a single brick of capacitors is 0.5 μF. One wing of the capacitor bank has five brick of capacitors connected in parallel. Therefore, the capacitance of one wing of the capacitor bank is 2.5 μF. The PPCB has two wings connected in parallel. One is called the south wing and the other one is the north wing. Therefore, the total capacitance of the PPCB system is 5 μF. Figure 11 shows the current direction in the pulsed-power system during discharge. First, the capacitor bank will be charged up to 20 kV using the high-voltage power supply (HVPS). When the rail-gap switches are triggered, the electric energy will go through the top plate of the parallel-plate transmission line and goes into the vacuum chamber. Finally, the discharge current will come back to the capacitor bank through the bottom plate of the transmission line. The HVPS will be introduced in section 3.1.1. The rail-gap switch will be introduced in section 3.1.2.

3.1.1 The high-voltage DC power supply

This system provides energy to the capacitor bank. The high-voltage DC power supply system consists of a low voltage power supply[DC-5050A by TAIWAN Power Tech], a pulse

doi:10.6844/NCKU202000512

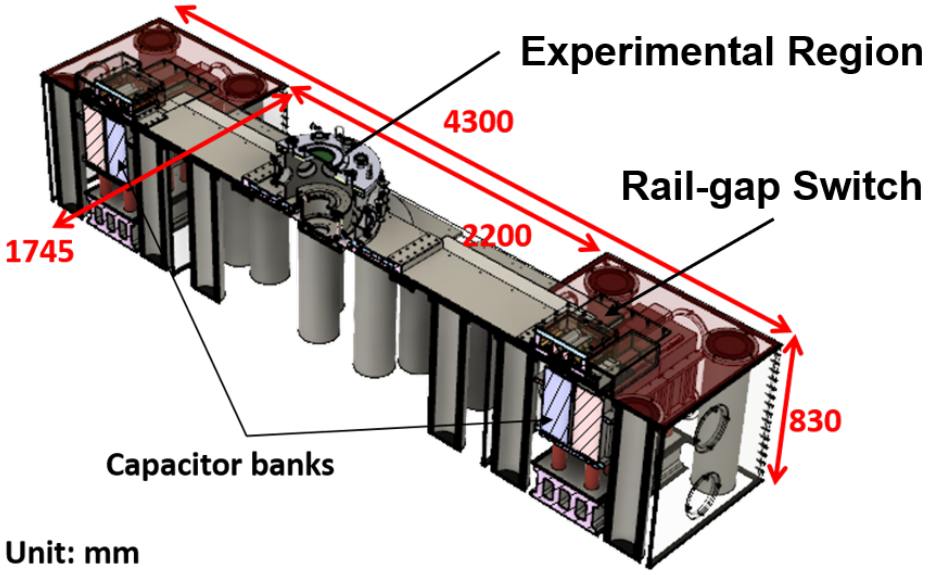

Figure 9: The parallel-plate capacitor banks system.

	The design diagram	Equivalent Circuit	Equivalent parameter
One-Brick capacitor	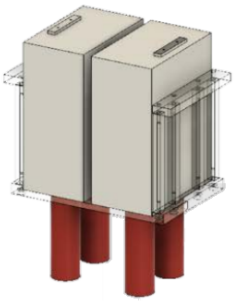	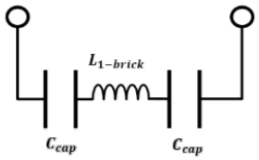	Capacitance: $\frac{C_{cap}}{2} = 0.5\ \mu F$
One wing of capacitor bank	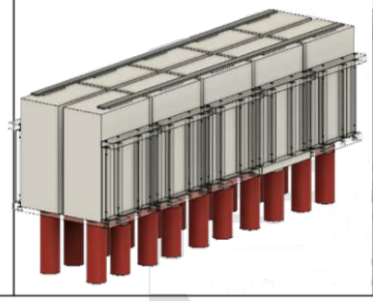	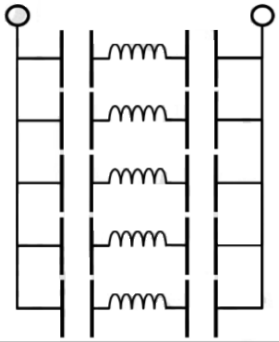	Capacitance: $\frac{C_{cap}}{2} * 5 = 2.5\ \mu F$

Figure 10: The design diagram, circuit diagram, and the capacitance of the one-brick capacitor and one wing of the capacitor bank. Courtesy of [4].

generator[SPIK2000A-03 by Shenchang Electric Co.], a transformer(500-30K-02), and a voltage doubler[5]. The low-voltage power supply provides a DC current with a voltage up to 500V[5]. The pulse generator converts the DC current to AC pulses with the amplitude up to 500V.

doi:10.6844/NCKU202000512

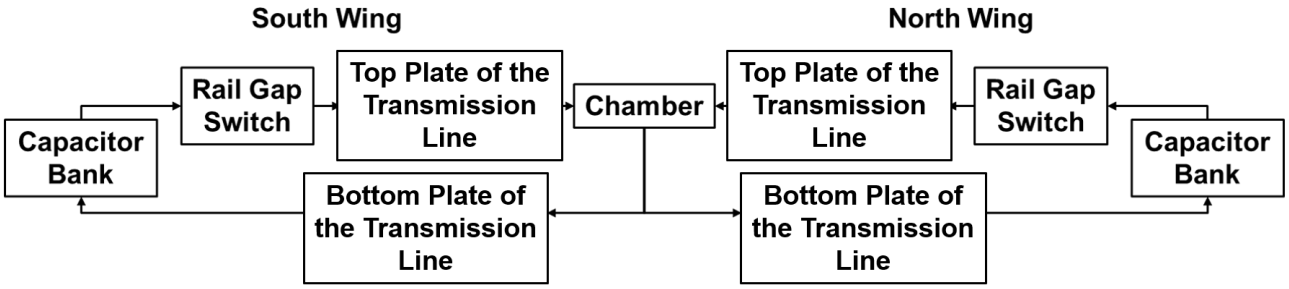

Figure 11: Circuit diagram of the pulsed-power system.

The transformer raises the voltage of the AC pulses with a frequency of 10 kHz 60 times up to 30 kV. The voltage doubler converts the AC current to a DC current with a voltage up to 60 kV. The highest power of the high voltage DC power supply system is 1,500W.

3.1.2 The rail-gap switch

The rail-gap switch is used in the pulsed-power system because of its low inductance. The inductance of the rail-gap switch is 230 ± 10 nH which was measured by the former student Ming-Cheng Jheng[4]. In figure 12(a), the rail-gap switch consists of two rail-like electrodes and a knife-edge electrode in between. One of the rail-like electrodes is connected to the capacitor bank and the other one is connected to the top metal plate of the transmission line. They are called the HV electrode and the grounded electrode, respectively. In figure 12(b), the voltage of the knife-edge electrode is set to one third of the HV by the dividing resistors. During the discharging test done by the former student Ming-Cheng Jheng [4], we found the cylinder edge of the rail-like electrode has the darkest and deepest burn marks in figure 12(c). The reason is as follow: (1) the length of the cylinder part of the rail-like electrodes is 300 mm; (2) the length of the knife-edge electrode is 300 mm; (3) the point pairs A1 and A2, A1 and A3, B1 and B2, and B1 and B3 are aligned together in figure 13; (4) the points A2, A3, B2 and B3 have little bumbs from the machining; and (5) the point discharge effect happened at the place with the most curvature. Therefore, the point-discharge effect happened at the place between the aligned point pairs. Thus, we changed the length of the rail-like electrodes to avoid the aligned point pairs. To decide the length, we calculate the electric field strength around the aligned point pairs by solving the Poisson's equation numerically.

doi:10.6844/NCKU202000512

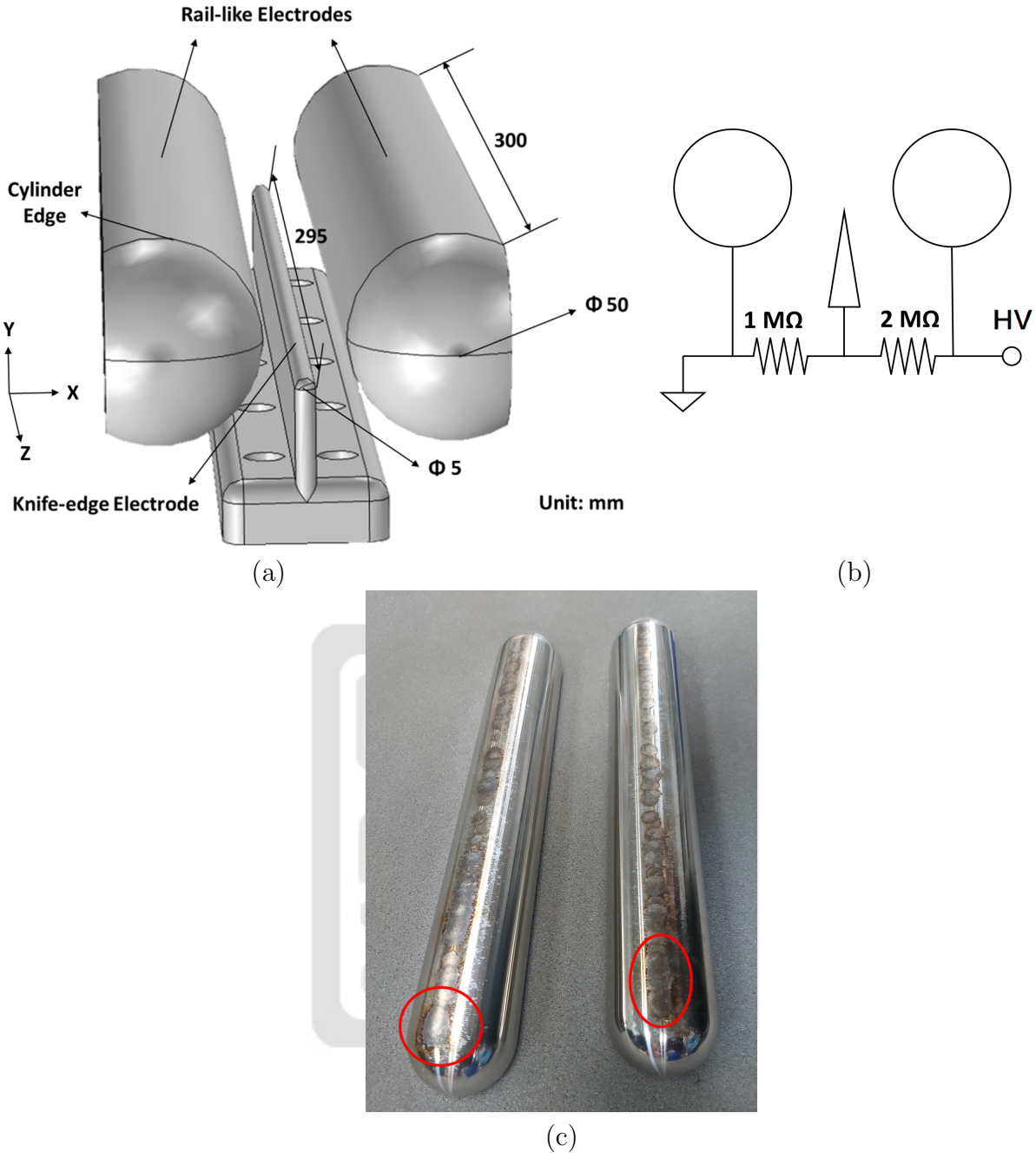

Figure 12: (a) The drawing of the rail-gap switch. (b) The circuit diagram of the dividing resistors for the rail-gap switch. (c) The burn marks of the rail-like electrodes.

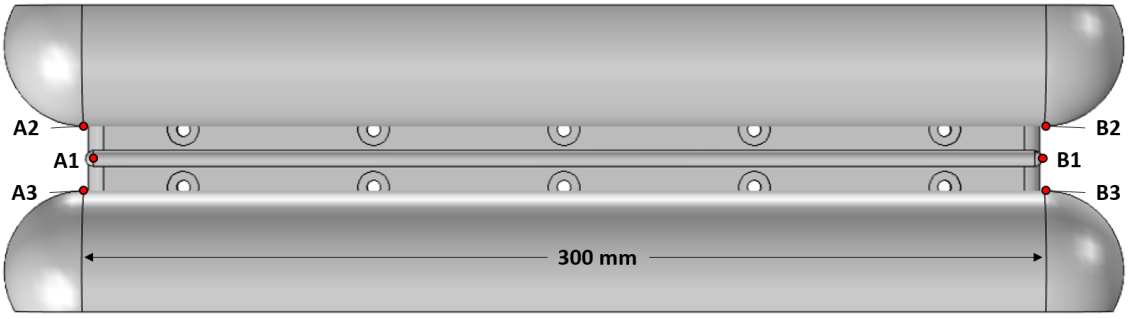

Figure 13: The location of the discharge at the edge of the knife-edge electrode.

doi:10.6844/NCKU202000512

In this simulation, the knife-edge electrode was at the center of the gap. The gap between two rail-like electrodes was set to 20 mm. Figure 14 and 15 shows the electric field strength before and during discharge. In this simulation, the knife-edge electrode was at the center of the gap. The gap between two rail-like electrodes was set to 20 mm. Figure 14 shows the simulated result when HV rail-like electrode is connected to 20 kV which is the charging voltage of the pulsed-power system. The knife-edge electrode is connected to 20/3 kV which is set by the dividing resistors. The minimum distance between the surface of each rail-like electrode and the center of the knife-edge electrode is 10 mm along x-direction. The contour shows the electric field strength in the unit of V/m at the height of points A1 and B1 in figure 13. It shows the electric field strength are strong around the points A1 and B1 due to the point-discharge effect. The stronger the electric field is, the more discharge events will occur. Therefore, the discharge events cause the big burn marks around the points A2, A3, B2, and B3.

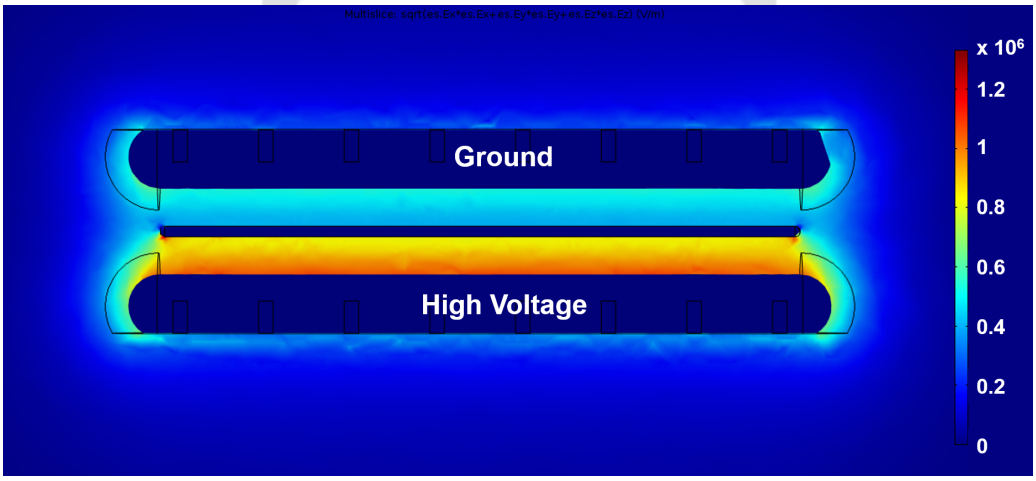

Figure 14: The distribution of the electric field strength before the discharge.

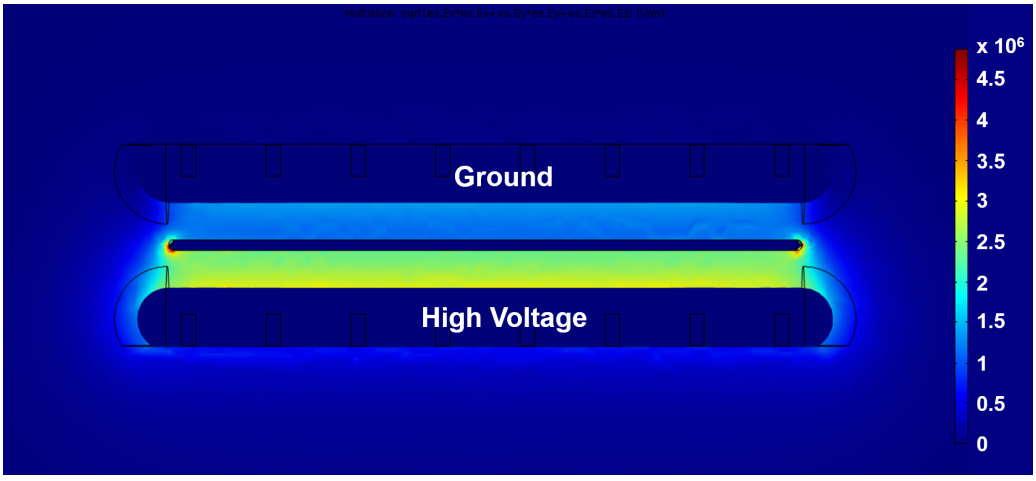

Figure 15: The distribution of the electric field strength during the discharge.

doi:10.6844/NCKU202000512

We would like to change the length of the rail-like electrodes and see how the length effects the strength of the electric field. Intead of changing the length of cylinder in simulations, the knife-edge electrode was moved along the z-direction (figure 12 (a)) in different simulations to mimic changing the length of the rail-like electrodes. In other words, different offsets of the knife-edge electrode along the z-direction were used to represent different lengths of the rail-like electrode. There are two spheres which are shown in white points in figure 16. The one closed to the center is called sphere A and the other one is called sphere B. Diameter of both sphere A and B are both 1 mm. To calculate the influence of the point discharge effect, the electric field strength around edge points of the knife-edge electrode is averaged in those two spheres. In figure 17, the x-axis is the offset relative to the center with the step size of 1 mm and the y-axis is the averaged electric field strength within the spheres. Those with positive x was the average electric field strength calculated in the sphere B. Those with negative x was calculated in the sphere A. In other words, the positive x value means the rail-like electrodes are lengthened and the negative one means the electrodes are shortened. According to the result before the trigger event, we choose the point at half of the maximum which is 25 mm. In other words, we choose to shorten the original rail-like electrode by 25 mm on both sides, that is, to shorten it by 50 mm in total.

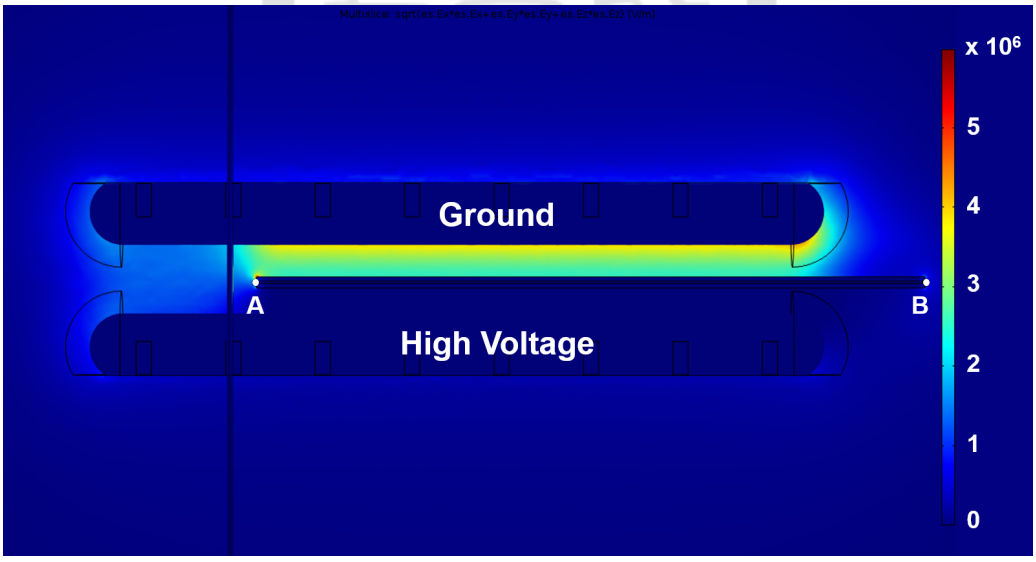

Figure 16: The average electric field strength when the knife-edge electrode moving along the gap.

doi:10.6844/NCKU202000512

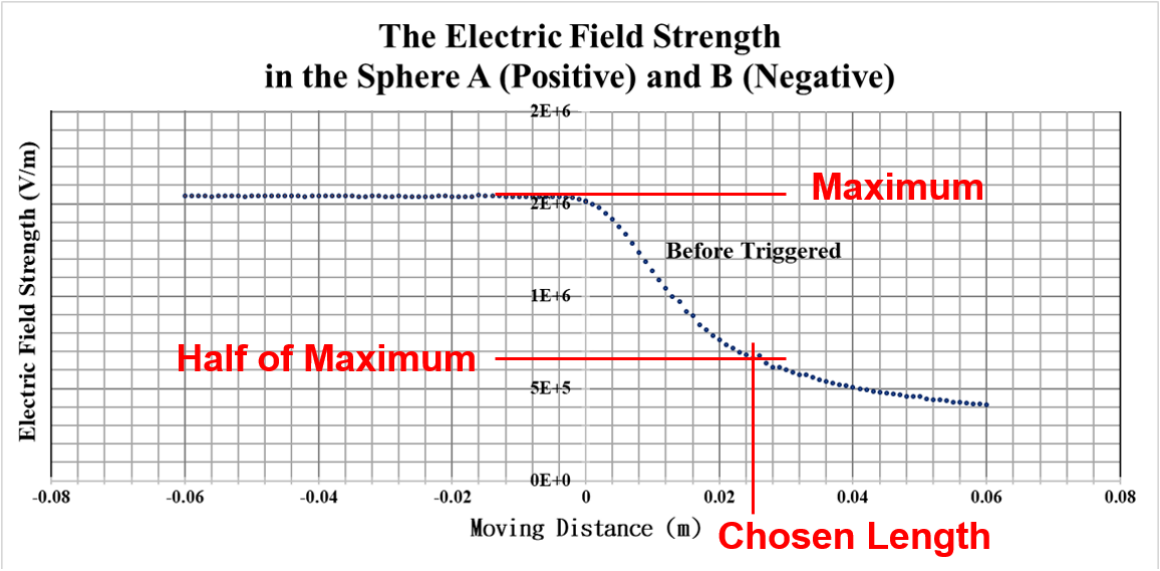

Figure 17: The chosen length of the rail-like electrodes is shorten by 50 mm.

3.2 The multi-step triggering system

The multi-step triggering system consists of a function generator, a slow trigger-pulse generator, and a Marx generator[4, 5, 13]. The function generator generates a 5 V square pulse with a width of 1.25 ms. The pulse is sent to the slow trigger-pulse generator. The slow trigger-pulse generator generates a -17-kV pulse with a rise time of 55 ± 0.4 μs. The slow high-voltage pulse is then sent to the Marx generator. The Marx generator is triggered and sends a -40-kV triggering pulse with a falling speed of -6.6 ± 0.4 kA/ns.

Figure 18 shows the circuit of the Marx generator. The capacitance of each capacitors is 40 nF and the resistance of each resistor is 10 MΩ. There are three spark-gap switches SW. 1, SW. 2, and SW. 3 and one peaking switch SW. 4. Switch 1 is a trigatron while the other switches are self-breakdown switches. Figure 19 shows the computer-aided drawing (CAD) drawing of the Marx generator without the load. There are three capacitors underneath the spark-gap switches box. The resistors are installed at the side of the box. Switch 1 is a trigatron while the other switches are self-breakdown switches. The charging voltage is 20 kV between the point A and H provided by the high-voltage power supply. When all capacitors are fully charged, voltages at points A, B, D, and F are 20 kV and points H, C, E, and G are grounded. When the triggered signal coming from the slow trigger-pulse generator activates SW. 1, point B is grounded. In the loop B, H, and C, the discharging time of the Cap. 1 and resistor R2 is far longer than the discharging time of the output. Therefore, the voltage difference across Cap.

doi:10.6844/NCKU202000512

1 is still 20 kV in the μs time scale and point C becomes -20 kV. When the SW. 2 performs a self break-down (appendix A.1), the point D connects to point C through the SW. 2 and becomes -20 kV. Again, due to the voltage difference across the Cap. 2 is unchanged, the point E becomes -40 kV. Similarly, Point F becomes -40 kV and point G becomes -60 kV. Finally, the peaking switch is connected and output -60 kV to a load.

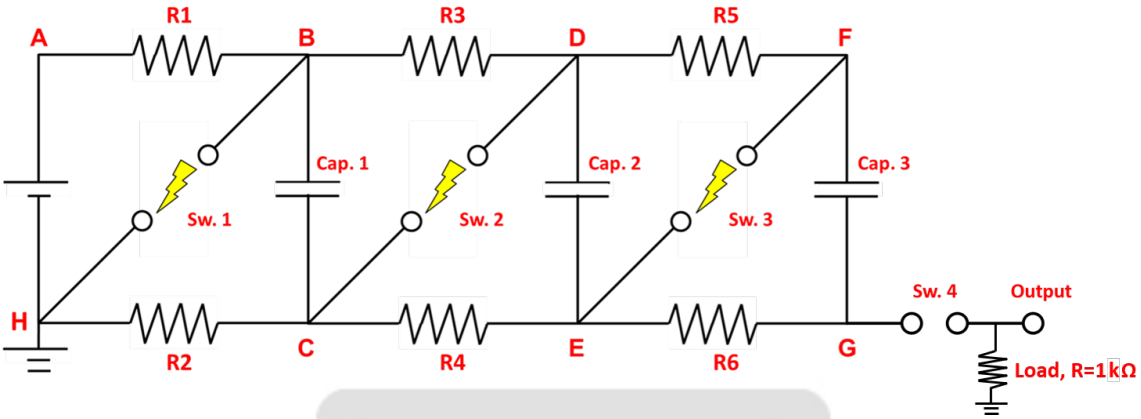

Figure 18: The circuit diagram of the Marx generator.

During the period of building the Marx generator, a circuit simulation was performed for figuring out the parameters of Marx generator. This simulation uses OrCAD Capture CIS

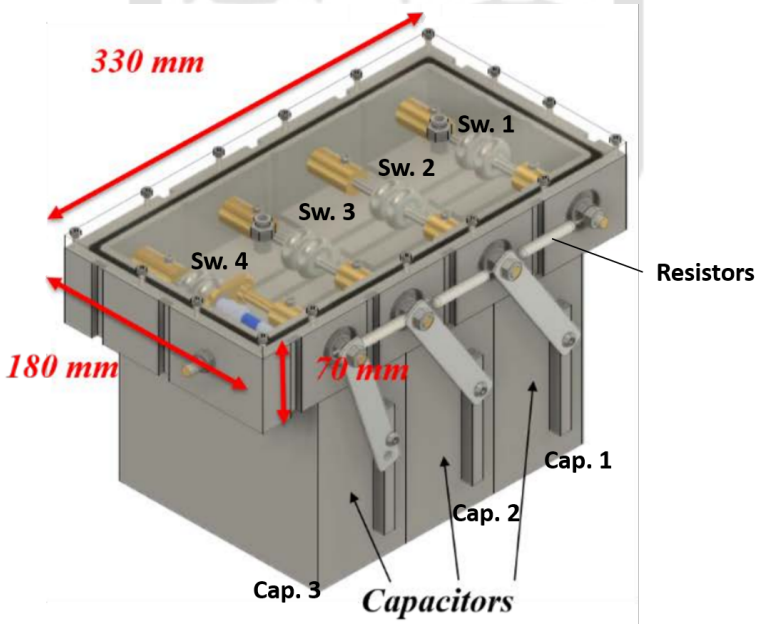

Figure 19: The drawing of Marx generator that we use.

which is a software for drawing circuit diagram and simulating the result of a circuit[14]. The main difficulty is that the software doesn't provide a proper component to simulate the spark-gap switch. Therefore, we built one model ourselves. In figure 20, the spark-gap switch is

doi:10.6844/NCKU202000512

a combination of an arbitrary function generator U2 and a voltage-control switch S2S. The spark-gap switch has three parameters which are the function V(t), V_{ON}, and V_{OFF}. The V(t) is a linear function of time $V(t) = 10^6 \times t$ which makes the voltage going to 1 V in 1 μs. The V_{ON} and V_{OFF} define three states: ON state, OFF state, and the transition state. If the control voltage is higher than the V_{ON}, the resistance of the switch is 1Ω which is much smaller than the R4. The voltage-control switch is connected. If the control voltage is lower than V_{OFF}, the resistance is 1 MΩ which is much larger than R4. The voltage-control switch is disconnected. If the control voltage is between V_{ON} and V_{OFF}, the resistance follows the function

$$R(V) = e^{\ln(10^3)+1.5\ln(10^6)\frac{V-(V_{ON}+V_{OFF})/2}{V_{ON}-V_{OFF}}-2\ln(10^6)\frac{V-((V_{ON}+V_{OFF})/2)^3}{(V_{ON}-V_{OFF})^3}}$$

where V is the control voltage[15]. The voltage-control switch is transitioning. For example, for $V_{OFF} = 0.47$ and $V_{ON} = 0.53$, the switch is initially at OFF state. When the time is at 0.47 μs, the switch will go into transition state and gradually turn on when time is at 0.53 μs. In figure 20, the component V2 provides 1 kV across the spark-gap switch. When the spark-gap switch is at OFF state, the Switch test point is not connected to the ground so that the voltage is at 1 kV. When the spark-gap switch component is at ON state, the Switch test point is connected to the ground so that the voltage is close to 0 V. In figure 21, it is a single stage Marx generator and is a similar circuit to that in figure 20. The switch test point in figure 20 is replaced by the Input test point. A 1-μF capacitor C_{10} is connected in parallel with the spark-gap switch and grounded through a resistor R_7 whose resistance is much larger than the spark-gap switch at ON state. The time constant of C_{10} and R_7 is 1 ms which is much longer than the time of the transition state of the spark-gap switch. Therefore, the voltage difference between two ends of the C_{10} is closed to a constant in the time scale of interests. Thus, the output voltage will go to -1 kV.

In figure 22, it is a three-stage Marx generator. It repeats the structure of the one-stage Marx generator three times. In the real world, all high voltage points are coupled to ground via a capacitor with a small capacitance. We use 10 pF in our model. Electric wires have small resistances. We use 1 Ω in our model. Spark-gap switches have inductance. We use 1 pH in our model. Therefore, those components are added to satisfy the real-world condition. Notice that the activating time of different spark-gap switches are different by setting different V_{OFF}

doi:10.6844/NCKU202000512

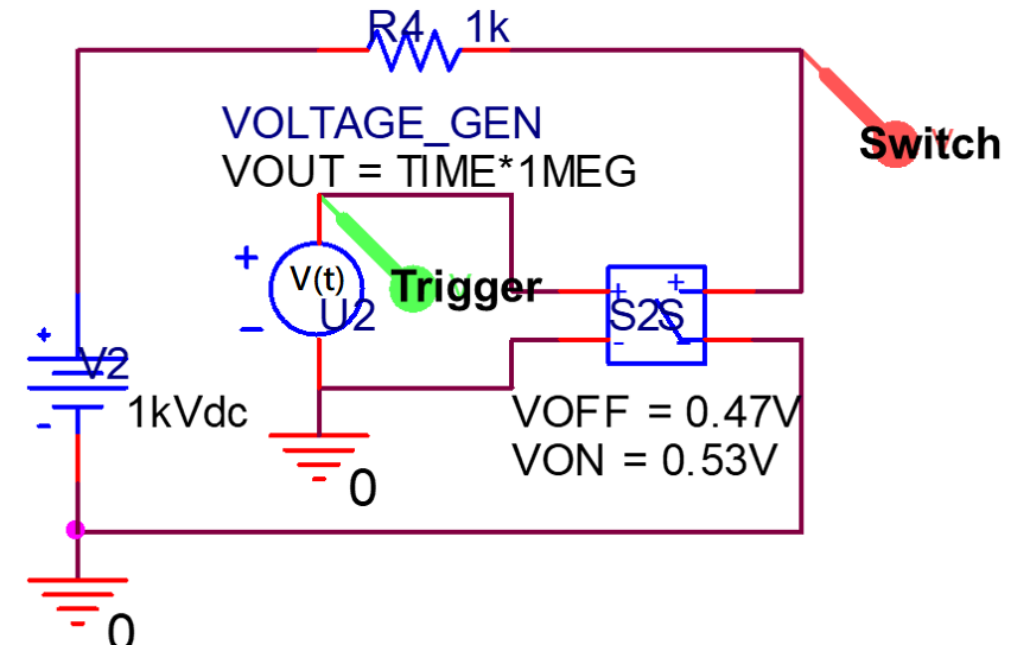

(a)

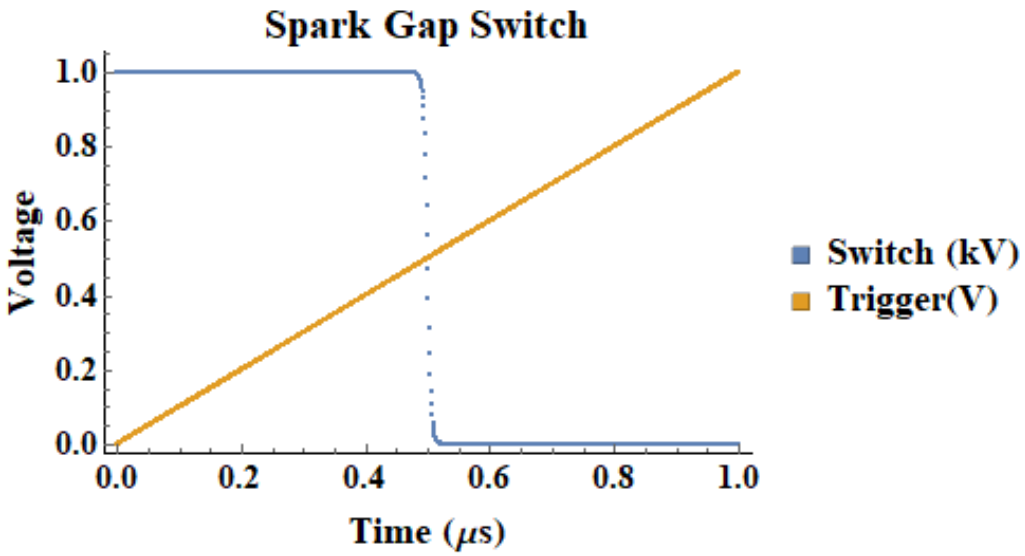

(b)

Figure 20: (a) The circuit diagram of the spark-gap switch. (b) Its simulation result.

and V_{ON}. For example, if $V_{OFF} = 0.31$, it means the time of the switch is activated at 0.31 μs. There is a time delay of 0.06 μs between each switch. As a result, the voltage at the Third test point drops like steps in figure 23. An additional spark-gap switch called the peaking switch is added at the output of the three-stage Marx generator. The peaking switch is closed after all other switches are closed. Therefore, a single step from 0 to -3 kV present at the Total test point. Outputs of First, Second, Third, and Total test point are shown in red, blue, green and black, respectively in figure 23. This simulation provides a semi-real discharge result of the three-stage Marx generator closed to the real world without actually doing the discharge

doi:10.6844/NCKU202000512

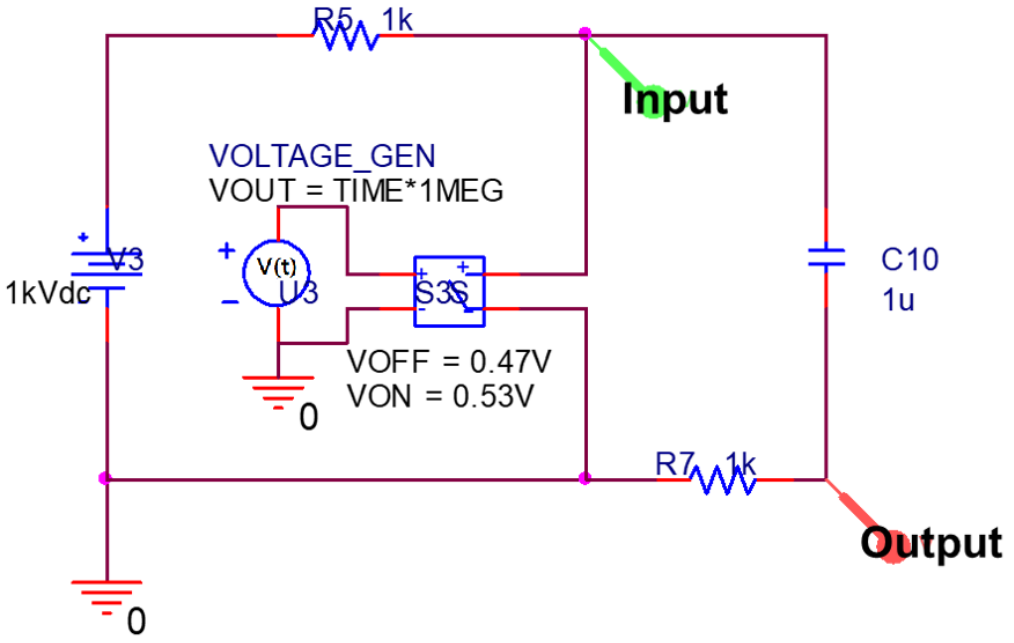

(a)

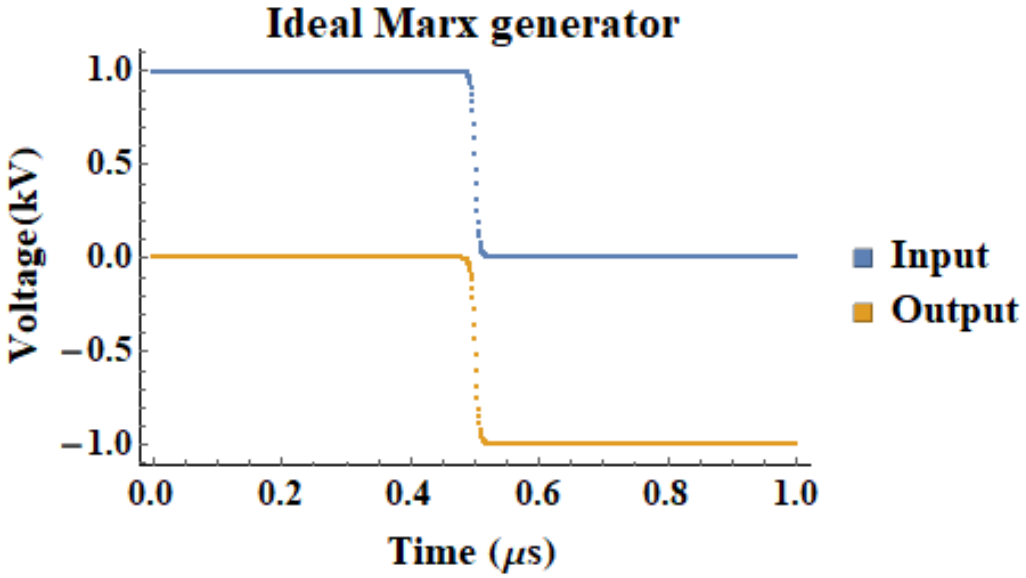

(b)

Figure 21: (a) The circuit diagram of one stage Marx generator. (b) Its simulation result.

experiment. We can use this model to redesign a Marx generator in the future if necessary. The advantage of this simulation is that it can predict some results by changing parameters of switches, resistors, capacitors, and inductors.

3.3 Discharging tests of the pulsed-power system

We conducted many discharging tests when we were building the system They were: (1) finding the breakdown voltage of the rail-gap switch in section 3.3.1; (2) the way to determine

doi:10.6844/NCKU202000512

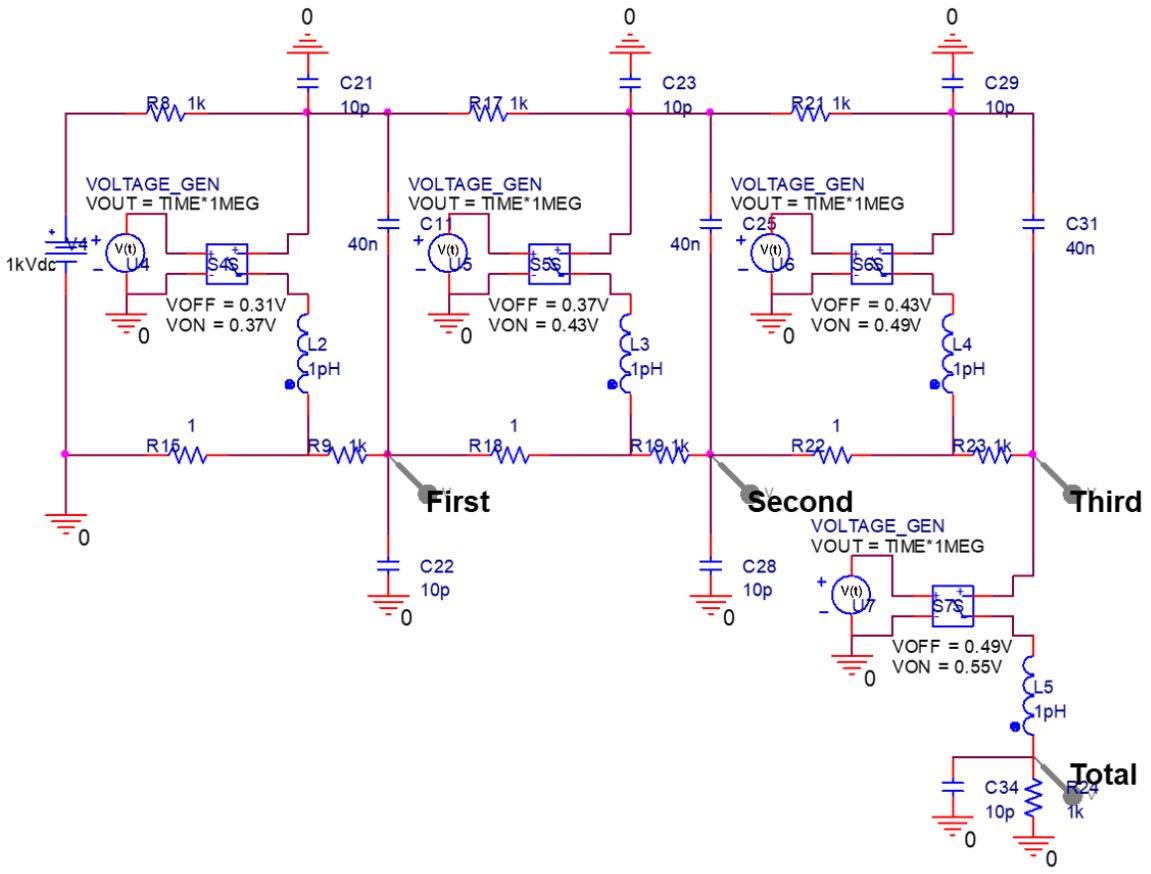

Figure 22: The circuit diagram of three stages Marx generator.

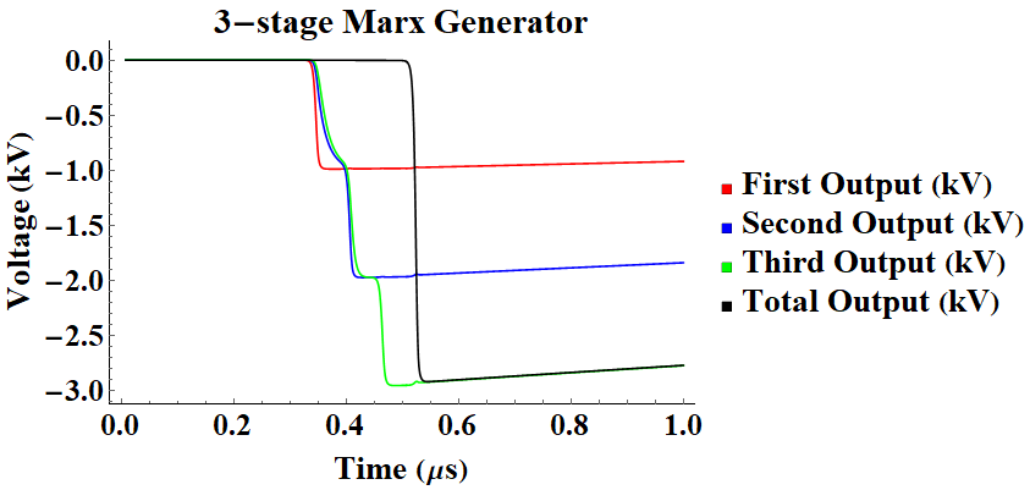

Figure 23: The three stages Marx generator simulation result.

the time reference point using the north wing discharging tests in section 3.3.2; (3) difference in performance before and after polishing the rail-like electrodes introduced in section 3.3.3; (4) the south wing discharging tests in 3.3.4; (5) the discharging tests of combing two wings using only one bick in each wing and three bricks in each wing in section 3.3.5; (6) discharging test of the whole system in section 3.3.6.

doi:10.6844/NCKU202000512

3.3.1 Rail-gap switch breakdown voltage tests

The discharge voltage of the system should below the breakdown voltage of the rail-gap switch. About the breakdown voltage of a gap between two electrodes, please read the appendix A.1. Figure 24 shows how the breakdown voltage of the rail-gap switch was tested. The testing system consisted a HV power supply, a capacitor, a rail-gap switch, and a high voltage probe. Figure 25 shows the gap distance of the rail-like electrodes and the location of the knife-edge

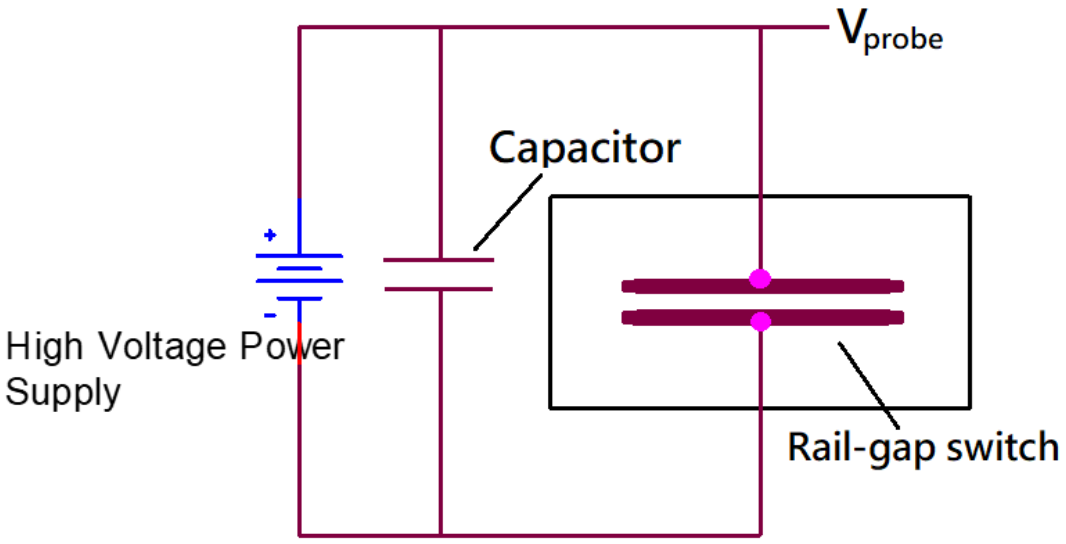

Figure 24: Circuit diagram for testing the rail-gap switch breakdown voltage.

electrode[5]. The voltage of the power supply was set to a cap voltage which meant the highest voltage that the power supply provided. The cap voltage is the setting of the power sypply and may not necessary the same as the measurement using the high voltage probe. Therefore, The voltage was gradually increased till the breakdown occured. When the voltage across rail-like electrodes was around the breakdown voltage, a self breakdown might occur and the breakdown voltage was recorded.

doi:10.6844/NCKU202000512

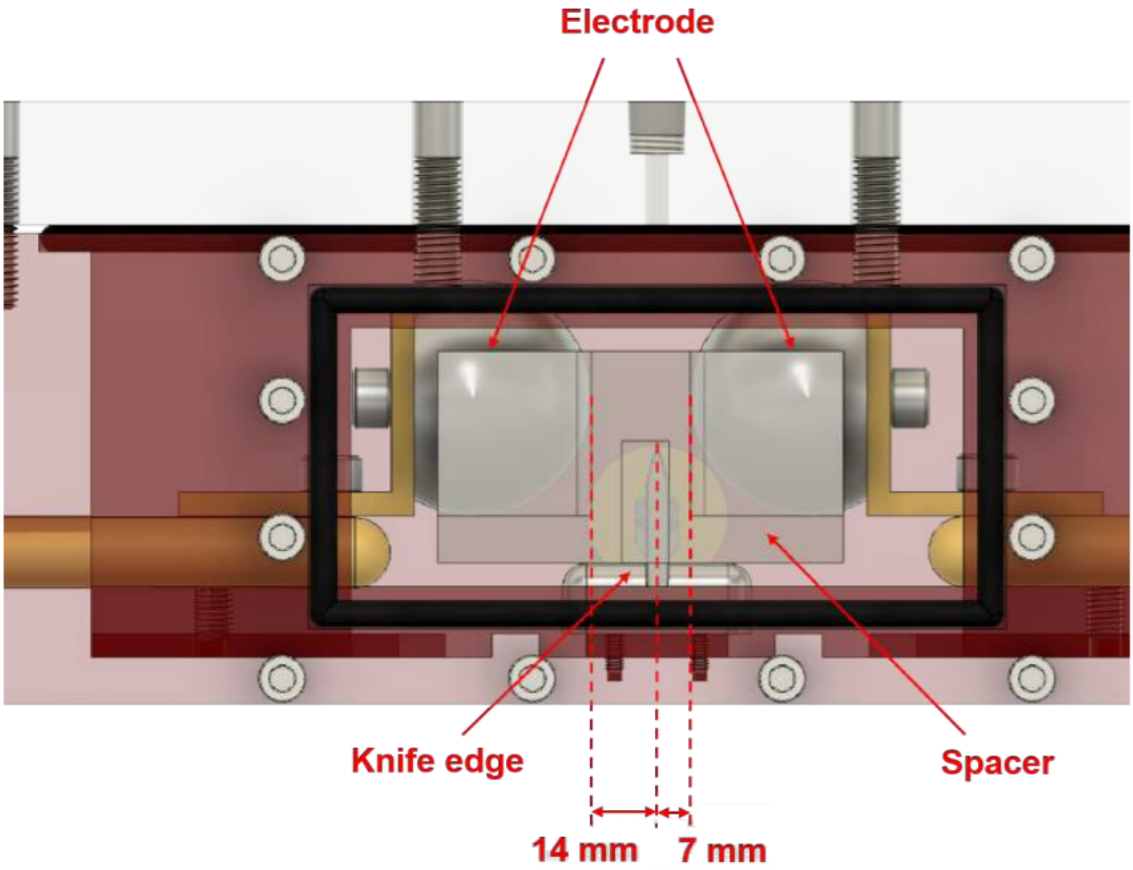

Figure 25: The total gap distance between two electrodes is 21 mm. The gap distance between knife-edge electrode and the electrode with high voltage terminal and the other gap are 7 mm and 14 mm, respectively[5].

Results of 36 breakdowns are shown in figure 26. The cap voltage is shown on the HVPS and the breakdown voltage is measured by the oscilloscope using the high voltage probe. At first, we expected the breakdown voltage below 40 kV. The results were always around 40 kV which meant the cap voltage 40 kV was at the margin of self-breakdown voltage. For cases where the breakdown voltages were higher than the cap voltage, it was probably because the cap voltage shown on the HVPS was not accurate. Thus, we changed the cap voltage to 45 kV and found that breakdown voltages were lower than the cap voltage which meant that the measured breakdown voltages were more real. After 25 discharging tests, the surface of the rail-like electrodes was getting rougher and the breakdown voltage went higher than 45 kV once. Unfortunately, the data was not recorded. Therefore, the cap voltage was set to 51 kV and three data points higher than 45 kV were recorded. As a result, the averaged breakdown voltage of all data points was 42 ± 3 kV. The pulsed-power system will be operated at 20 kV. Therefore, the gap distance of 21 mm is sufficient. This gap distance was used in this experiment. However,

doi:10.6844/NCKU202000512

we used 10.76 mm as the new gap distance in letter experiment. The new gap distance was decided by the former student Ming-Cheng Jheng in Ref.[4]. The raw data is shown in Table 12 in appendix A.2.

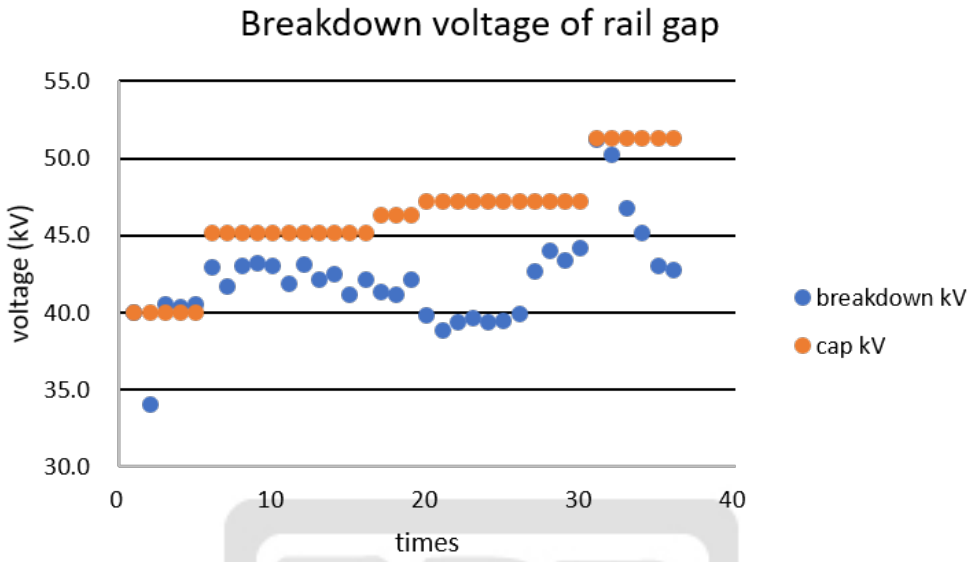

Figure 26: 36 times of the breakdown voltage result.

3.3.2 Determination of the time reference point

The time reference point is important because all dignostics we are building need to be sychronized. Figure 27 shows the circuit diagram of discharging tests of single brick in north wing. We used it to determine the time reference point. The sequences of the discharging tests are as follows:

1. 1 brick of capacitors was charged to 20 kV;
2. the triggering signal from the multi-step triggering system was sent to the rail-gap switch;
3. the triggering signal as the time reference point of all events was captured by a pickup coil;
4. the rail-gap switch was activated by the triggering signal;
5. the voltage at point B became -20 kV because the voltage at point A was connected to the ground when the switch was activated;

doi:10.6844/NCKU202000512

6. the current which discharged from the capacitor bank went through the rail-gap switch into the vacuum chamber;

7. the current was measured by the Pearson current monitor and the Rogowski coil;

8. the current returned to the capacitor bank. The CAD drawing of the experimental setup is shown in figure 28.

About the rail-gap switch, the total gap distance between two electrodes was 10.76 mm. The gap distance between knife-edge electrode and the grounded electrode was 3.9 mm. The gap distance between knife-edge electrode and the HV electrode was 6.86 mm[4]. This setup is used in all experiments later. Figure 29 shows the CAD drawing of the coaxial transmission line,

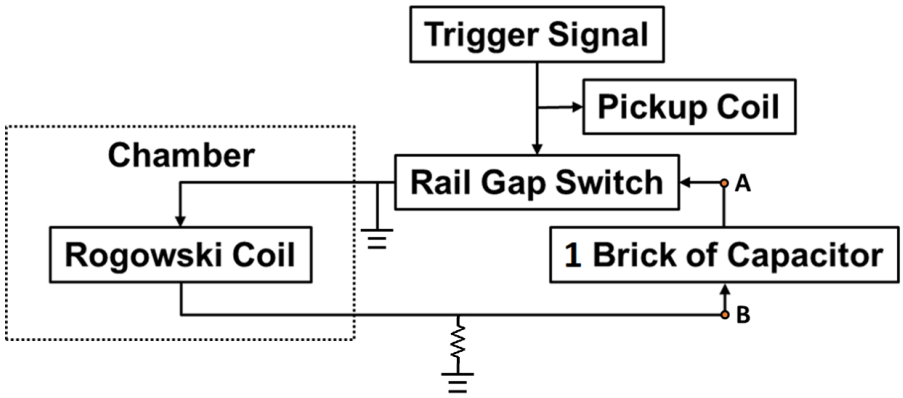

Figure 27: Circuit diagram of the north wing discharging tests.

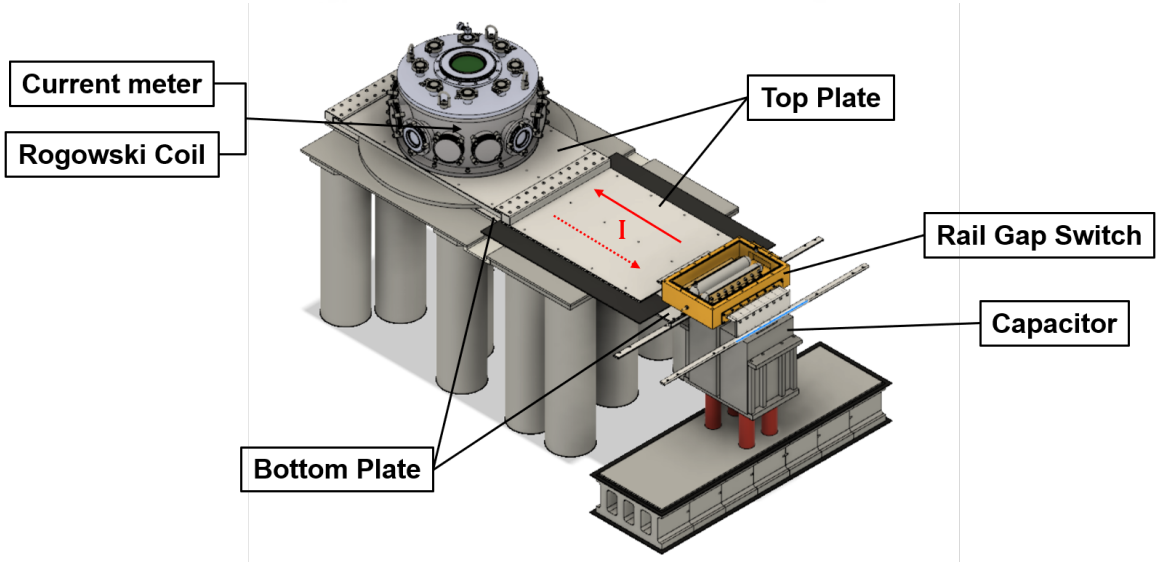

Figure 28: Setup of the north wing discharging tests.

eight wires as the load and the Rogowski coil in the vacuum chamber. The outer cylinder of

doi:10.6844/NCKU202000512

the coaxial transmission line was connected to the top plate of the parallel-plate transmission line and was grounded. The inner cylinder of the coaxial transmission line was connected to the bottom plate of the parallel-plate transmission line. The potential of the inner coaxial transmission line was negative during the discharge. Eight wires were used to connect the inner and the outer cylinders of the coaxial transmission line. Therefore, the current flowed through the top plate of the parallel-plate transmission line, the outer cylinder of the coaxial transmission line, eight wires, the inner cylinder of the coaxial transimission line, then to the bottom plate of the parallel-plate transmission line. Finally, the current went back to the capacitor bank through the bottom plate of the transmission line. The current was measured by the Rogowski coil located around the eight wires. The Rogowski coil will be introduced in section 4.1. Shown in figure 30, the pickup coil was located next to the cable between the

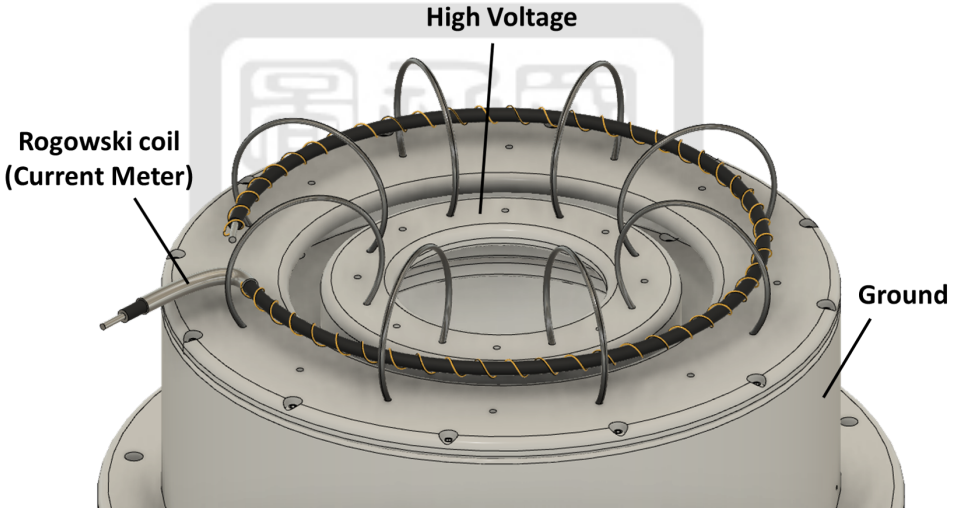

Figure 29: The total current from both wings is measured by a Rogowski coil inside the vacuum chamber.

output of the Marx generator and the knife-edge electrode of the rail-gap switch. It detected the pulse current by sensing the change of the magnetic flux generated from the pulsed current of the triggering signal. The diameter of the coil was ∼15 mm and the distance between the wire and the coil was ∼10 mm. We would like to use the output signal of the Marx generator as the reference point. Figure 31(a) shows one of the output signals of the Marx generator. It's the triggering signal. The red line is the interpolation of the blue dots, which are the raw data. Figure 31(b) shows the derivative of the output of the Marx generator. There is a minimum point in the differential. The time of that minimum point t_1 is the inflection point of the falling curve. Therefore, we define the onset of the triggering signal to be the inflection point of the

doi:10.6844/NCKU202000512

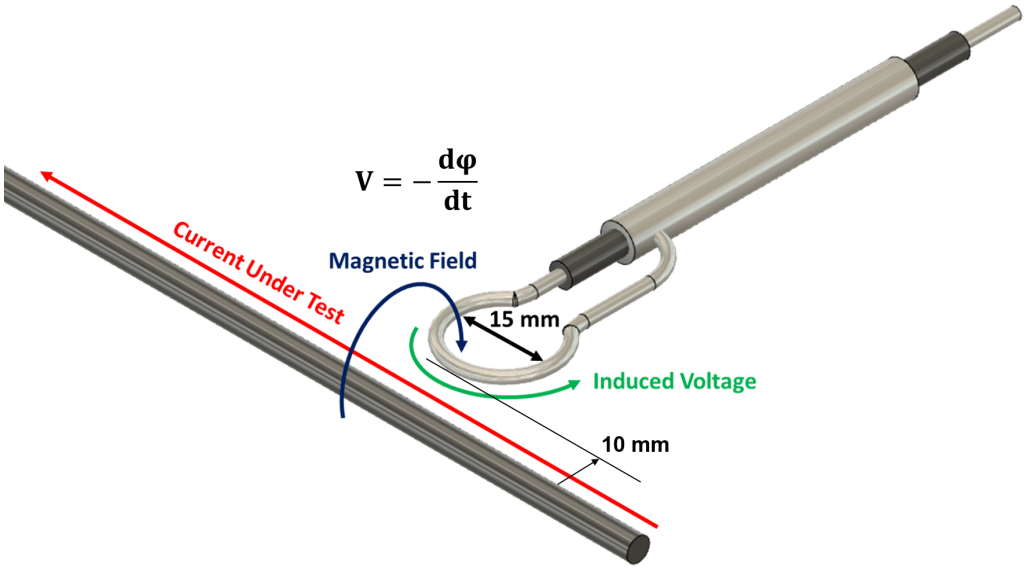

Figure 30: The pulsed current from the Marx generator is detected by the pickup coil.

output of the Marx generator. We would like to find the time reference point by comparing the triggering signal from the Marx generator with the pickup coil signal. They are shown in figure 32(a). The pickup-coil signal is also interpolated. After taking the derivative of the interpolation, the inflection point of the triggering signal is at t_1. The inflection point of the pickup-coil signal is at t_2 as shown in figure 32(b). In figure 33, The time difference between the triggering signal and the pickup-coil signal (i.e, t_2 - t_1) is 13.4 $\pm$ 0.1 ns. The data is shown in Table 13 and in appendix A.2. Shot number 7 was a missfire and it is not included in the calculation of the average and the standard deviation. Because the time difference t_2 - t_1 is relatively small compared to the period of the discharging voltage, the inflection point of the pickup-coil signal will be defined as the time reference point, i.e, t = 0. All dignostics will be sychronized to the pickup-coil signal in the future.

doi:10.6844/NCKU202000512

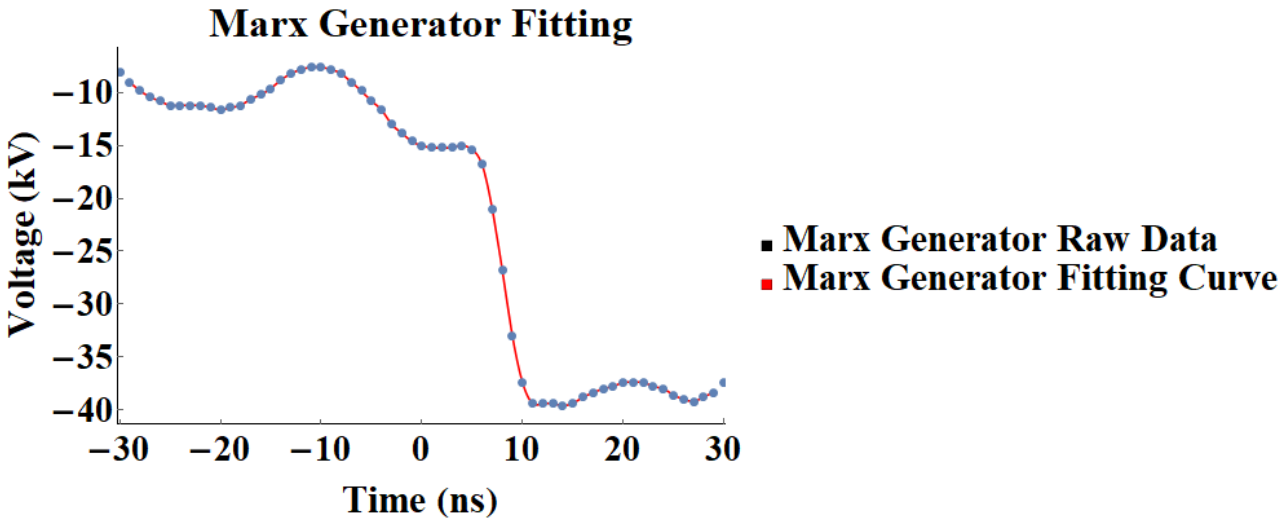

(a)

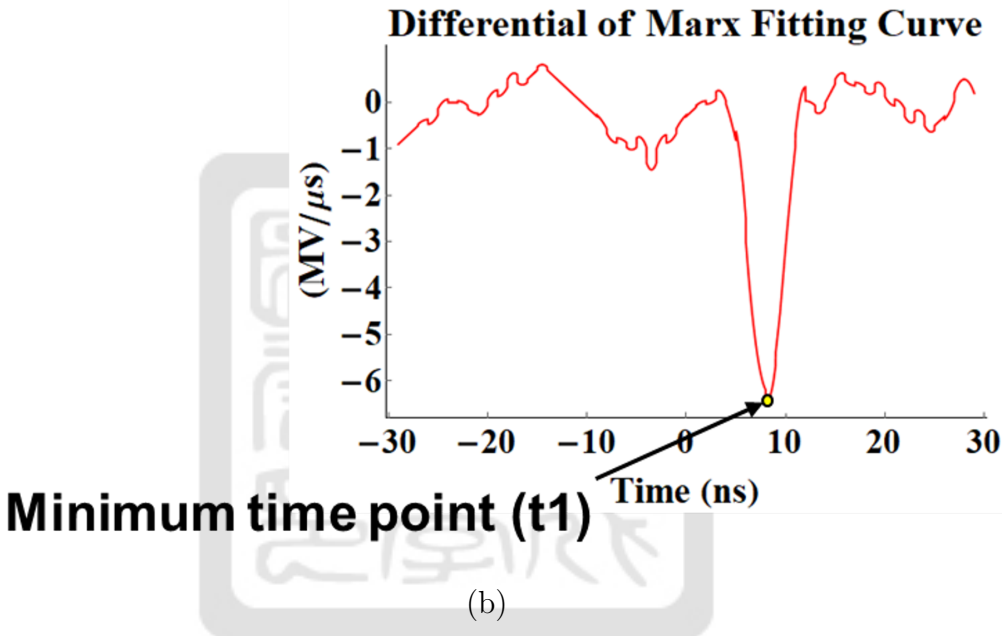

(b)

Figure 31: The data analysis of the Marx generator signal.

3.3.3 Effects of polishing electrodes of the rail-gap switch

In this section, we would like to test if the surface roughness of the electrodes in the rail-gap swich makes any differences. Thirty shots were first conducted using the same setup in section 3.3.2. The surface of the rail-like electrodes became really rough and had many burn marks. Therefore, we polished the electrodes with the sandpaper and engraving machine. The procedure is the following:

1. Remove the black and big burn marks using the alumina carving stick with the engraving machine.

doi:10.6844/NCKU202000512

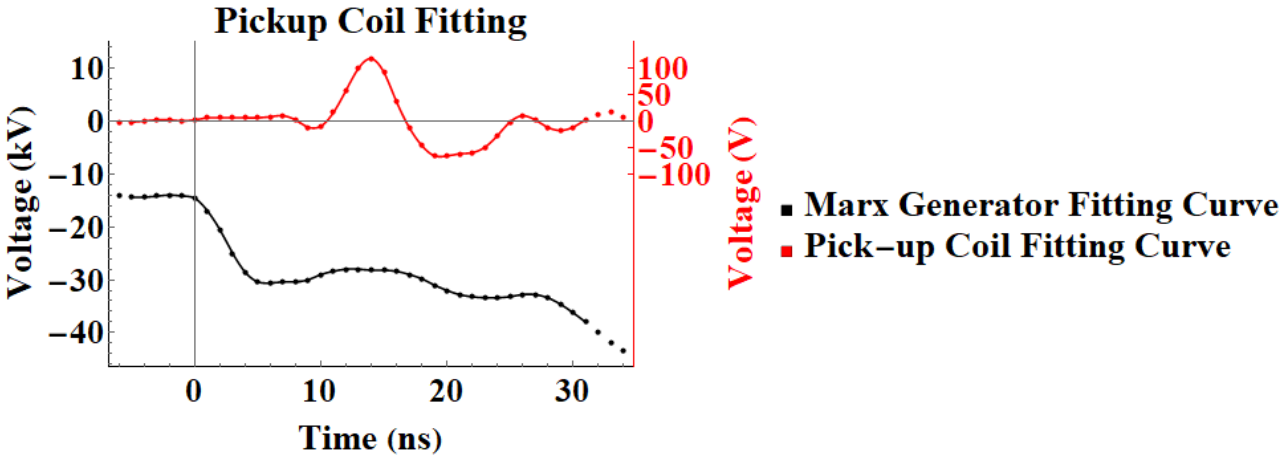

(a)

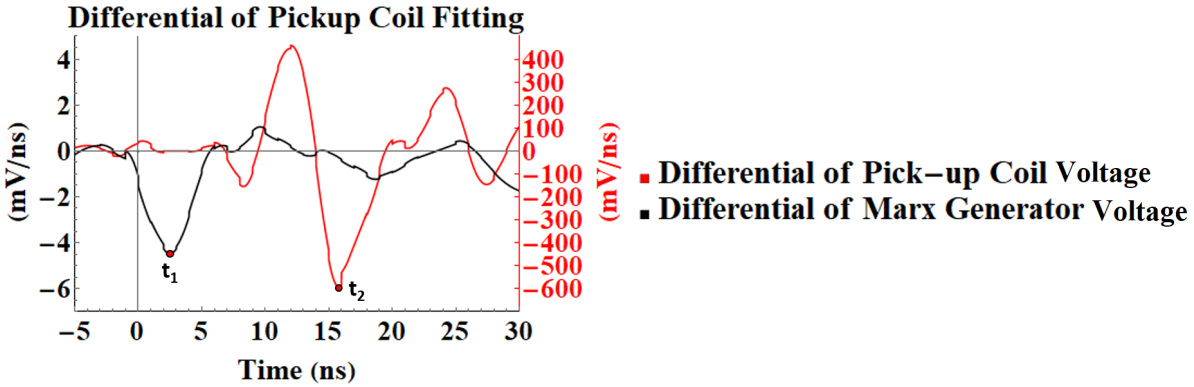

(b)

Figure 32: The data analysis of the pickup coil signal which defines the time reference point.

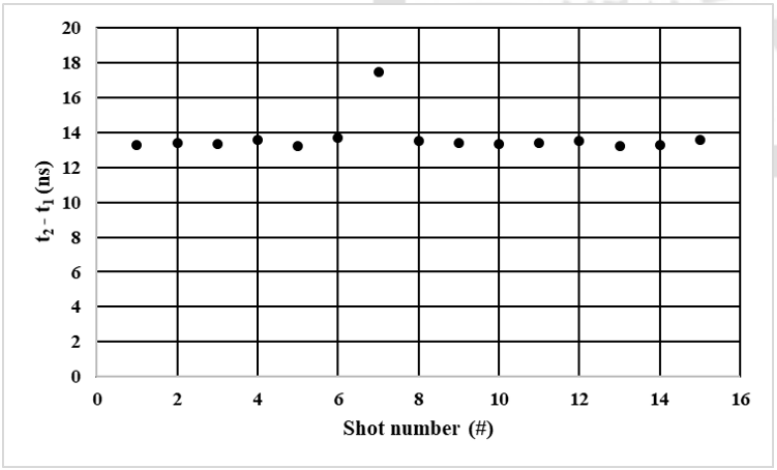

t_2 - t_1=13.4 ± 0.1 ns

Figure 33: Time difference between triggering signal and pickup coil signal, i.e, t1 - t2.

2. Remove the small scratch using the #200, #500, #1000, then #2000 sandpapers. As a result, the electrodes became smooth again. The comparison of electrodes before and after being polished is given in figure 34.

Figure 35 shows the peak current's location of the discharge. The discharging currents were fitted by the RLC discharging model which was defined as

doi:10.6844/NCKU202000512

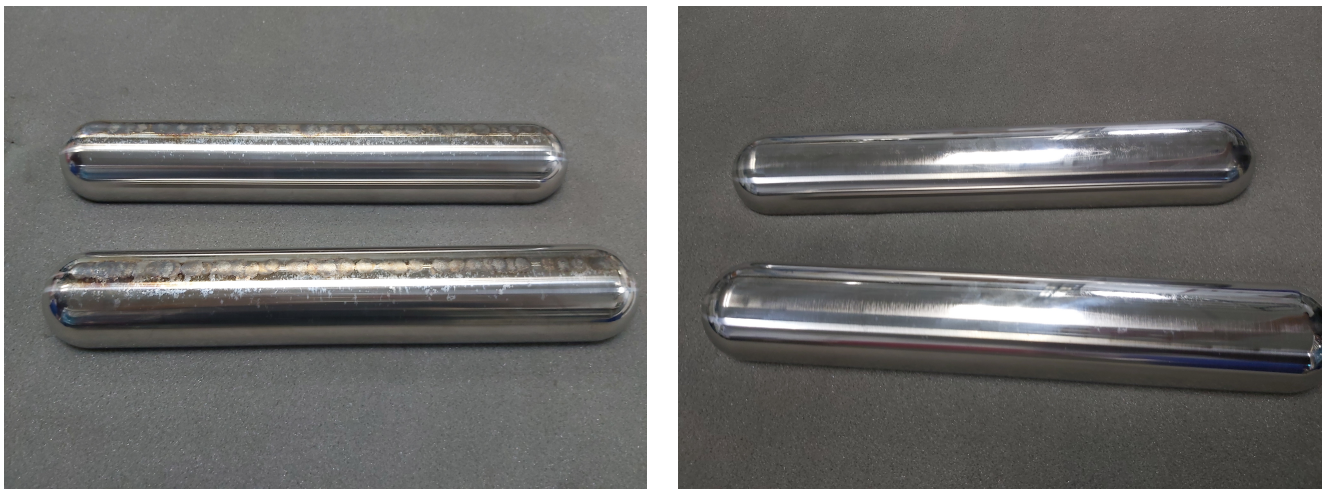

(a) Before polishing (b) After polishing

Figure 34: Before and after rail-like electrodes polishing.

$$A\, e^{\lambda t}\, \sin(\omega t + \phi) \tag{8}$$

where A is the amplitude, λ is the rate of exponential decay, ω is the angular frequency, and ϕ is the phase corresponding to the temporal offset. The fitted numbers are: $A = (2.39 \pm 0.06) \times 10^4$ V, $\lambda = -(6.14 \pm 0.60) \times 10^4$ 1/s, $\omega = (2.36 \pm 0.02) \times 10^6$ rad/s, and $\phi = (6.59 \pm 1.30) \times 10^{-1}$ rad. The minimum point is the peak current. Figure 36 shows the time of the peak currents

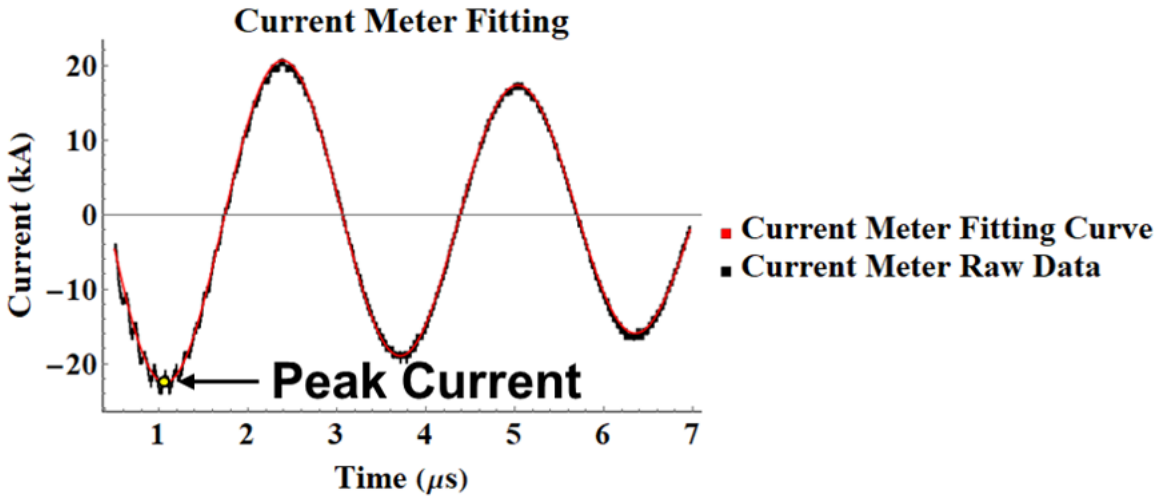

Figure 35: The peak current's location of the discharge and the fitting curve.

for one of the shot as an example. The average of the time that peak current occurs changed from 1.1 ± 0.1 μs before polishing to 0.95 ± 0.06 μs after polishing. The frequency of the oscillating current was 376 ± 3 kHz and 377 ± 2 kHz before and after the electrode being polished,respectively. The delay time of the current, which will be introduced in section 3.3.5,

doi:10.6844/NCKU202000512

was 0.71 ± 0.01 μs before polishing electrodes and 0.24 ± 0.06 μs after polishing electrodes. The data is shown in Table 14 and Table 16 in appendix A.2.

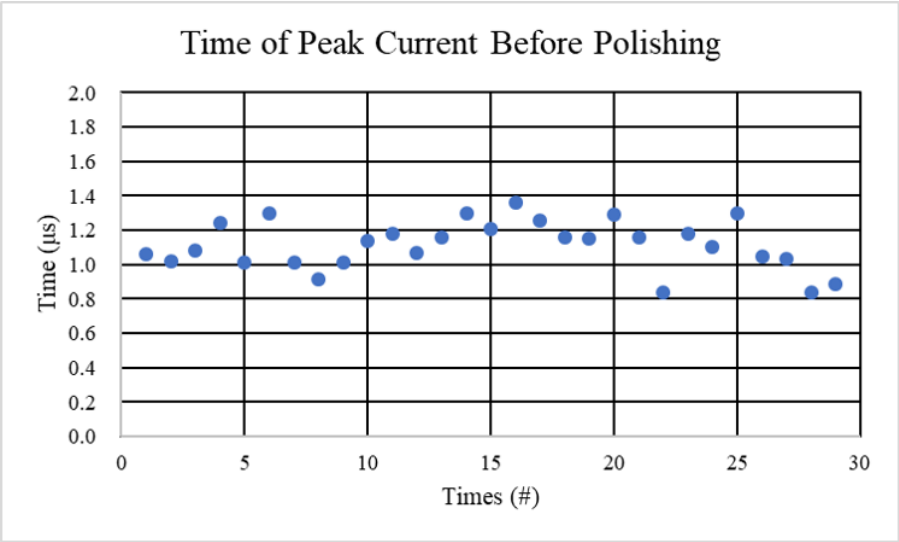

(a) Before polishing. $T_{peak} = 1.1 \pm 0.1$ μs.

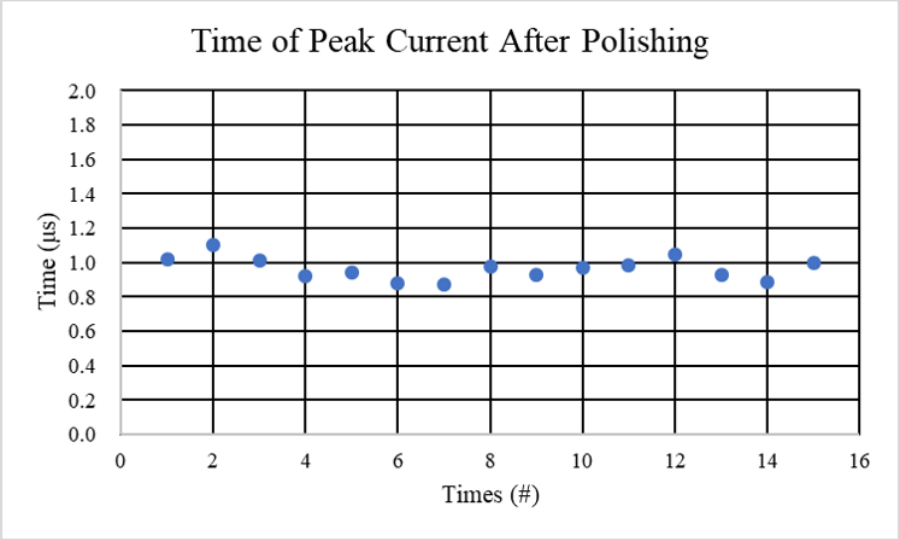

(b) After polishing. $T_{peak} = 0.95 \pm 0.06$ μs.

Figure 36: The effect of polishing rail-like electrodes on peak current time.

In summary, Table 2 shows the difference before and after polishing. The peak current of cases after polishing electrodes was 160 ns earlier than those before polishing electrodes. The standard deviation of the peak current was reduced by 57%.

3.3.4 Single wing discharging tests

The north wing was already tested and described in section 3.3.2 and 3.3.3. The south wing is the same to the north wing as shown in figure 28. All components in the north wing were duplicated in south wing. The discharging tests were also repeated for south wing using

doi:10.6844/NCKU202000512

Table 2: The difference of the peak current before and after the polishing.

	Before polishing	After polishing
Time of the peak currents	1.1 ± 0.1 μs	0.95 ± 0.06 μs
The frequency of the current	376 ± 3 kHz	378 ± 2 kHz
The delay time of the current	0.71 ± 0.01 μs	0.24 ± 0.06 μs

1-brick of capacitors. The results are given in Table 3. In this table, the total inductance data of the south wing which is 350 ± 50 nH comes from Ming-Cheng[4]. Comparing with his result, the standard deviation of the total inductance reduced significantly after polishing the rail-like electrodes. One of the current are shown in figure 37.

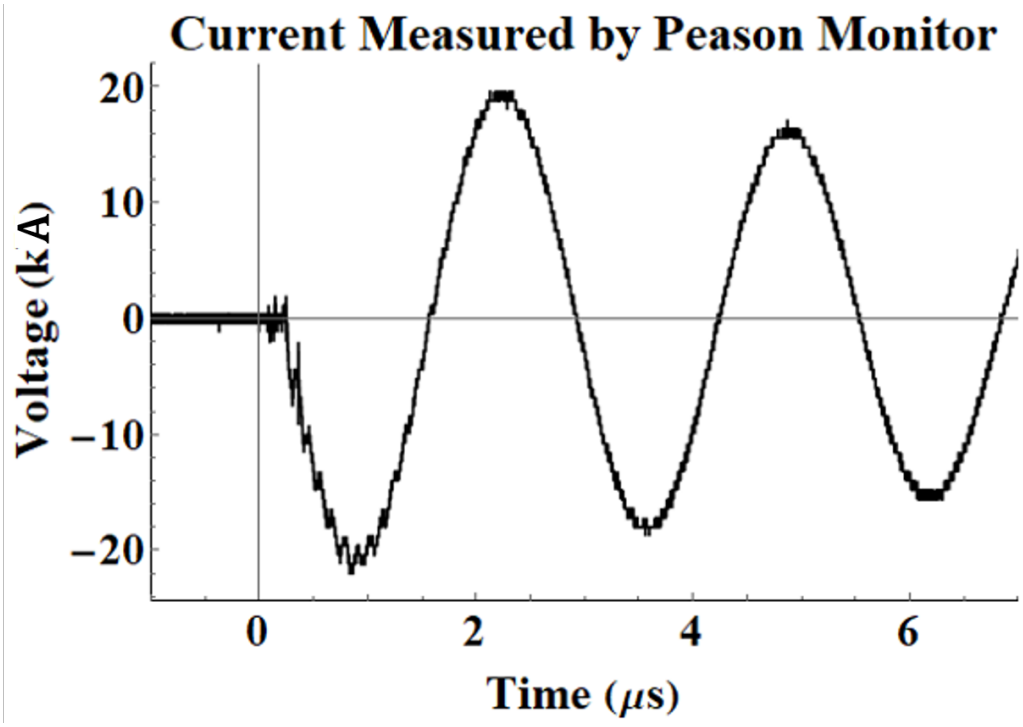

Figure 37: The current of the south wing measured by the Pearson current monitor.

Notice that the total inductance was calculated by the RLC discharging formula

$$\omega = 2\pi f = \frac{1}{\sqrt{LC}} \tag{9}$$

where the capacitance of the 1-brick of capacitors C was 0.5 μF. The total inductance using 1-brick of capacitors tested from the former student Ming-Cheng Jheng is also given in the table[4]. After polishing the electrodes, the standard deviation of the inductance had been

doi:10.6844/NCKU202000512

greatly reduced. The data is shown in table 17 in appendix A.2.

Table 3: Summary of the single wing discharging test with 1-brick of capacitors.

	North wing	South wing
Peak Current	21.8 ± 0.5 kA	20.8 ± 1.5 kA
Time of the peak current	0.97 ± 0.07 μs	0.92 ± 0.03 μs
The delay time of the current	0.24 ± 0.06 μs	0.19 ± 0.04 μs
The total inductance from Ming-Cheng	None	350 ± 50 nH
The frequency of the current	378 ± 2 kHz	378 ± 3 kHz
The total inductance after polishing	355 ± 4 nH	355 ± 6 nH

3.3.5 Discharging test of combining two wings

After the discharging tests of each wing, we assembled both wings and conducted the discharging tests. The n-n bricks of capacitors meant that there were n bricks of capacitors in each wing. From the single wing discharging test, we expected the output currents from 1-1 bricks were ∼40 kA because the peak currents from both wings individually were ∼20 kA and they are connected in parallel now. However, the Pearson current monitor can only measure currents up to 50 kA and we expected the 3-3 and 5-5 discharging tests are higher than 50 kA. It can not be used for discharging test of capacitors more than 1-1 bricks. Therefore, the 1-1 discharging tests was conducted first to calibrate the homemade Rogowski coil which can measure the current above 50 kA. The calibration of the Rogowski coil will be introduced in section 4.1. Furthermore, the 3-3 discharging tests should be conducted before the 5-5 discharging tests due to the safety reason.

Figure 38 shows the circuit diagram of the pulsed-power system. The capacitors were charged by the HVPS at points A and B. The voltage measurement points were at points A and B. The total current through points C and D was measured by the Rogowski coil which is a current meter. The rail-gap switches are activated by the triggering signal from the multi-step triggering system. A new problem was encountered by defining the rise time of the current. Shown in figure 39 is from one of the discharging current from 1-1 discharging test. Figure 40 is from one of the discharging current from 3-3 discharging test. We defined the time point of the peak current as T_{i}. The delay time is defined as T_{i} - T_{o} where $T_{\mathrm{o}} \equiv 0$ was the time reference

doi:10.6844/NCKU202000512

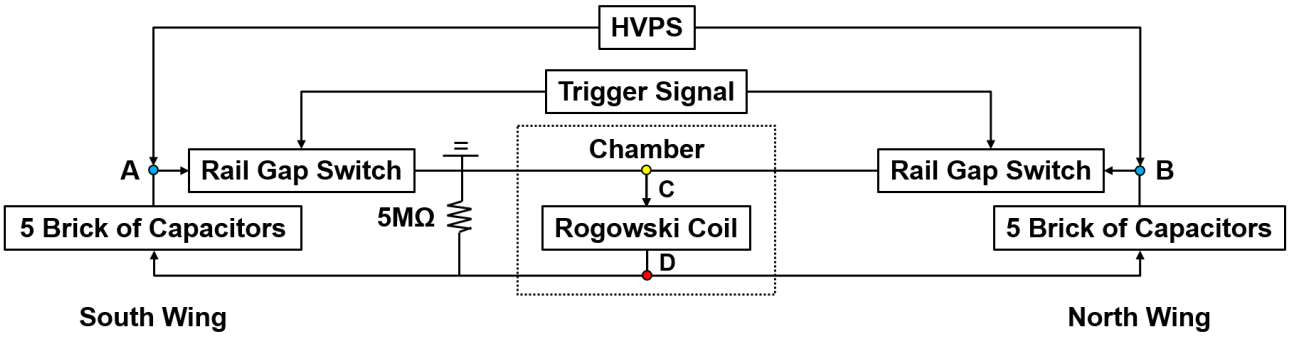

Figure 38: Circuit diagram of the pulsed-power system.

point shown in figure 39(b). However, the current didn't start at $t = 0$. Instead, the current start at $T_{\rm r}$ and the rise time was defined as $T_{\rm i}$ - $T_{\rm r}$. To find $T_{\rm r}$, the current in the range of -0.4 to 0.7 μs was fitted by a fucntion:

$$I(t) = a\ \log(\sqrt{e^{b\,(x-T_{\rm r})}+1}) \tag{10}$$

where a, b, and $T_{\rm r}$ were fitting parameters. After analyzing 30 discharge data, the average of $T_{\rm r}$ was 150 $\pm$ 40 ns and the rise time ($T_{\rm i}$ - $T_{\rm r}$) was 1.5 $\pm$ 0.4 μs. We suspect that $T_{\rm r}$ is related to the time point of the discharges of each wing. Figure 41 shows the voltage of the capacitors at each wing from one of the discharging tests. The discharge curves were filtered by a low pass filter with a cutoff frequency of 4 MHz using post processing. The time of the inflection points of the voltages from the south wing and the north wing were $t_{\rm S}$ and $t_{\rm N}$, respectively. Then, we defined $t_{\rm S-N} \equiv t_{\rm S} - t_{\rm N}$. In 30 discharging tests, there were 17 positive $t_{\rm S-N}$ and 13 negative $t_{\rm S-N}$ which meant the sequence of discharges of the north wing and the south wing was random. Therefore, we defined $t_{\rm min}$ as the leading time point of the discharge from either the south or the north wing, i.e, $t_{\rm min} \equiv \min(t_{\rm S}, t_{\rm N})$. For example, figure 41 was the case where the discharge of the south wing occurred earlier than that of the north wing, i.e, $t_{\rm min} = t_{\rm S}$. Finally, in the 30 times of discharging tests, $t_{\rm min}$ was also 150 $\pm$ 40 ns which indicated $T_{\rm r} = t_{\rm min}$. Figure 42 shows the relation between $T_{\rm r}$ and $t_{\rm min}$ from all shots. The linear regression also showed that $T_{\rm r}$= $t_{\rm min}$.

We used this way to find $T_{\rm r}$ in the 5-5 discharging tests as the time reference point because: (1) the Pearson current monitor can't measure currents higher than 50 kA while the expected current output of the 5-5 discharging tests will be higher than 50 kA; (2) the Rogowski coil

doi:10.6844/NCKU202000512

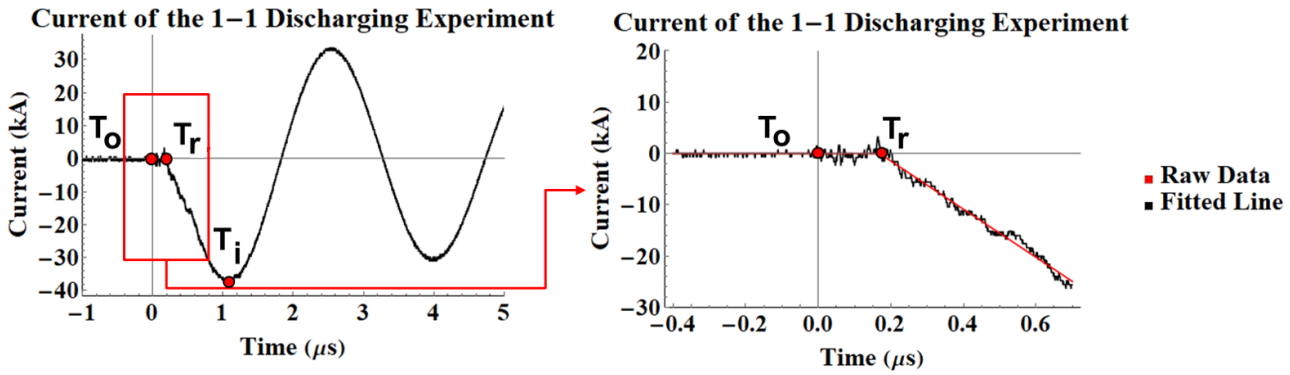

(a)

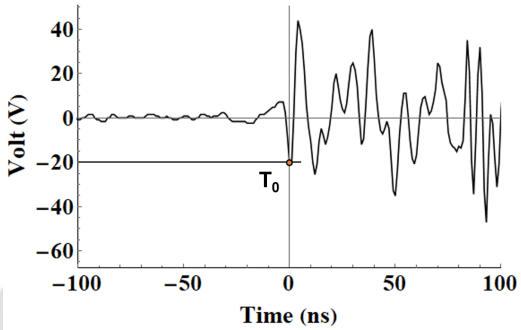

(b)

Figure 39: (a) Definition of the rise time and delay time. (b) The time reference point is defined when the pickup coil signal reach -20 V. The rise time is defined by T_{i} - T_{r}. The delay time is defined by T_{i} - T_{o}.

could measure the current higher than 50 kA but the noise of it was too high to find T_{r}; (3) the high voltage probe can measure t_{min} even if the expected current was higher than 50 kA.

In summary, The results of the 1-1 and 3-3 discharging test are shown in Table 4. In addition, the raw data is shown in Appendix 18 and 19.

Table 4: The results of the 1-1 and 3-3 discharging test.

	1-1	3-3
Peak current	41 ± 1 kA	80 ± 10 kA
Peak current time	0.94 ± 0.04 μs	1.17 ± 0.04 μs
peak current occurred t_{min}	1.6 ± 0.4 μs	1.4 ± 0.2 μs

3.3.6 Discharging tests of the whole system

We finally assembled the whole system as shown in figure 38. The setup of the 5-5 discharging tests was 5 bricks of capacitors in each wing. The discharging current which is shown in figure 43 was also fitted by Eq. 8. The inductance L can be calculated by the following

doi:10.6844/NCKU202000512

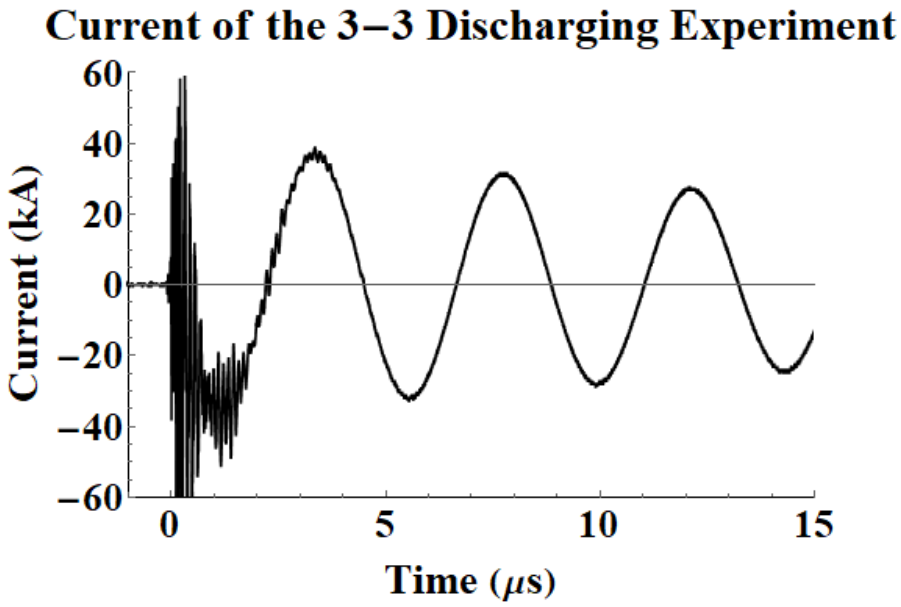

Figure 40: Current of 3-3 discharging experiment.

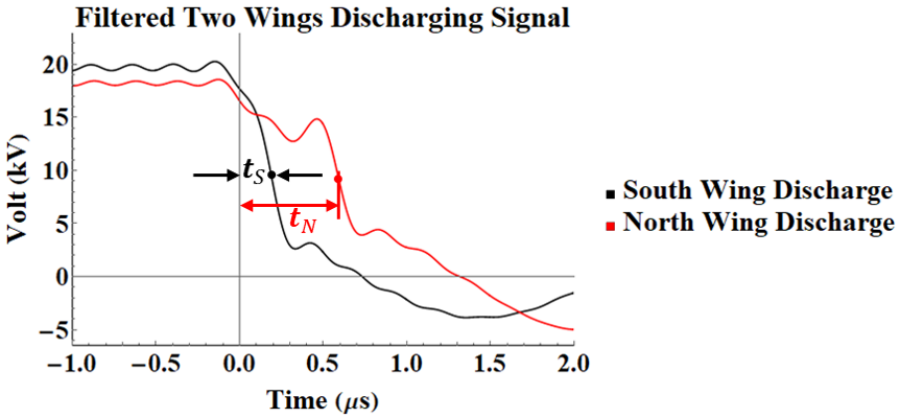

Figure 41: Capacitor banks discharge from each wing.

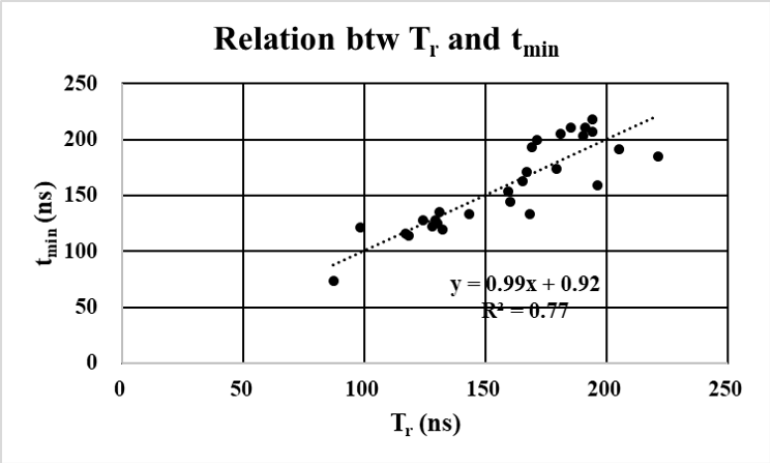

Figure 42: Relation between T_r and t_{min}.

equation using the fitted ω:

$$L = \frac{1}{\sqrt{\omega C}},\ C = 5\ \mu\text{F},\ \omega = 1.3 \pm 0.4\ \text{MHz} \rightarrow L = 150 \pm 50\ \text{nH} \tag{11}$$

doi:10.6844/NCKU202000512

where C was the total capacitance of the pulsed-power system. The inductive reactance $X_L = \omega L$ is 170 ± 30 mΩ. On the other hand, the starting time point T_r was 160 ± 50 ns. Thus, the rise time of the discharge current was 1.5 ± 0.1 μs. The data is shown in Table 21 in appendix A.2.

In summary, the results of the discharging tests of the whole system is shown in Table 5.

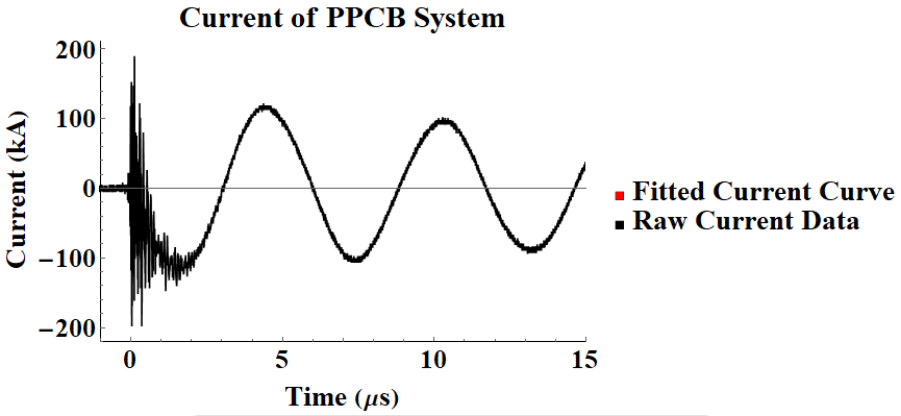

Figure 43: Current of the pulsed-power system.

Table 5: The results of the discharging tests of the whole system.

Peak current	110 ± 20 kA
Peak current time	1.63 ± 0.06 μs
Peak current occurred $t_{\min}$	160 ± 50 ns
Current Rising Time	1.5 ± 0.1 μs
Frequency of the current	1.3 ± 0.4 MHz
Inductance	150 ± 50 nH
inductive reactance X_L	170 ± 30 mΩ

doi:10.6844/NCKU202000512

4 Diagnostics

We built three diagnostics in this thesis. They are Rogowski coil for measuring the current; a time-integrated imaging system in visible light, and a time-integrated x-ray pinhole camera. The last two diagnostics are both for taking images of plasma jets. The development of the Rogowski coil with an integrator will be introduced in section 4.1. The imaging system in visible light will be introduced in section 4.2. The x-ray generated by the plasma jet needs to be filmed by a pinhole camera. The development of the x-ray pinhole camera will be introduced in section 4.3.

4.1 The Rogowski coil

The Rogowski coil with the integrator was used to measure currents above 50 kA. It's because the Pearson current monitor (Pearson 301x) which we would like to measure the 3-3 discharging test can only measure currents up to 50 kA. However, the output current of the whole system is in the order of 100 kA exceeding the capability of the Pearson current monitor.

4.1.1 Concept of the Rogowski coil

Figure 44(a) shows the drawing of the Rogowski coil. The Rogowski coil is a ring made by a coaxial cable and a curved solenoid[16]. The inner core of the coaxial cable output the signal corresponded to the current being measured while the outer layer is grounded. The curved solenoid is twined by N rounds around the coaxial cable whose outer layer is removed. One end of the curved solenoid is connected to the grounded layer and the other end is connected to the inner core. The current to be measured I_{in} going through the center of the ring perpendicularly generates a magnetic field B through the curved solenoid. From Faraday's law, the induced voltage V_{RC} is generated between two ends of the curved solenoid. The relation between I_{in} and V_{RC} is

$$M\frac{dI_{\text{in}}}{dt} = V_{\text{RC}} \tag{12}$$

where the mutual inductance of Rogowski coil $M = -\frac{\mu_0 N r^2}{2L}$, L is the radius of the Rogowski coil, r is the radius of each loop of the curved solenoid, and μ_0 is the vacuum permeability. Because the output signal V_{RC} is the differential of the input current I_{in}, the integrator is needed

doi:10.6844/NCKU202000512

for integrating the output signal V_{RC} for retrieving the input current I_{in}. Figure 44(b) shows the circuit diagram of the RC integrator. The integrating formula is

$$\frac{1}{RC}\int V_{\mathrm{RC}}dt = V_{\mathrm{out}} \tag{13}$$

where R and C are the resistance and the capacitance of the RC integrator and V_{out} is the output of the RC integrator. By combining Eq. 12 and Eq. 13, we get

$$I_{\mathrm{in}} = \frac{RC}{M}V_{\mathrm{out}}\ . \tag{14}$$

Therefore, the Rogowski coil with the integrator can measure the current going through the center of the Rogowski coil with the ratio of $\frac{RC}{M}$.

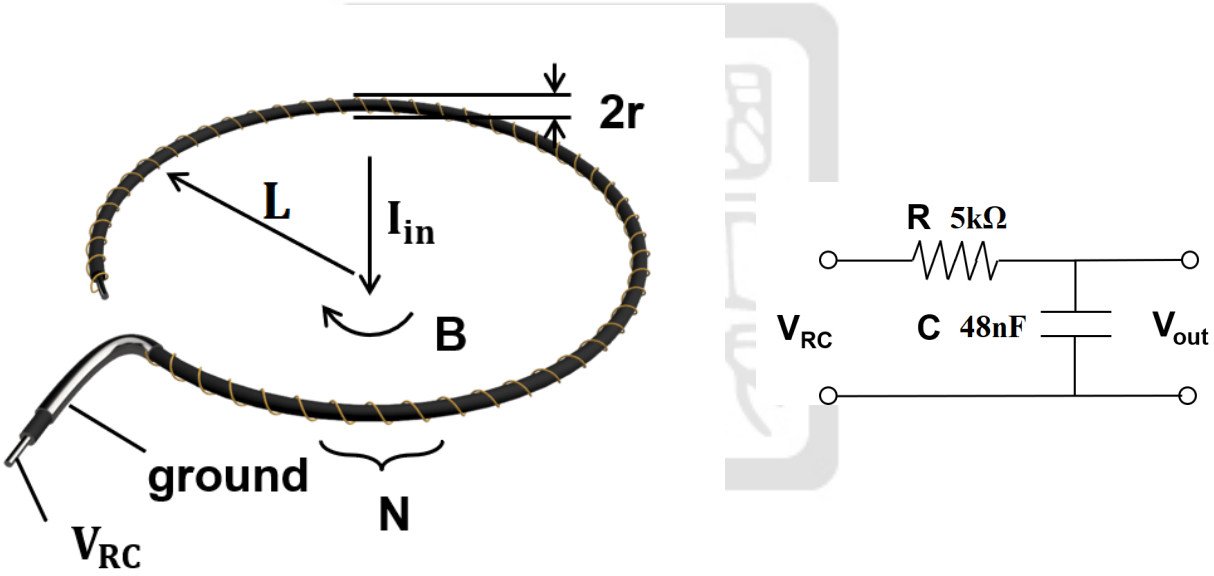

(a) (b)

Figure 44: (a) Drawing of the Rogowski coil. (b) The circuit diagram of the RC integrator.

4.1.2 Dependency of the current location

The measured current may not always go through the center of the Rogowski coil. However, Eq. 12 is only calculated assuming that the current goes through the center of the Rogowski coil. Therefore, we would like to show that the output of the Rogowski coil V_{RC} is independent of the location where the measured current goes through the Rogowski coil.

In figure 45(a), suppose the measured current I has an offset d from the center, the magnetic field will be calculated at each infinitesimal fragment along the entire circle. From Faraday's

doi:10.6844/NCKU202000512

law, we have

$$V_{\text{out}} = -\frac{d\Phi_{\text{B}}}{dt} \tag{15}$$

where Φ_{B} is the magnetic flux through the curved solenoid. The goal is to prove that Φ_{B} is independent of d. Therefore, V_{out} is also independent of d. Let the distance between each fragment and the current is l, the definitions of the angle α and θ are shown in figure 45(b). The magnetic field generated by the current is $\overrightarrow{B}$. However, the amplitude of $\overrightarrow{B}$ normal to each turn of the curved solenoid is only $B\ \cos\theta$. The effective field strength to the curved solenoid is $B\ \cos\theta$. For the special case at the center, the output voltage is

$$V_{\text{out}}(d=0) = -\frac{d\Phi_{\text{B}}(d=0)}{dt} = -\frac{d}{dt}(\frac{\mu_0 I_{\text{in}}}{2\pi L} \times \pi r^2) = -\frac{\mu_0 N r^2}{2L}\frac{dI_{\text{in}}}{dt} = M\frac{dI_{\text{in}}}{dt}. \tag{16}$$

The effective field strength to the curved solenoid is

$$B_{\text{eff}} = B\ \cos\theta = \frac{\mu_0 I_{\text{in}}\ \cos\theta}{2\pi l}\,. \tag{17}$$

The total area of all coils of the solenoid is $A = N\pi r^2$. The area per angle along the Rogowski coil is

$$\frac{N\pi r^2}{2\pi L} = \frac{\Delta A}{\Delta\alpha} \equiv (\frac{dA}{d\alpha})\,. \tag{18}$$

Finally, the integration of the magnetic flux from $\alpha = 0$ to 2π is

$$\Phi_B = \int_0^{2\pi} B_{\text{eff}}(\frac{dA}{d\alpha})d\alpha\,. \tag{19}$$

Combining Eq. 17 and Eq. 19, we get

$$\Phi_B = \int_0^{2\pi} \frac{\mu_0 I_{\text{in}}}{2\pi l} \cdot \cos\theta \cdot \pi r^2 \cdot \frac{N}{2\pi L} d\alpha \tag{20}$$

where $\frac{\mu_0 I_{\text{in}}}{2\pi l}$ is the amplitude of the magnetic field, πr^2 is the area of each loop of the curved solenoid, and $\frac{N}{2\pi L}$ is the angular density of the turns of the curved solenoid. The variables of

doi:10.6844/NCKU202000512

$\cos\theta$ and α can be calculated from the cosine laws which are

$$l^2 = d^2 + L^2 - 2dL\cos\alpha, \tag{21}$$

$$d^2 = l^2 + L^2 - 2lL\cos\theta, \tag{22}$$

i.e.,

$$\cos\theta = \frac{l^2 - d^2 + dL\cos\alpha}{lL}. \tag{23}$$

Finally, the magnetic flux Φ_B from Eq.20 becomes

$$\Phi_B(d) = \int_0^{2\pi} \frac{\mu_0 I_{\text{in}} \cdot (L^2 - dL\cos\alpha)}{2\pi L \cdot (d^2 + L^2 - 2dL\cos\alpha)} \cdot \pi r^2 \cdot \frac{N}{2\pi L} d\alpha\,. \tag{24}$$

Figure 45(b) shows the normalized magnetic flux related to the center $\frac{\Phi_B(d)}{\Phi_B(0)}$. The constant parameters which are given in section 4.1.3 are: $L = 15$ cm, $r = 2.2$ mm, $N = 50$. It shows that Φ_{B} is independent with d. Thus, V_{out} is independent of d.

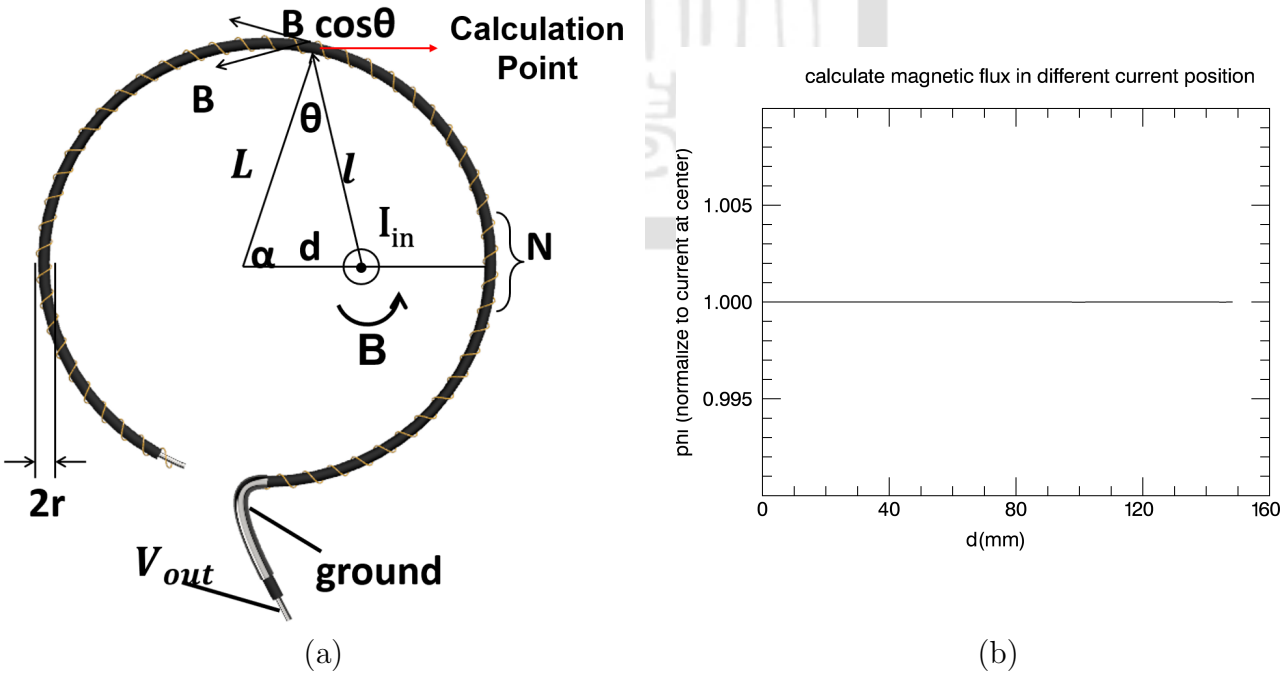

(a) (b)

Figure 45: (a) The magnetic field generated by the measured current which has an offset d from the center. (b) The normalized magnetic flux related to the center.

doi:10.6844/NCKU202000512

4.1.3 Determination of parameter

Before building the Rogowski coil and the integrator, parameters of the Rogowski coil and the integrator need to be determined using the amplitude and frequency of the input current are $I_{\max}$ and ω. They are the mutual inductance of Rogowski coil M, and the time constant τ defined as the value of the resistance times the capacitance of the RC integrator, i.e., $\tau \equiv RC$. Suppose the input current is a sinusoidal function, i.e.,

$$I_{\text{in}} = I_{\max} \sin \omega t \,, \tag{25}$$

the differential of the input current is

$$\frac{dI_{\text{in}}}{dt} = \omega I_{\max} \cos \omega t \,. \tag{26}$$

First, to control the voltage range of the V_{RC}, we need to determine the mutual inductance $M = -\frac{\mu_0 N r^2}{2L}$. Equation 12 shows the amplitude of the V_{RC}

$$|V_{\text{RC}}| = \left| M \frac{dI_{\text{in}}}{dt} \right| \approx |M \omega I_{\max}| \,. \tag{27}$$

We would like to have V_{RC} in the range of 100 V for the safety reason. The frequency ω is around 1MHz chosen from the results of the previous discharging tests[4]. The parameters related to the mutual inductance M are the radius of the Rogowski coil L, the radius of the curved solenoid r, and the number of turn N. The radius of the Rogowski coil L is limited by the surrounding structure. The radius of the curved solenoid r is limited by the radius of the coaxial cable. Therefore, they need to be chosen to satisfy $M \approx 10^{-9}$ H. Second, after the mutual inductance M is chosen, τ is the next thing to be determined. Suppose V_{RC} is around 100 V and the ω is around 1MHz, Eq. 13 shows

$$|V_{\text{out}}| = \left| \frac{1}{RC} \int V_{\text{RC}} dt \right| \approx \left| \frac{1}{RC} \frac{1}{\omega} V_{\text{RC}} \right| = \left| \frac{V_{\text{RC}}}{\omega RC} \right| \,.$$

The approximation is only valid when $\omega RC \gg 1$. We get the $|V_{\text{out}}| \approx \left|\frac{V_{\text{RC}}}{\omega RC}\right|$ is between 0.1 to 1 V, which is measurable. Therefore, The time constant is around 10^{-3} to 10^{-4} sec. As a result, the parameters of our homemade Rogowski coil with the integrator are $L = 15$ cm, $r =$

doi:10.6844/NCKU202000512

2.2 mm, $N = 50$, $R = 5$ kΩ, $C = 48$ nF, and $\tau = RC = 0.24$ ms.

4.1.4 Building procedures

To build the Rogowski coil, the needed materials are a coaxial cable that has a female BNC connector connected and a thin wire such as an enameled wire or a single core wire. The length of the coaxial cable needs to be longer than $2\pi L$ plus the length that carries the signal out. In figure 46(a), the steps are

1. Remove the BNC connector at one end of the coaxial cable if BNC connectors are connected to both end of the cable.
2. Remove the external insulator with a length of $2\pi L$.
3. Remove the outer grounded layer with a length of $2\pi L$.
4. Remove a little section of the middle insulator at the tail of the coaxial cable.
5. Solder the thin wire to the inner core of the coaxial cable at the end of the cable. Make the N-turn solenoid around the coaxial cable using the thin wire.
6. Make sure N turns of loop uniformly distributed and twisted tightly along the coaxial cable in the region where the outer insulator and the outer grounded layer are tear-off.

The homemade Rogowski coil was shown in figure 46(b). The yellow shield which covers the Rogowski coil was used to reduce the noise of the Rogowski coil. The shield is made by the twined aluminum foil like the curved solenoid. However, each turn overlaps on top of the precious turn with the polyimide tape in between. The structure of the shield is shown in figure 47. We sticked the aluminum foil on the polyimide tape to separate the overlapping place. Therefore, we twine the aluminum foil with the polyimide tape on a water tube and the overlapping place of the aluminum foil does not contact with each other. We expect that the noise from the azimuthal electric field will be shielded by the aluminum foil while the magnetic field generated by the measured current can penetrate thrould the shield. The shielding should be grounded. However, the results with and without grounding the shielding were almost no difference.

doi:10.6844/NCKU202000512

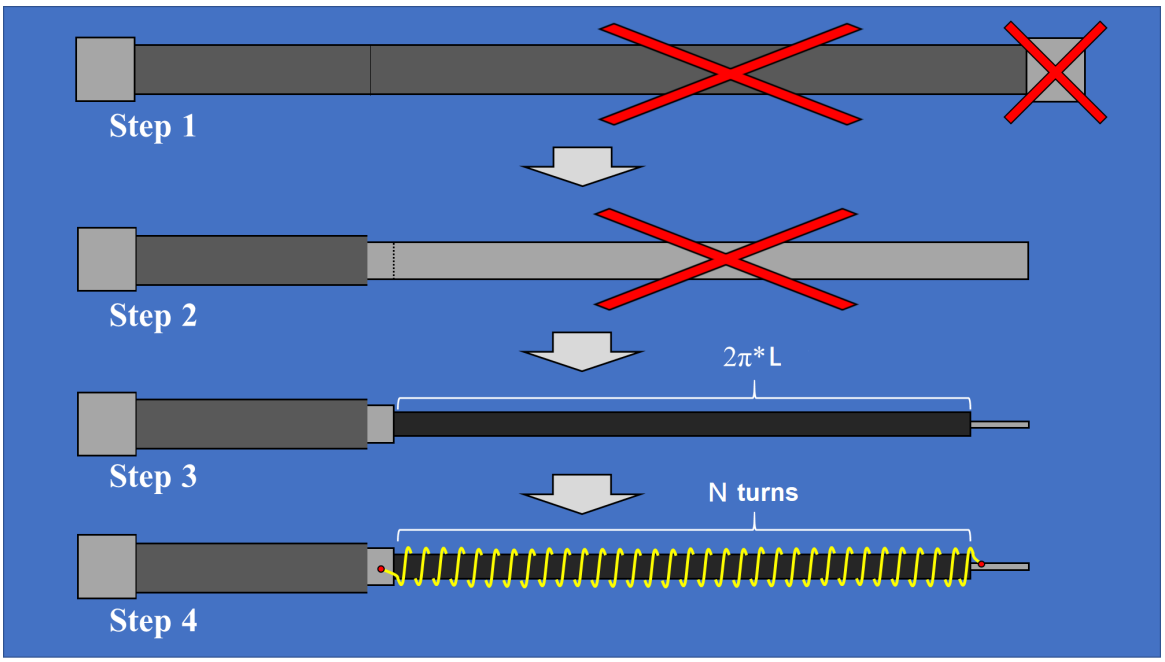

(a)

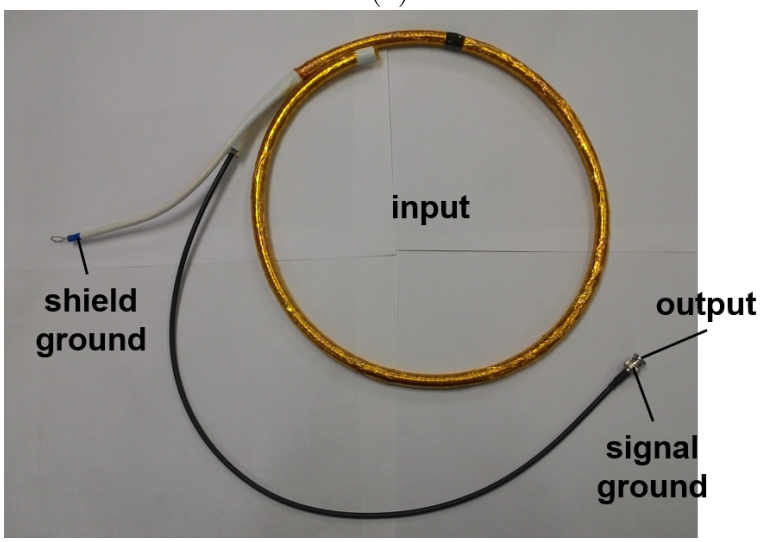

(b)

Figure 46: (a) Production of the Rogowski coil. (b) The homemade Rogowski coil.

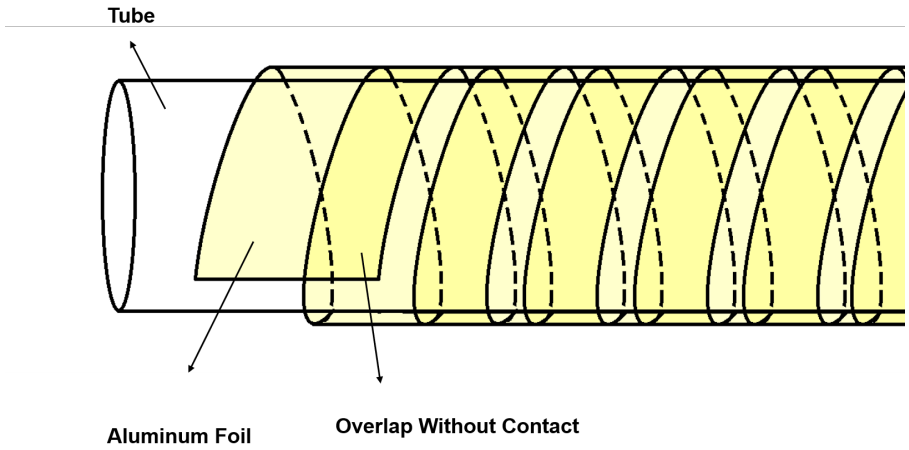

Figure 47: The structure of the yellow shield.

doi:10.6844/NCKU202000512

4.1.5 Calibration using a function generator

The Rogowski coil itself was first calibrated by using a function generator. The calibration was conducted by comparing the current of the function generator and the output voltage of the Rogowski coil. In figure 48(a), the function generator is connected to a 10-turn coil through a resistor. The resistor is for measuring the input current via measuring the voltage across the resistor. The purpose of the 10-turn coil is to increase the current from the function generator by 10 times.

The result is plotted in figure 48(b). The black curve is the voltage from the function generator that generates the measured current

$$V_{\text{in}} = I_{\text{in}}R + L\frac{dI}{dt} \approx I_{\text{in}}R \tag{28}$$

where $L\frac{dI}{dt}$ is the inducted voltage across the 10-turn coil which is much smaller than $I_{\text{in}} \cdot R$. To prove that the approximation is valid, we first estimate the inductance of the 10-turn coil L

$$L = \mu_0 K N^2 \frac{A}{l} \tag{29}$$

where $K \approx 1$ is the calculation of Nagaoka's coefficient which can approximate to 1, μ_0 is the permeability of free space, $N = 10$ is the number of turns, $A = \pi \times (0.15)^2$ m^2 is the area of cross-section of the coil, and $l = 0.03$ m is the length of the coil[17]. Therefore $L \approx 2.96 \times 10^{-8}$ H and the

$$L\frac{dI}{dt} = L\omega I \approx 4.79 \times 10^{-4} \ll 3 \tag{30}$$

where $\omega = 2\pi f = 2\pi \times 400$ kHz, and $I = \frac{V}{R} = \frac{3\,V}{46.6\,\Omega}$. The red curve is the output voltage V_{out} in the unit of mV. The V_{in} from the function generator was a sine wave and the V_{out} from the Rogowski coil was also a sine wave with an offset and some noises. To get the mutual inductance of the Rogowski coil M, Eq. 27 was used.

First, we calculated

$$\omega I_{\text{in}} = \omega \frac{V_{\text{in}}}{R}$$

where ω is the angular frequency of the measured current. Second, we did the Fourier transform of V_{out} of the Rogowski coil and used the mode amplitude of the with the maximum amplitude

doi:10.6844/NCKU202000512

of the V_{out} as shown in figure 48(c). The mode had a frequency of 490 kHz which coincided with the input frequency as expected. Third, we compared the measured current times the angular frequency ωI_{in} and the V_{out} as shown in figure 48(d). The y-axis is ωI_{in}, the x-axis is V_{out}, and the slope is the reciprocal of the mutual inductance M which is $(1.01 \pm 0.01) \times 10^{-9}$ H.

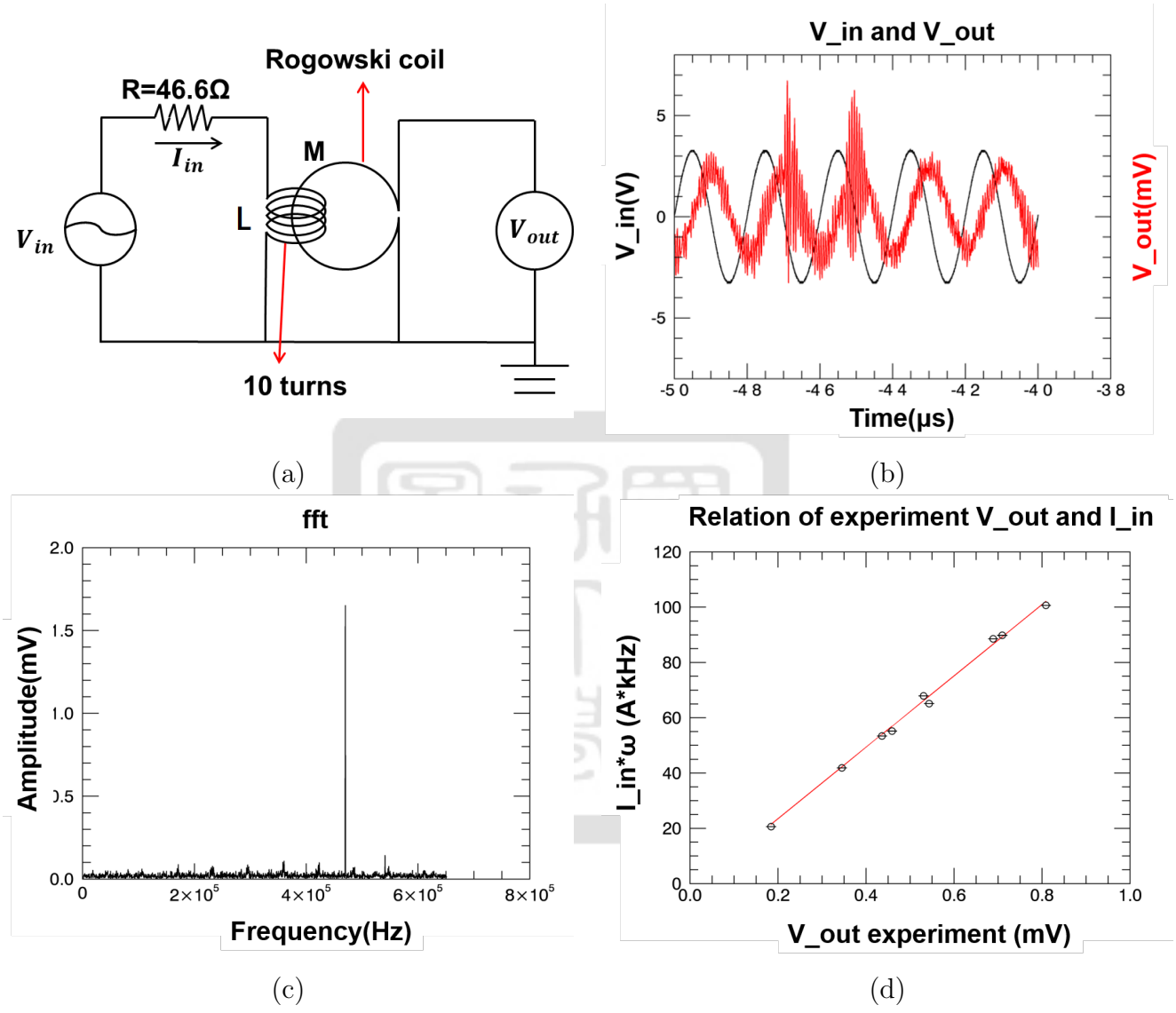

Figure 48: (a) Calibration setup of the Rogowski coil using the function generator. (b) One of the results shown by the V_{in} and V_{out}. (c) The Fourier transform of the output voltage data V_{out} from Rogowski coil. (d) Comparison between the ωI_{in} and the V_{out}.

4.1.6 RC integrator

An RC integrator is used to integrate the signal from the Rogowski coil V_{RC} to get the measured current I_{in}. Figure 44(b) shows the circuit diagram of the RC integrator. The input

doi:10.6844/NCKU202000512

voltage V_{RC} and the output voltage V_{out} have the relation

$$V_{\mathrm{RC}} = R\frac{dQ}{dt} + \frac{Q}{C}\,, \tag{31}$$

$$V_{\mathrm{out}} = \frac{Q}{C} \tag{32}$$

where Q is the charge quantity in the capacitor. Therefore, by solving Eq. 31 and Eq. 32, we get

$$Q = e^{-\frac{t}{RC}} \int_0^t \frac{1}{R}\, e^{\frac{t}{RC}}\, V_{\mathrm{RC}} dt\,. \tag{33}$$

If the time scale is much less then the value of RC, i.e. $t \ll RC$,

$$V_{\mathrm{out}} \approx \frac{1}{RC} \int_0^t V_{\mathrm{RC}}\, dt\,. \tag{34}$$

Currently, we have the value of RC equals to 240 μs in section 4.1.3 and the rising time of the discharging current equals to 1.5 $\pm$ 0.1 μs in section 3.3.6. Therefore, the homemade RC integrator which shows in figure 49 works in this timescale.

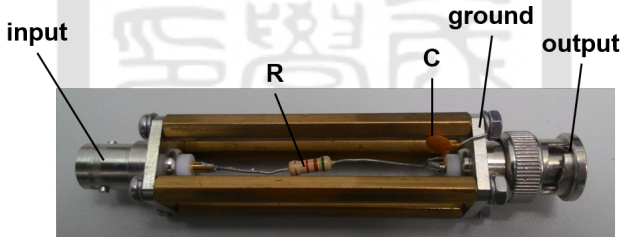

Figure 49: The homemade RC integrator.

4.1.7 Calibration of the Rogowski coil with and without the integrator using the pulsed-power system

The calibrations were conducted by measuring the same current output from the single wing of the pulsed-power system we built by using both the Pearson current monitor (modal 301x) and our Rogowski coil with and without the integrator. The Rogowski coil without the integrator was calibrated first. The calibration with the integrator was performed afterward.

Figure 50 shows the calibration circuit diagram of the Rogowski coil without the integrator. This calibration is done with the north wing discharging test using one brick of capacitors

doi:10.6844/NCKU202000512

which is shown in section 3.3.2. The high voltage power supply charged the capacitors to 20 kV. The total capacitance was 0.5 μF storing 100 J when the capacitors were charged. The HVPS supplies the discharging energy and the Marx generator which provides the triggered signal for a rail-gap switch. When the Marx generator was activated, the rail-gap switch was triggered and connected the capacitors to the ground, generating the measured current for the current monitor and the Rogowski coil. The current monitor made by Pearson gave the correct measured current $I_{\rm in}$ and the Rogowski coil to be calibrated gave the output voltage $V_{\rm RC}$. An example of the data is shown in figure 51(a), the x-axis is time, the black data is the

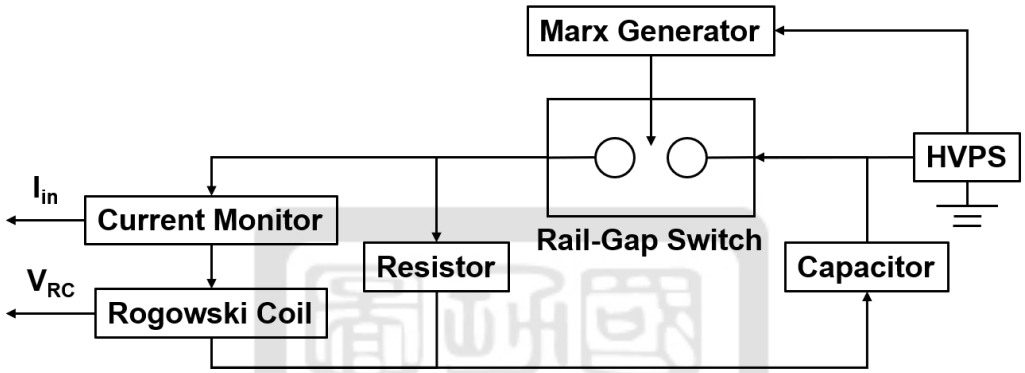

Figure 50: Calibration circuit diagram of the Rogowski coil without the integrator.

measured current $I_{\rm in}$, and the red data is the output voltage $V_{\rm RC}$. To use Eq. 12, we change the differential into the integral

$$M\frac{dI_{\rm in}}{dt} = V_{\rm RC} \rightarrow M\, I_{\rm in} = \int V_{\rm RC} dt\,. \tag{35}$$

Therefore, in figure 51(b), the output voltage $V_{\rm RC}$ in black was first fitted by the function

$$A\, e^{\lambda x}\, \sin(\omega x + \phi)\,. \tag{36}$$

The fitted parameters are: $A = 99.6 \pm 0.9\,{\rm V}$, $\lambda = (-3.8 \pm 0.2) \times 10^5\,{\rm s}^{-1}$, $\omega = (2.37 \pm 0.01) \times 10^6\,{\rm rad/s}$, $\phi = 0.3 \pm 0.4\,{\rm rad}$. The parameters are also shown in appendix 22. We then took the integration $\int V_{\rm RC} dt$ of the fitted function. From Eq. 35, we got the mutual inductance $M = (1.812 \pm 0.008) \times 10^{-9}\,{\rm H}$ and the delay time of $V_{\rm RC}$ was $(4.8 \pm 0.2) \times 10^{-8}$ s in 15 samples. The data is given in appendix 23.

Next, the calibration of the Rogowski coil with the integrator using the same circuit shown

doi:10.6844/NCKU202000512

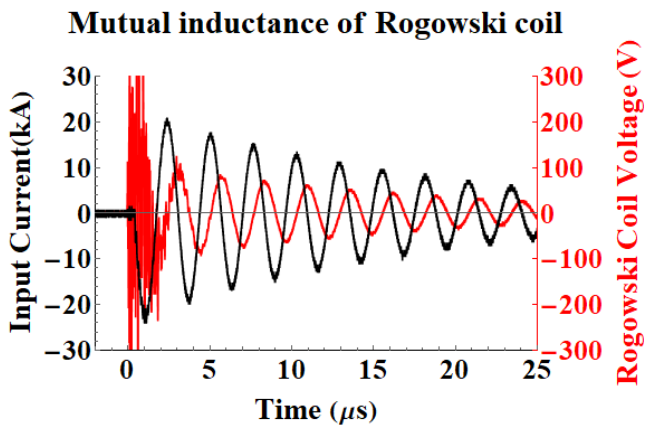

(a)

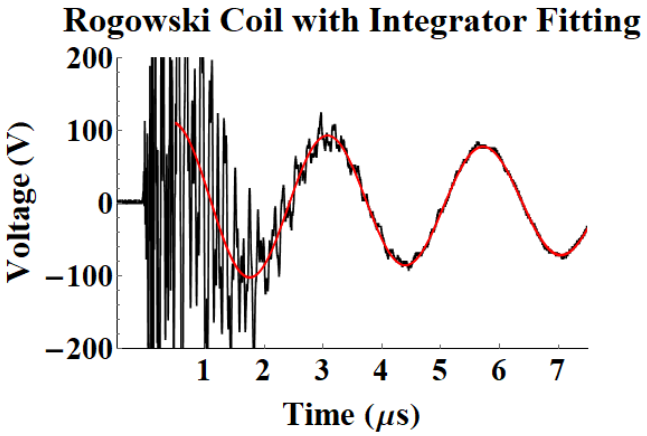

(b)

Figure 51: (a) The I_{in} and V_{RC} data of the Rogowski coil without the integrator. (b) The curve fitting of the V_{RC} data. (c) The integration of the V_{RC} curve fitting.

in figure 50 was conducted. We only added the RC integrator downstream of the Rogowski coil and integrate the V_{RC} through the RC integrator to get V_{out}. In figure 52, we show the measurement using the Pearson current monitor I_{in} in blue. The measurement using Rogowski coil with the integrator in red which is V_{out}. The I_{in} is fitted by Eq. 36 and the V_{out} is fitted using $ratio * I_{\text{in}}$ where $ratio = \frac{RC}{M}$. The parameters of I_{in} fitted by Eq. 36 are listed: $A = 2.39 \pm 0.03$ A, $\lambda = (-6.2 \pm 0.3) \times 10^4$ s, $\omega = (2.37 \pm 0.01) \times 10^6$ rad/s, $\phi = 0.6 \pm 0.1$ rad. The data is shown in appendix table 24. By Eq. 14, the ratio of the Rogowski coil with the integrator $\frac{RC}{M}$ was $(2.071 \pm 0.005) \times 10^4$ s/H and the delay time between I_{in} and V_{out} was $(1.3 \pm 0.2) \times 10^{-7}$ s. The data is given in appendix 25.

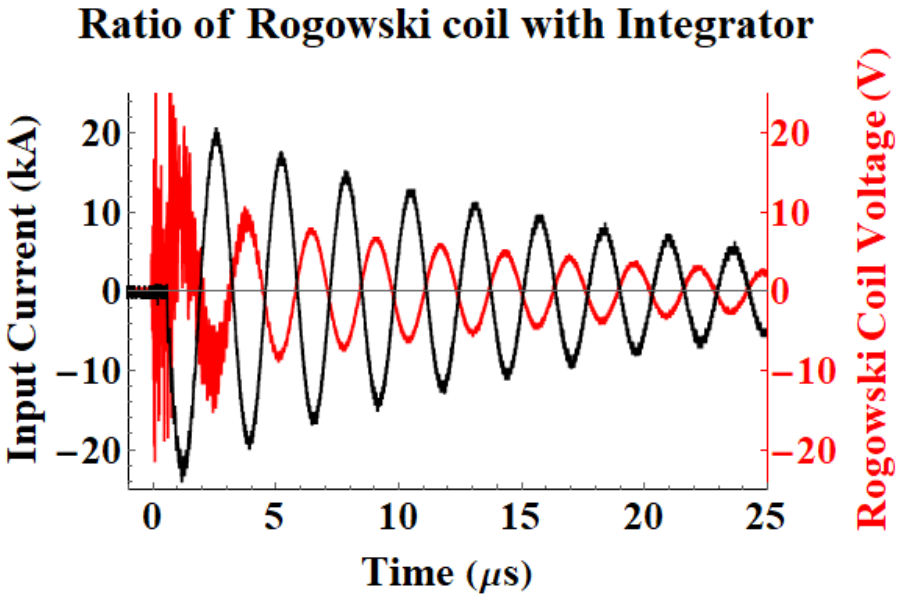

Figure 52: The I_{in} and V_{out} data of the Rogowski coil with the integrator.

doi:10.6844/NCKU202000512

In summary, the mutual inductance of the Rogowski coil M was $(1.812 \pm 0.008) \times 10^{-9}$ H, the ratio of the Rogowski coil with the integrator $\frac{RC}{M}$ was $(2.071 \pm 0.005) \times 10^4$ s/H, and the delay time between the output of in the Rogowski coil with the integrator was $(1.3 \pm 0.2) \times 10^{-7}$ s.

4.2 Visible light camera

We use a regular camera to film the discharge of the conical-wire array in visible light. The operating procedure is listed below:

1. Build the conical-wire array inside the vacuum chamber.
2. Use the vacuum pump with the uninterruptible power supply (UPS) to pump down the pressure to 5×10^{-6} torr in the vacuum chamber. The UPS is used to isolate the vacuum pump from the ground to prevent the damage of the discharge current.
3. Put the regular camera at the location opposite to the where people stand to avoid the x ray which will come from the discharge experiment.
4. Set up the regular camera whose camera model is NIKON D750, aperture is f/22, exposure time is 30 s, ISO is Lo 1 (equivalent to ISO 50), and focal length is 120 mm.
5. Set up the remote control of the regular camera to avoid operation by person in the discharge experiment area. After this step, person is not allowed to go into the discharge experiment area.
6. Charge up the capacitor banks by the HVPS to 20 kV.
7. Turn off the room light.
8. Use the remote control to turn on the regular camera. Because the exposure time is 30 s, we have enough time to conduct the next step.
9. Trigger the rail-gap switches to conduct the discharge experiment. The regular camera should capture the image of the discharge experiment.
10. After the exposure time is end, we can turn on the room light.
11. Wait 15 min and the capacitor banks should dump all remaining energy.

doi:10.6844/NCKU202000512

12. After this step, person is allowed to go into the discharge experiment area. Use the discharge rod to discharge the capacitors.

13. Vent the vacuum chamber.

After this procedure, we get the image of the discharge experiment. The result will be given in section 5.3.

4.3 The x-ray pinhole camera

The x-ray pinhole camera is used to take the image of the plasma jet inside the vacuum chamber. Figure 53 shows the flow chart of the pinhole camera. The triggering signal from the Marx generator is used as the time reference point. This signal is caught by a pickup coil which was introduced in section 3.3.2, The output of the pickup coil is used to trigger a pulse delay generator for timing control of all potential diagnostics. The delay generator will send a triggering signal with a chosen delay time to trigger the pinhole camera. After the pinhole camera captures the image of the plasma jet, it sends the image to the computer. The x-ray pinhole camera consists of two parts: one is the imaging system that converts the x-ray from the plasma jet into the visible light which is then captured by a regular camera; the other one is the controller which controls and provides powers for the imaging system. Specifically, the micro-channel plate (MCP) driver inside the controller controls the MCP which serves as the shutter of the pinhole camera. Therefore, the width of the signal of the MCP driver is very important to the x-ray pinhole camera. Figure 54 shows the time sequence of all events about the pinhole camera and the pulsed-power system. The starting trigger which sent from a function generator activated the trigger pulse generator. The trigger pulse generator sent a slow trigger pulse to activate the Marx generator. The Marx generator sent a fast trigger pulse to activate the pulsed-power system. In the meantime, the pickup coil got the time reference point from the fast trigger pulse. The pulsed-power system sent a discharging current to generate a plasma jet at the peak of the current. Before the plasma jet being generated, the pinhole camera started to film the plasma jet. The starting time was determined by a delay generator. After the plasma jet being generated, the pinhole camera stopped filming the plasma jet.

doi:10.6844/NCKU202000512

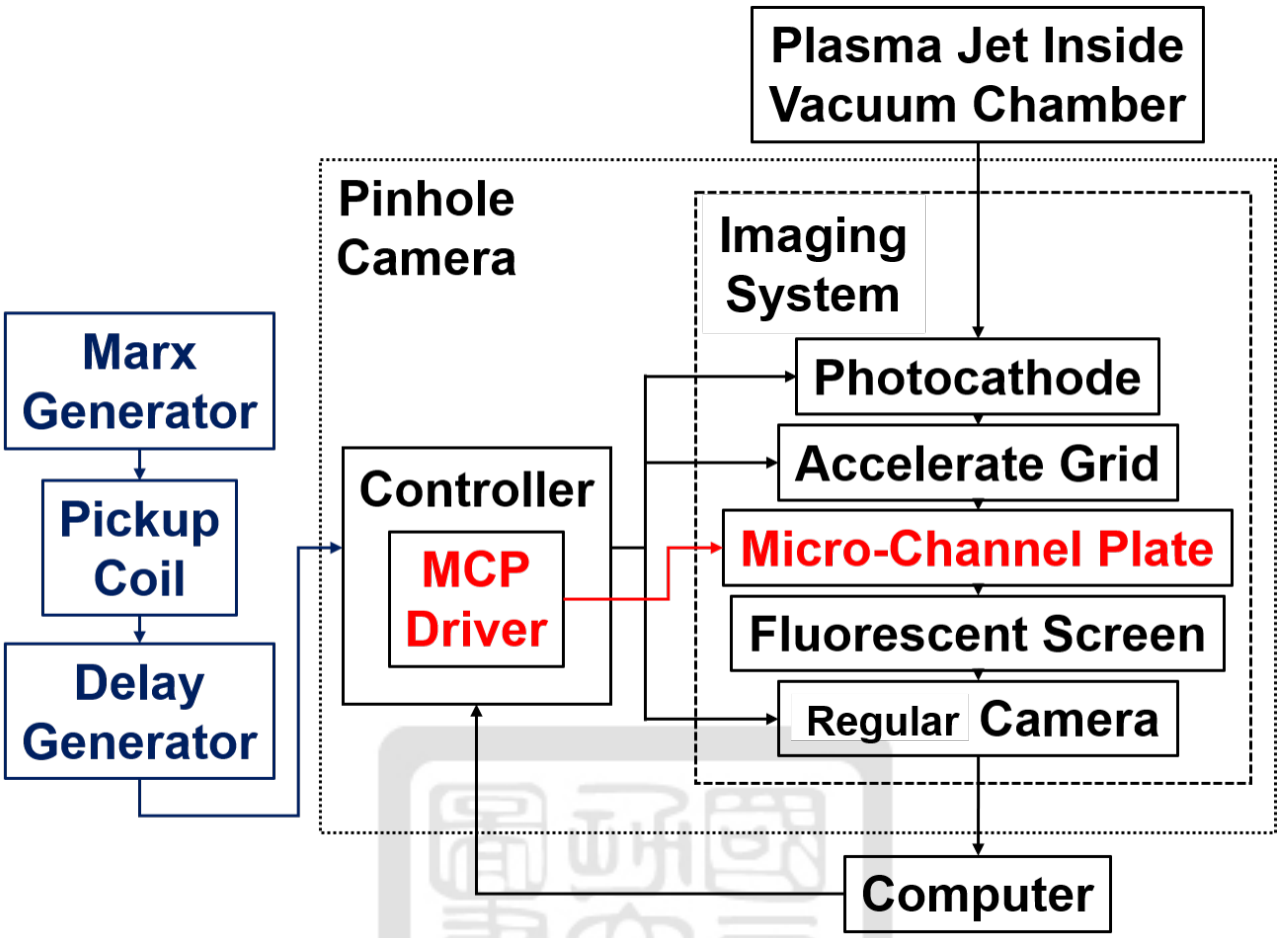

Figure 53: Flow chart of the pinhole camera.

4.3.1 Imaging system and the micro-channel plate (MCP)

Figure 55 shows the concept of the imaging system of the x-ray pinhole camera. The pinhole projects the x-ray image from the plasma jet on the photocathode emitting electrons. The accelerator grid is at ground while the photocathode is at -1 kV. The electrons are accelerated by the accelerator grid. The number of electrons are multiplied by up to 10^7 by the MCP which can be applied by a voltage up to 2.1 kV. Electrons eventually hit the fluorescent screen in the backside of the MCP. Finally, the fluorescent screen emits visible light which is captured by a regular camera. Figure 56(a) shows the structure of an MCP[18]. The MCP is a glass disk with many holes which are called the channels. The MCP we use is DV5615 (Chevron style) made by Baspik[19]. The diameter of the channels is 15 μm. The length to diameter ratio is 50. The typical center to center spacing is 19 μm. The resistance between two sides is ~ 0.1 GΩ. A 1-kV voltage is applied across both sides of the MCP generating a strong electric field along each channel. Figure 56(b) shows a channel of the MCP. The inner channel wall has

doi:10.6844/NCKU202000512

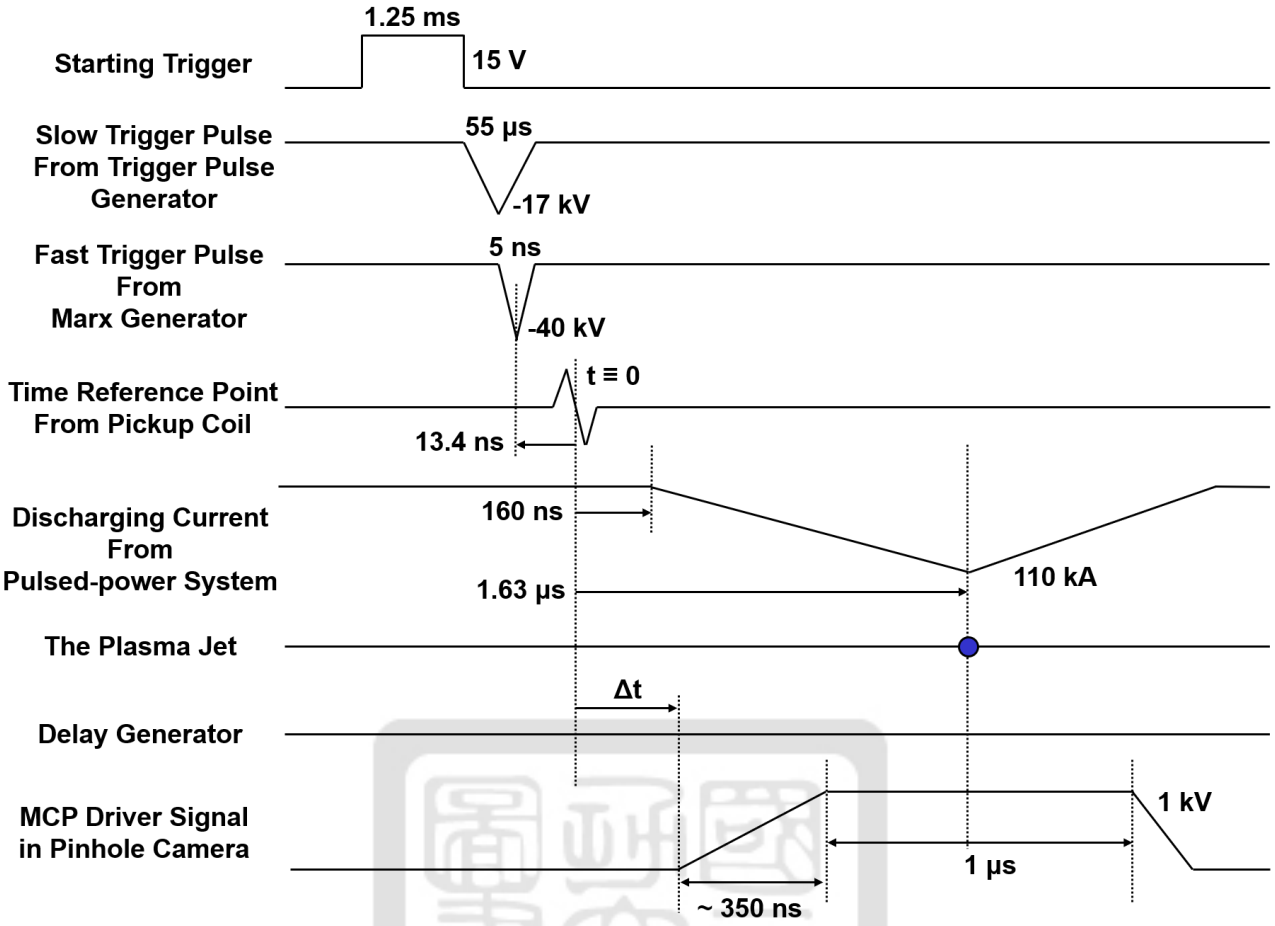

Figure 54: The Gantt chart of the pinhole camera with the information of the pulsed-power system.

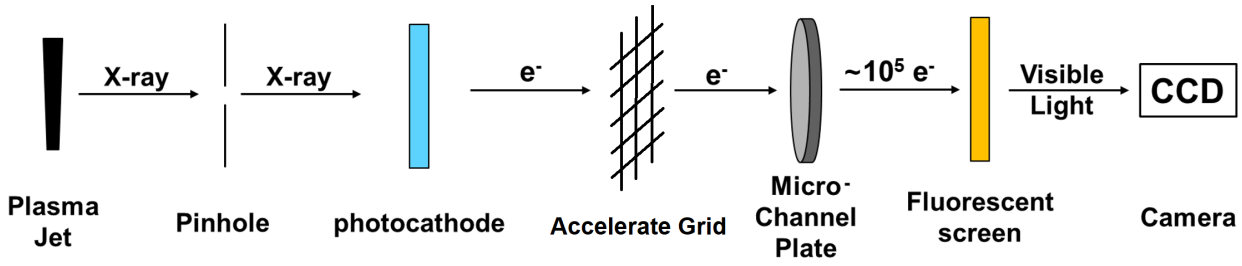

Figure 55: The flow chart of the optical devices part of the pinhole camera.

a semiconducting layer that generates two secondary electrons when a primary electron strikes. When a secondary electron is generated, it is accelerated by the strong electric field. After it strikes the semiconducting layer again, it will generate two tertiary electrons and this process continues. Thus, a channel will generate 10^4 to 10^7 (up to 10^7 in our MCP) output electrons from a primary electron. However, if no voltage is provided across the MCP, the number of electrons will not be increased. If a high-voltage pulse is used, the number of electrons is only increased when the high voltage is presence. In other words, the MCP behaves as an electrical

doi:10.6844/NCKU202000512

shutter. The pulse width of the pulse is the exposure time. To provide an exposure time of

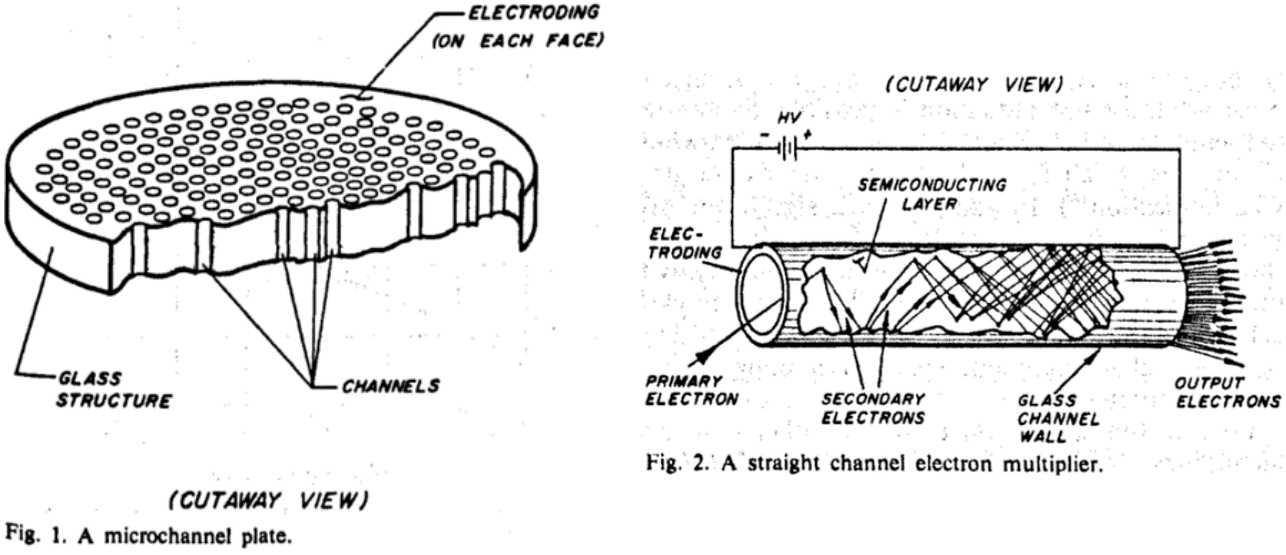

(a) (b)

Figure 56: (a) A micro-channel plate. (b) A straight channel electron multiplier.

1 μs, the MCP as a shutter in the pinhole camera needs a 1 kV voltage in 1 μs. Therefore, an MCP driver is built for generating a 1 kV pulse with a pulse-width of 1 μs.

4.3.2 The concept of the MCP driver

The MCP driver is built for generating the 1-kV pulse with a pulse-width of 1 μs for gating the x-ray pinhole camera. The function of the MCP driver is to convert a transistor-transistor logic (TTL) signal (i.e. a 5-V square pulse) to a 1-kV square pulse. The information of all components are listed in Table 6 at the end of this section. Figure 57(a) shows the overview flow chart of the MCP driver. The input of the MCP driver is a function generator in this test or a delay generator in reality. The output of the MCP driver is an oscilloscope in this test or an MCP in reality. The MCP driver is supplied by a high voltage power supply (HVPS) in this test or an HVPS module in reality. The MCP driver has three components which are the MOSFET driver, Both MOSFETs are n type[20]. the MOSFET for positive signal called the MOSFET 1, and the MOSFET for negative signal called the MOSFET 2. Each MOSFET has three electrodes: gate (G), source (S), and drain (D). The function of the MOSFET is a switch. When the voltage between the gate and the source of the MOSFET is at high level (15 V), it's ON and the drain is connected to the source. When the voltage between the gate and the source of the MOSFET is zero, it is OFF and the drain is not disconnected from the

doi:10.6844/NCKU202000512

source. When the function generator sends a TTL signal to the MOSFET driver, the square pulse is divided into three steps: step 1 is at low voltage, step 2 is at high voltage, and step 3 is at low voltage. The MOSFET driver then sends a normal square pulse to the MOSFET 1 and an inversed square pulse to the MOSFET 2. Therefore, the status of the MOSFET 1 is OFF, ON, then OFF while the status of the MOSFET 2 is ON, OFF, then ON. Thus:

1. the MOSFET 1 is OFF and the MOSFET 2 is ON so the final output is at ground.
2. the MOSFET 1 is ON and the MOSFET 2 is OFF so the final output is high voltage.
3. the MOSFET 1 is OFF and the MOSFET 2 is ON so the final output is grounded again.

As a result, the driver sends a 1-kV square pulse if 1 kV is supplied by the HVPS.

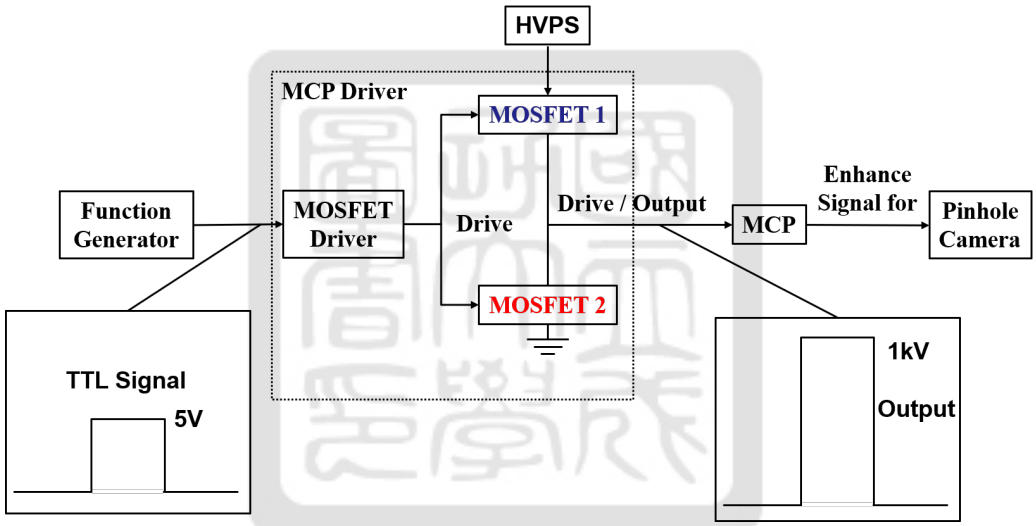

(a)

MOSFET 1	MOSFET 2	Output
OFF	ON	OFF
ON	OFF	ON
OFF	ON	OFF

(b)

Figure 57: (a) The overview flow chart of the MCP driver. (b) The states of the MOSFET 1 and/or MOSFET 2.

Figure 58(a) shows the flow chart of the MOSFET driver unit. The texts "5V P" next to the arrows means it's a 5-V positive square pulse which is shown in figure 58(b). The text "5V N" refers to a 5-V inversed square pulse or called negative square pulse. The texts "Optical P" and

doi:10.6844/NCKU202000512

"Optical N" represent square pulse and inversed square pulse, respectively, in optical form. The TTL signal is sent from the function generator and converted into an optical signal by the 1st optical transmitter. The reason for using optical coupling is to prevent the function generator from being damaged by the electromagnetic pulse (EMP) of the pulsed-power system. In the MOSFET driver unit, there are two parts which are the low voltage part and the high voltage part. In the low voltage part, after the optical receiver receives the optical signal from the function generator, the NOT gate inverts the positive signal into the negative signal and sends it to the coupler for MOSFET 2 and the 2nd optical transmitter. The 2nd optical transmitter sends an optical negative square pulse to the high voltage part. The 2nd optical transmitter is used to insulate the high voltage part from the low voltage part. The 2nd optical receiver in the high voltage part has a NOT gate function and invert the negative pulse back to the positive pulse which is sent to the coupler for MOSFET 1. The coupler for MOSFET 1 is used to drive the MOSFET 1. The MOSFET 1 is driven by the coupler for MOSFET 1 which receives a positive pulse. Similarly, the MOSFET 2 is driven by a coupler for MOSFET 2 which receives a negative pulse.

To explain the reason for separating the MOSFET driver unit into two parts, the principle of the MOSFET needs to be introduced. In figure 58(c), the MOSFET has three electrodes which are the gate (G), the drain (D), and the source(S). If the voltage between the gate and the source is at a high level, the drain and the source are connected. If the voltage between gate and source is at a low level, the drain and source are disconnected. Back to the figure 57(a), to turn the MOSFET 1 ON, the voltage of its gate V_{G} need to be higher than the voltage of its source V_{S}, i.e.,

$$V_{\mathrm{G}} = V_{\mathrm{S}} + \Delta V \tag{37}$$

where ΔV is the signal send to the gate of the MOSFET 1. To generate the V_{G}, the ground of the high voltage part is connected to the output of the MCP driver. Therefore, The V_{G} can satisfy Eq. 37. The ground of the high voltage part and the low voltage part have the 1-kV difference in the period of high voltage output. Thus, the two parts need the optical coupling to insulate the high voltage part from the low voltage part because the grounds of the two parts are different. Similarly, the high voltage part and the low voltage part are powered separately using two batteries.

doi:10.6844/NCKU202000512

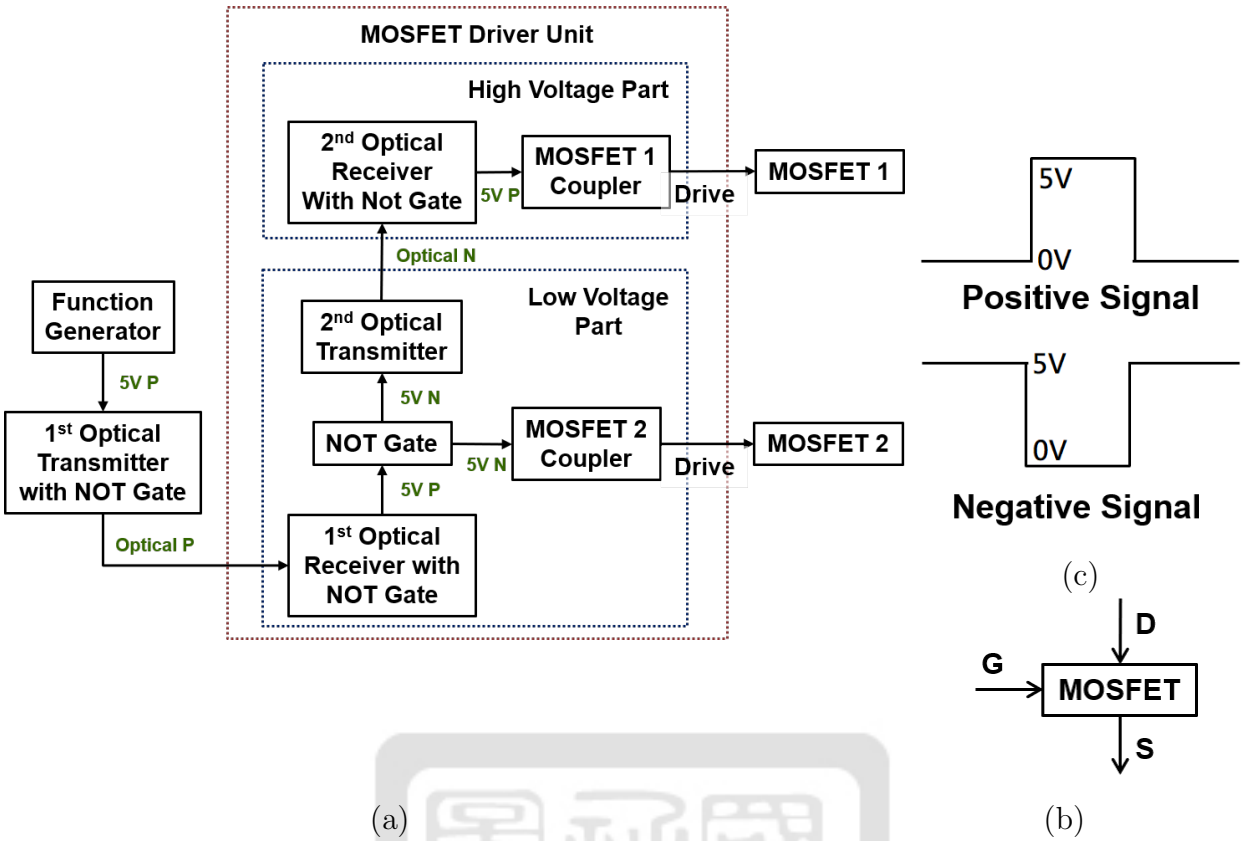

Figure 58: (a) The flow chart of the MOSFET driver unit. (b) The alias P is the positive square pulse and the alias N is the negative square pulse.

4.3.3 The MCP driver using IGBT

Before using MOSFET in the MCP driver, we used the IGBTs instead of MOSFETs to build the MCP driver. In figure 59(a), we show the schematic of testing the MOSFET driver IC using a function generator and an oscilloscope. The Vcc was 15V for testing. The MOSFET driver was an IC chip. The note in the figure provides the location and the corresponding number of each electrode. In figure 59(b), we show the TTL signal from the function generator in black, the positive pulse from the coupler for MOSFET 1 is in red, and the negative pulse from the coupler for MOSFET 2 is in blue. The time at the rising edge of the positive pulse t_{P1} was defined as the time from the rising edge of the TTL signal to the voltage of 50% of the maximum value. The t_{P1} was 0.12 μs, i.e. there was a 0.12-μs delay between the rising edge of the coupler for MOSFET 1 and the rising edge of the TTL signal. The time at the falling edge of the positive pulse t_{P2} was defined as the time from the falling edge of the TTL signal to the voltage of 50% of the maximum value. The t_{P2} was 1.21 μs. Therefore, The full width helf maximum (FWHM) $t_{P2} - t_{P1}$ was 1.09 μs. In addition, The time at the falling edge of the negative pulse t_{N1} was 0.22 μs and the time at the rising edge of the negative pulse t_{N2} was

doi:10.6844/NCKU202000512

1.14 μs. They were also defined as the time between the rising edge of the TTL signal and the voltage at 50% of the maximum value. The FWHM $t_{N2} - t_{N1}$ was 0.92 μs. The goal of the pulse width was around 1 μs and the delay should have been at least less than 1 μs. The FWHM of the positive signal and negative signal in figure 59(b) both satisfied the goal. The performance was good at this point.

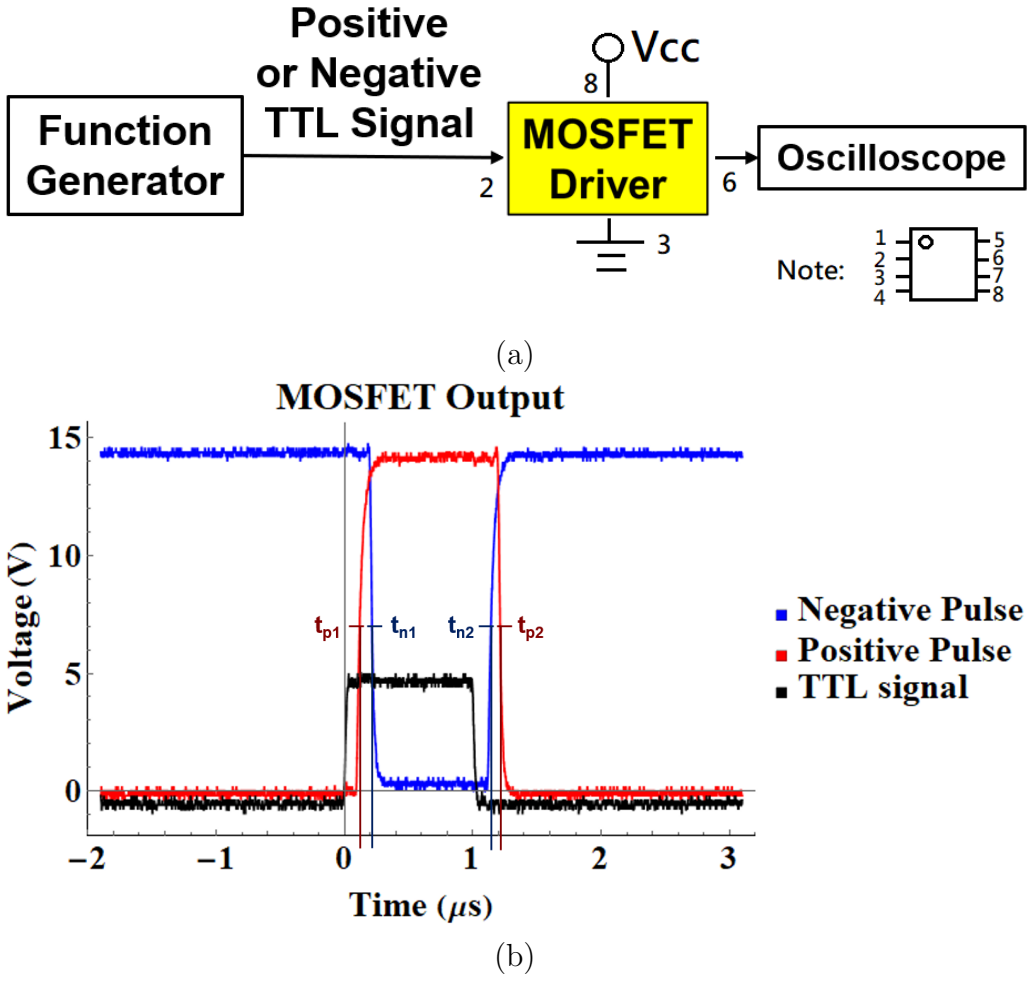

Figure 59: (a) The flow chart of the performance test of the MOSFET driver using positive or negative TTL signal. (b) The performance of the MOSFET driver.

In figure 60(a), we connected the output of the MOSFET driver into IGBTs[21]. Therefore, a TTL signal was sent to the MOSFET driver and the MOSFET driver output the signal to the gate electrode of IGBTs. The drain and source electrodes of the IGBT were not connected to other components. In figure 60(b), we show the TTL signal from the function generator in black, the positive pulse from the coupler for MOSFET 1 in red, and the negative pulse from the coupler for MOSFET 2 in blue. The results were: $t_{P1} = 0.57$ μs, $t_{P2} = 10.30$ μs, $t_{N1} = 0.25$ μs, and $t_{N2} = 10.62$ μs. The time at the rising edge of the positive signal t_{P1} was 0.57 μs, i.e. the MOSFET driver needed 0.57 μs to activate the IGBT. The voltage was 9.4 V at 1 μs and

doi:10.6844/NCKU202000512

the maximum voltage was 15 V. It meant the IGBT wasn't turned on at 1 μs, so it doesn't satisfy the goal. It was too slow to serve as the shutter of the pinhole camera.

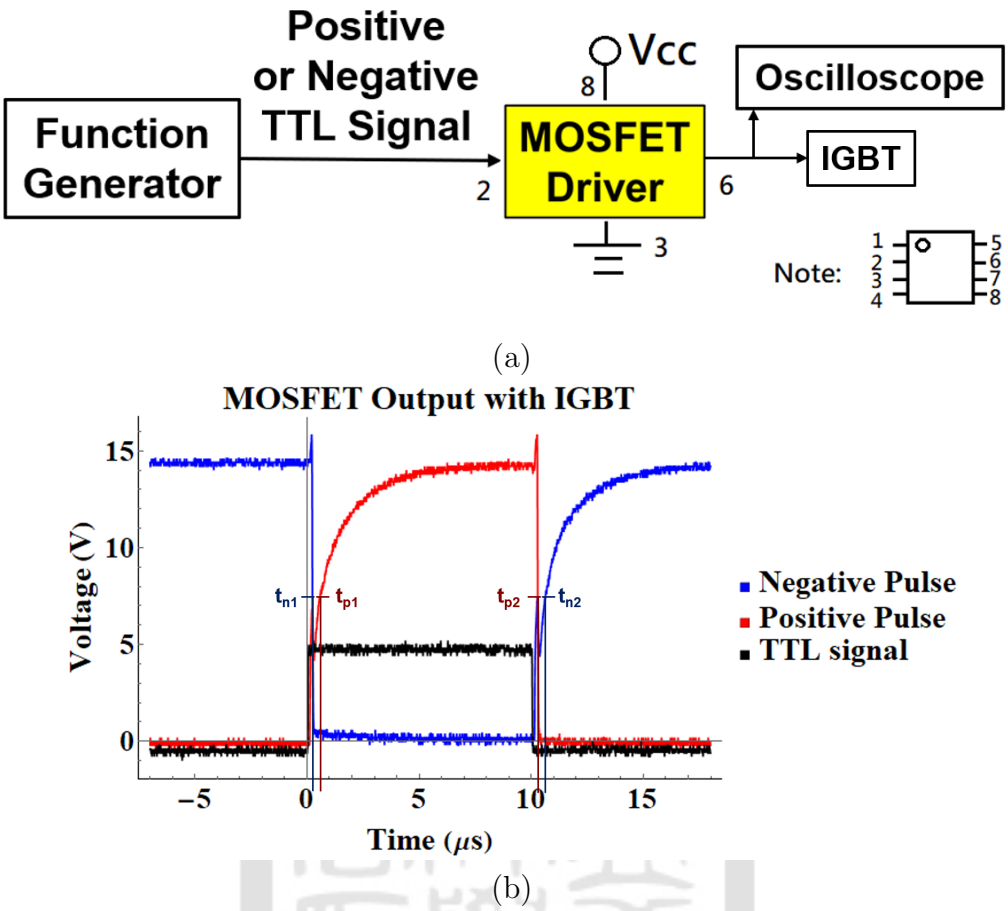

Figure 60: The flow chart of the performance of the MOSFET driver. (b) The performance of the MOSFET driver.

In figure 61(a), we show the circuit of testing the MCP driver using IGBTs. The function generator sent the TTL signal to the MCP driver, then the MCP driver sent the output voltage to an oscilloscope. The MCP driver was supplied by an HVPS. We tested the MCP driver in different supplied voltage from the HVPS with supply voltage up to 600 V. The supply voltage was changed from 100 V to 600 V in a step of 50 V. The 600 V was the upper limit of the IGBT. Figure 61(b) shows an example of the input TTL signal and the output voltage using 600 V as the supplied voltage. The rising time at 60% and 90% times of the maximum were defined as $T_{0.6\,\mathrm{max}}$ and $T_{0.9\,\mathrm{max}}$, respectively, and the falling time was T_{final}. The FWHM of this example was 8.9 μs. Figure 62(a) shows $T_{0.6\,\mathrm{max}}$, $T_{0.9\,\mathrm{max}}$, and T_{final} at different charging voltage. The rising time at 0.6 and 0.9 times of maximum were $T_{0.6\,\mathrm{max}} = 1.64$ μs and $T_{0.9\,\mathrm{max}} = 2.47$ μs at 600 V. The falling delay time was $T_{\mathrm{final}} = 0.75$ μs at 600 V. Figure 62(b) shows the charging voltage of the HVPS and the highest output voltage of the MCP driver. The FWHM of the

doi:10.6844/NCKU202000512

(a)

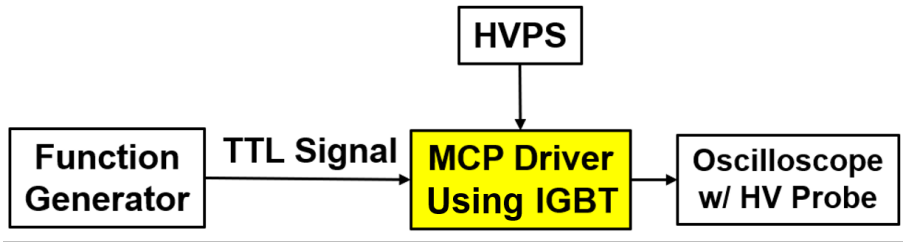

(b)

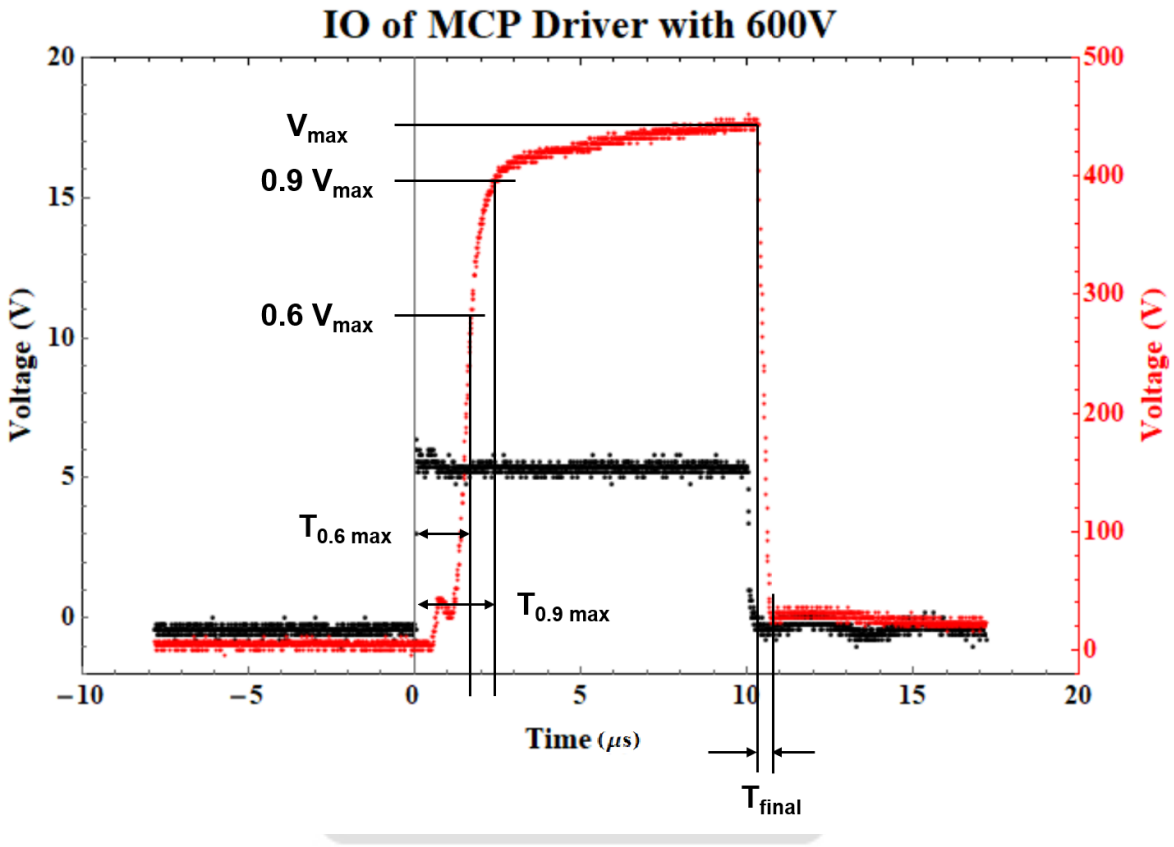

Figure 61: (a) The flow chart of the performance test of the MCP driver with IGBT. (b) The highest output voltage data of the MCP driver.

MCP driver using IGBTs is shown in figure 63. The data is shown in appendix 26. The goal of the time of the shutter is 1 μs and the maximum voltage is 1 kV. Because both the rising time and the maximum voltage does not satisfy this goal, we replace the IGBT by the MOSFET.

doi:10.6844/NCKU202000512

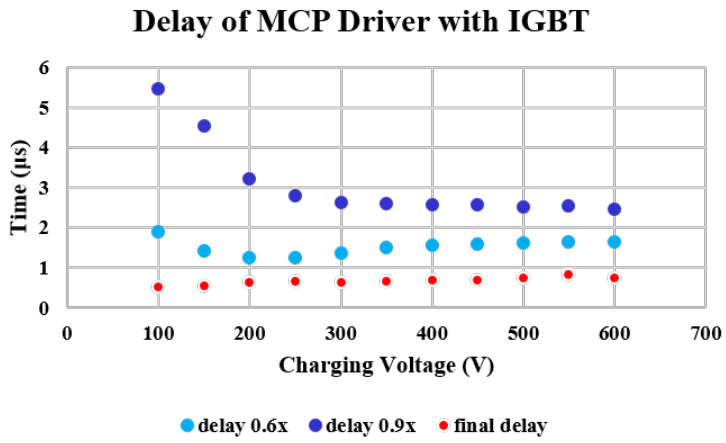

(a)

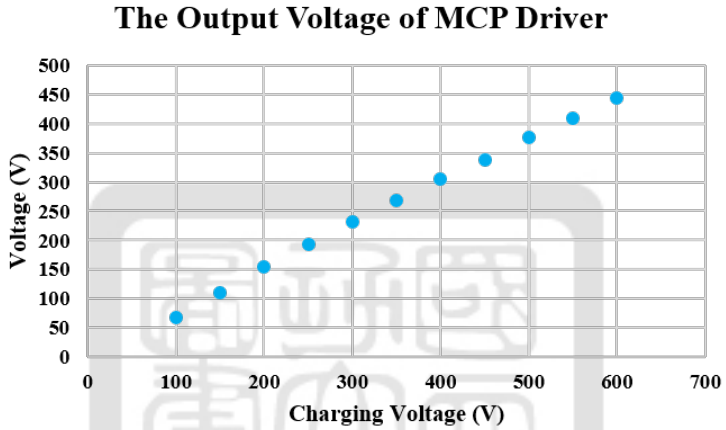

(b)

Figure 62: (a) The delay time of the rising edge of the MCP driver. (b) The output voltage of the MCP driver.

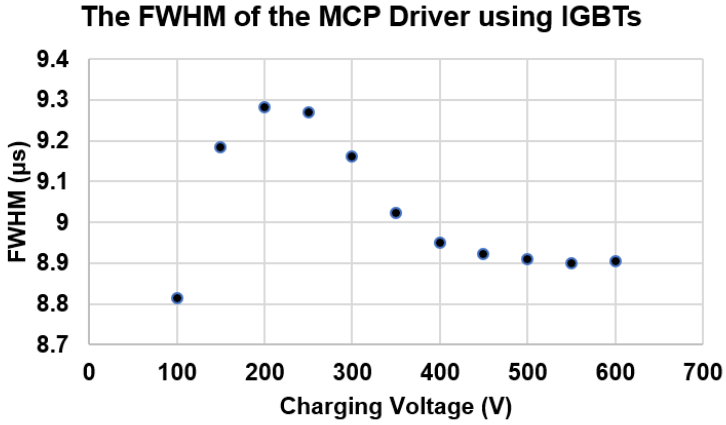

Figure 63: The FWHM of the MCP Driver using IGBTs.

doi:10.6844/NCKU202000512

4.3.4 The MCP driver using MOSFET

Figure 64(a) shows a similar test of the MCP driver using the MOSFETs. Figure 64(b) shows an example of the input TTL signal and the output voltage using 1 kV as the supply voltage. The rising time at 60% and 90% of the maximum were $T_{0.6\,\max}$ and $T_{0.9\,\max}$, respectively, and the falling time was T_{final}. Figure 65(a) shows $T_{0.6\,\max}$, $T_{0.9\,\max}$, and T_{final} at different charging

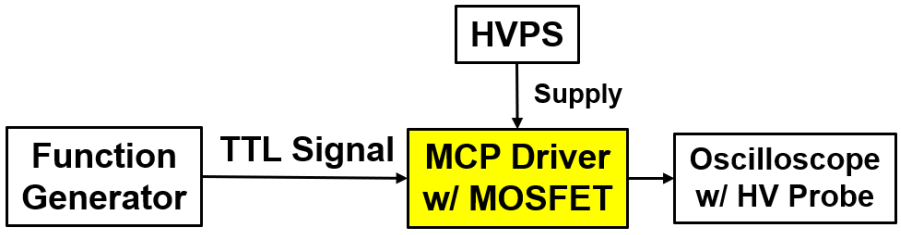

(a)

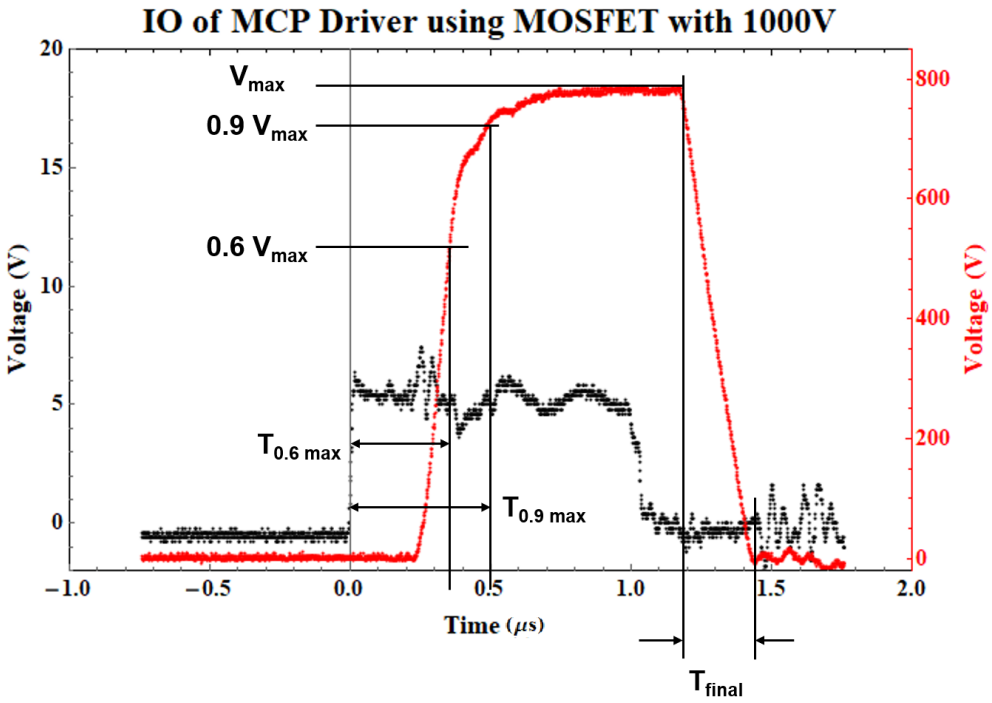

(b)

Figure 64: (a) The flow chart of the performance test of the MCP driver with MOSFET. (b) The highest output voltage data of the MCP driver.

voltages. The rising time at 60% and 90% of the maximum were $T_{0.6\,\max} = 0.34$ μs and $T_{0.9\,\max} = 0.47$ μs at 1 kV. The falling delay time was $T_{\text{final}} = 0.41$ μs at 1 kV. The FWHM of the MCP driver using MOSFETs is shown in figure 66. Because this is an electronic circuit and the errors were smaller than 10 ns, the error bars cannot be shown on the figure. The FWHM is less than 1 μs. Besides, the maximum voltage was closed to 1 kV. Thus, the MOSFET is chosen instead

doi:10.6844/NCKU202000512

of the IGBT. The data is shown in Table 27.

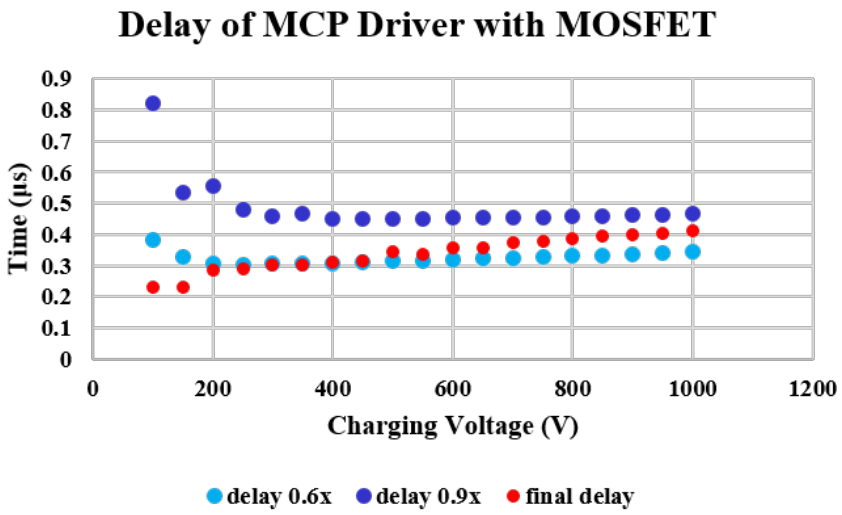

(a)

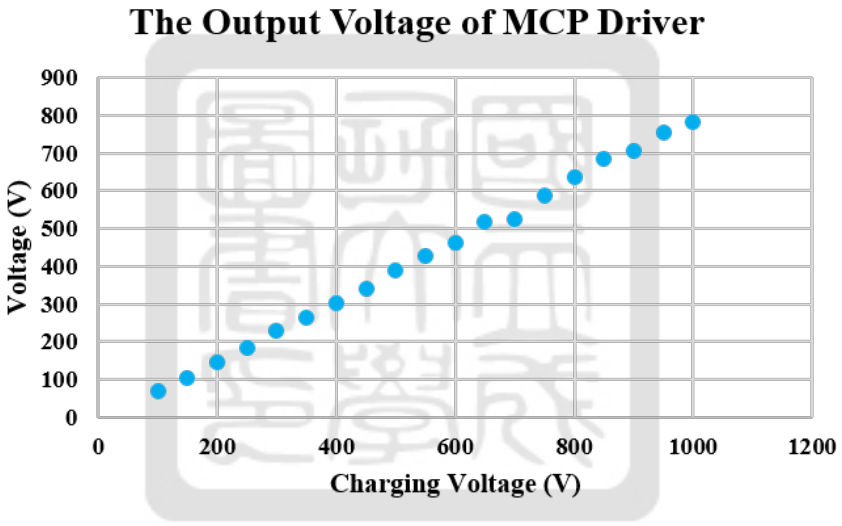

(b)

Figure 65: (a) The delay time of the rising edge of the MCP driver. (b) The output voltage of the MCP driver.

doi:10.6844/NCKU202000512

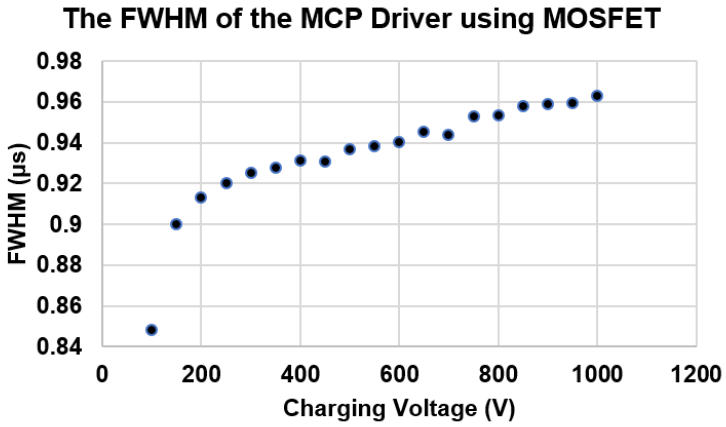

Figure 66: The FWHM of the MCP driver using IGBTs.

In summary, the MCP driver converts the TTL signal from a function generator or delay generator to a 1-kV square pulse for MCP. The MCP driver is the most important component of the pinhole camera controller in the next section. The reference of all components are listed in Table 6. The circuit diagram and layout are in section A.5.

Table 6: The components part numbers and references.

Component	Part Number	Reference
IGBT	IXXK110N65B4H1	[21]
DC-DC converter	DKE10 series	[22]
MOSFET dirver	FOD3184	[23]
NOT gate	SN74HC04APWR	[24]
MOSFET	SCT3160KL	[20]
optical coupling	HFBR1527, HFBR2528	[25]

4.3.5 The pinhole camera controller

The pinhole camera controller contains electric components of the x-ray pinhole camera. In general, the pinhole camera controller not only provides a high voltage between the photocathode and the accelerator grid but also sends the high voltage pulse to MCP from the MCP driver. Besides, the regular camera communicates through a data acquisition card (DAQ card) in the pinhole camera controller. In figure 67, blue arrows mean components pointed by the arrows are powered by the components connected to the backside of those arrows. The red arrows show the signal transmitted direction. About the power for all components, the pinhole camera controller has an external and replaceable battery connected to a bus. The voltage of the battery is 24 V. Therefore, all components which need power are connected to the battery

doi:10.6844/NCKU202000512

through the bus. To activate the MCP, the signal which comes from the delay generator goes to the MCP driver. Therefore, a high voltage square pulse is converted by the MCP driver and sent to the MCP. To control the whole system, a control signal is sent from a computer is controlled by a Labview program. The signal is sent through an optical USB for preventing damage of the computer by EMP. The HVPS control plate is used to send the power to two HVPSes. The DAQ card has two functions. One is to control the HVPS control plate. The other one is to communicate with the CCD. The HVPS control plate serves as the safety brake for the HVPS. The positive HVPS provide the high voltage for the MCP driver. The negative HVPS provides the high voltage between the photocathode and the accelerator grid.

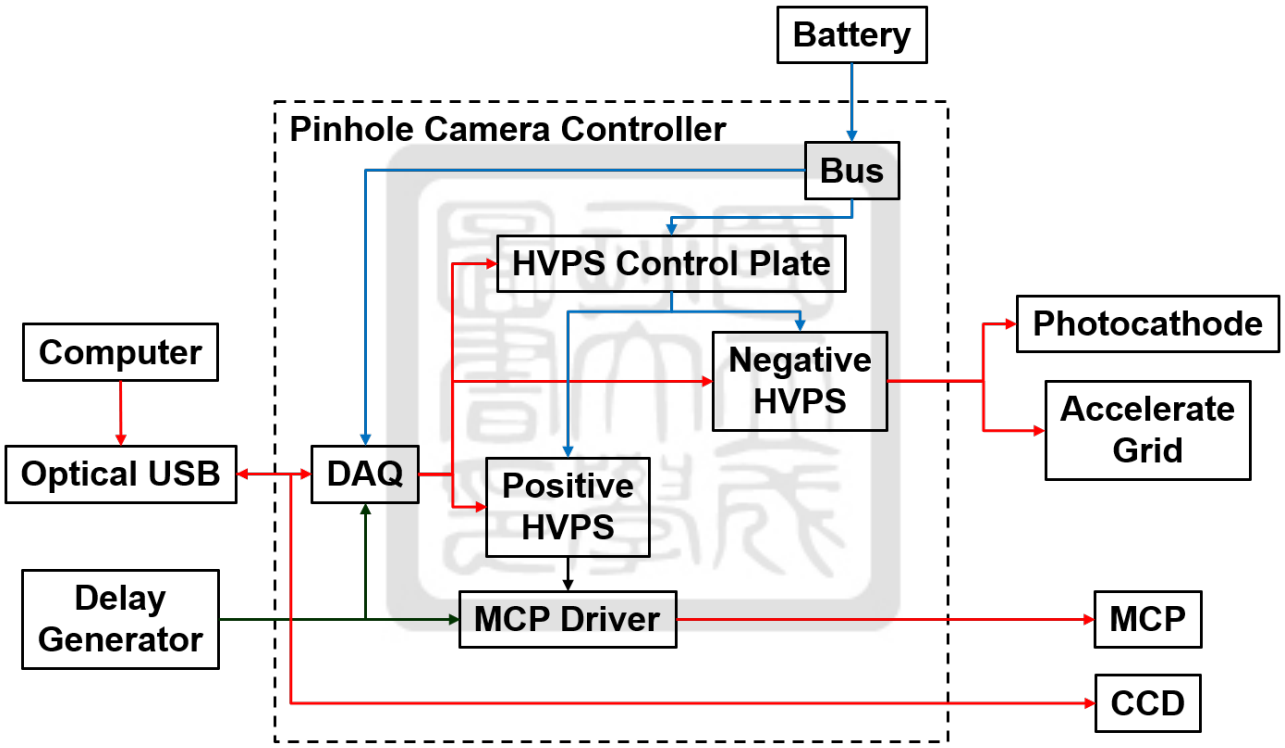

Figure 67: The circuit diagram of the pinhole camera controller.

In figure 68, the HVPS control plate is powered by a battery through a DC-DC converter which needs an input voltage between 18 V to 36 V. The relays, where the part number is BS-102B, are powered by the output of the DC-DC converter. The switch IC is used to enhance the controlling signal by the 24 V from the battery. It is powered by the DC-DC converter. The 500 Ω resistors are used to limit the current through the relays. When the relays are activated by the controlling signal, point N1 is connected to point N2 and the point P1 is connected to point P2 through the relays. The points N1 and P1 are connected to a DC-DC converter powered by the battery to provide the current for the HVPSes. Point P2 is connected

doi:10.6844/NCKU202000512

to the positive HVPS and point N2 is connected to the negative HVPS. The part number of the positive HVPS is Matsusada S1-1-5P-L2 and the pin definition is shown in Table 7. The part number of the negative HVPS is Matsusada HVR-3N-LW2 and the pin definition is shown in the Table 7.

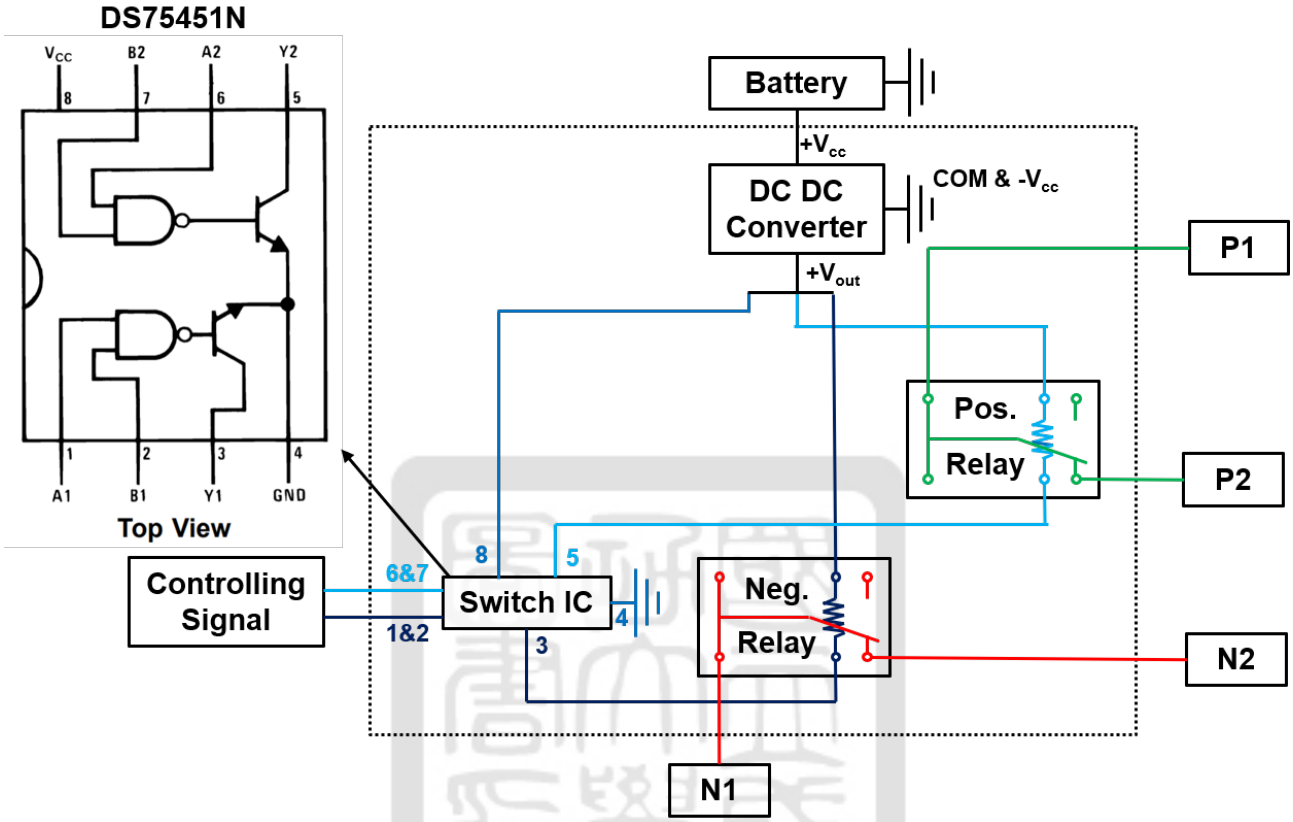

Figure 68: The circuit diagram of the HVPS control plate.

Table 7: The pin definition of positive and negative HVPS.

Positive HVPS		Negative HVPS	
Pin #	Function	Pin #	Function
1	V_{IN}	1	INPUT +12V DC
2	GND=CASE	2	GND=CASE
3	Sig-GND (CCW)	3	CCW
4	V_{CON-IN} (CW)	4	V_{CON-IN}
5	V_{REF} (CW)	5	VR 5KΩ
6	NC		
7	I_{MONI}		
8	V_{MONI}		

Figure 69 shows the Labview program which controls the HVPS control plate and HVPSes via the DAQ card. The .vi file is located in our lab cloud folder /shares/chieh/mcp%20lab-view/controller.vi.[26]. As shown in figure 69(a), to control the HVPS control plate and

doi:10.6844/NCKU202000512

HVPSes, we need an integer variable called the positive controlling signal which controls the output voltage of the positive HVPS and another integer variable called the negative controlling signal which controls the output voltage of the negative HVPS. Besides, we need two boolean variables called the positive signal relay and the negative signal relay to control the relays in the HVPS control plate. In figure 69(b), the upper limits of both HVPSes are set to ±1 kV. Because the voltage ratio between the input voltage and the output voltage of the positive and negative HVPS are 250 and 500, respectively, the voltage multipliers are needed in the code. There are 1/250 for the positive HVPS and 1/500 for the negative HVPS. We send the positive and negative controlling signal variables times their corresponding multiplier to the DAQ card within a while loop. For example, we set 500 V as the controlling signal variable to the positive HVPS. The 500 V times the 1/250, which is the multiplier of the positive HVPS, gives 2 V as the input voltage and is sent to the positive HVPS. When the pin #14 of the positive HVPS receives the 2V, it will output 500 V to the load. Next, we send the positive and negative signal relay variable to the DAQ card in another while loop. When the signal are sent and the relays are activated, both positive and negative high voltages are provided.

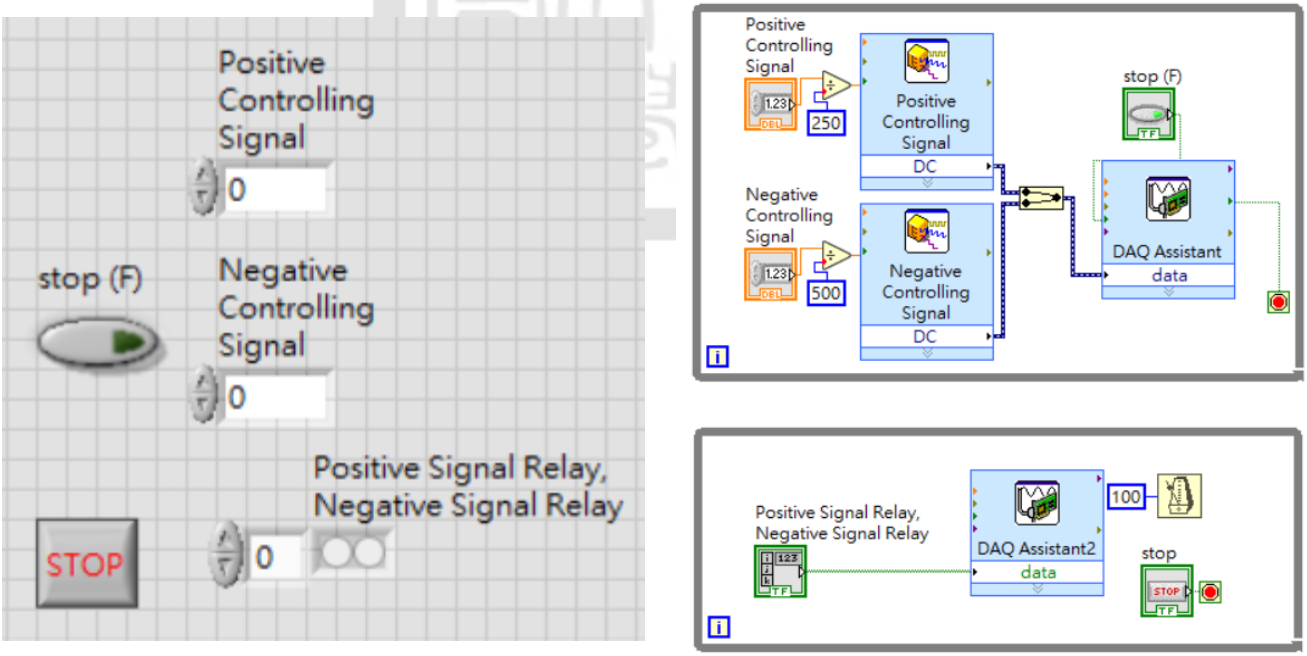

(a) (b)

Figure 69: The controlling method of the HVPS control plate and HVPSes using the DAQ card programmed by Labview software. (a) Front panel. (b) Block diagram.

A problem occurred due to the communication between the computer and DAQ while using the optical USB. At first, the communication was great and all functions could work perfectly.

doi:10.6844/NCKU202000512

However, the communication was interrupted for no reason exactly after every 30 seconds. If the optical USB was not used, the communication would not be interrupted. Thus, the problem was relative to the optical USB. The 100 ms timer was used to slow down the communication speed to postpone the interruption to 5 minutes. If the timer change to another time such as 200 ms, the interruption can be postponed longer but the communication speed would also be slower. The reason of this problem was unclear. Nevertheless, the delay timer help postpone the problem. The mechanical parts of the pinhole camera is under menufactured. The whole assembly will be the future works for the next students in the lab.

In summary, the pinhole camera controller has three functions: (1) to control and supply the high voltage between the photocathode and the accelerator grid using the HVPS control plate and HVPSes. (2) to generate a 1 kV square pulse to the MCP which acts as the shutter of the pinhole camera. (3) to communicate with the regular camera using the DAQ card which will be programmed in the future.

doi:10.6844/NCKU202000512

5 Plasma jet generations

The goal of this thesis is to generate plasma jets. We use conical-wire arrays driven by the pulsed-power system we built to generate the plasma jets.

The conical-wire array is used to generate the plasma jet. In figure 70, when the current goes through the metal wires, the ohmic heating will heat, vaporize and ionize the metal so that the plasma is generated. With the magnetic field generated by the current, the J×B force pushes the plasma toward the center. When the plasma collides at the center of the conical-wire array, it will generate a plasma jet propagating toward the top of the wire array. We use a model to estimate the required diameter of the metal wires. The model uses a long and thin cylinder shell for conducting currents. The cylinder shell is made by the plasma. The J×B force compresses the cylinder shell toward the center. On the other hand, the force generated by the inner pressure resists the cylinder shell from being compressed to infinitely small volume. For a given current profile, one can find the condition of mass per unit length of the cylindrical thin shell where most of the energy in the capacitor bank is converted to the plasma. Finally, the optimized diameter of the wire is determined.[1] A model for estimating the wire diameter will

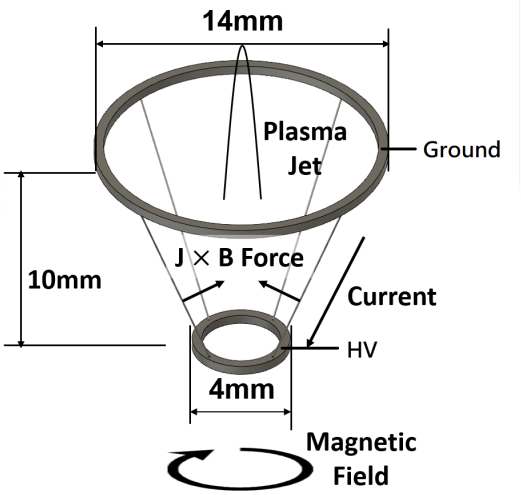

Figure 70: The conical-wire array.

be introduced in section 5.1. Finally, the implosions of conical-wire arrays will be presented in section 5.3.

doi:10.6844/NCKU202000512

5.1 Estimation of the requirement of the wire diameter

The diameter of the tungsten wires is important in generating the plasma jet. In figure 71, the current generated by the pulsed-power system has a peak of -110 ± 20 kA. The diameter of the tungsten wires determines the time when the plasma jet is generated. If the diameter of the wires is chosen carefully such that the plasma jet is generated at peak current, it will receive the most of the energy from the pulsed-power system. Figure 72(a) shows a simplified model to

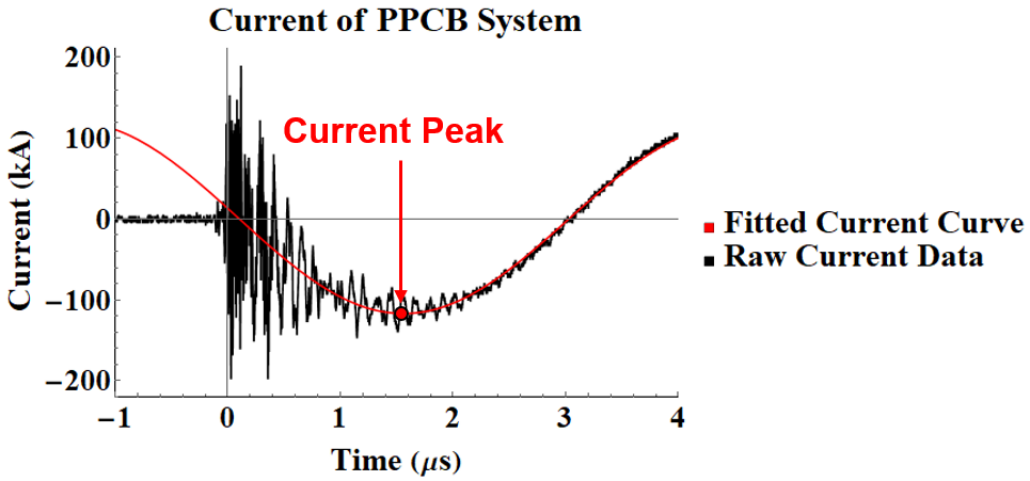

Figure 71: The current generated by the pulsed-power system.

estimate the required diameter of the tungsten wires[27]. We simplified the conical-wire array to this thin cylinder shell model for estimating the best diameter of the wires. The infinitely thin cylinder shell is filled with plasma. Its length is l. The radius is r, and the mass is m. The current generated by the pulsed-power system is I and the magnetic field generated by the current is B. Therefore, the $J \times B$ force that the plasma received is F. Consider a slice of the thin cyclinder shell, the mass of the slice is $\hat{m} = \frac{m}{l}$ and the force per slice is f. From Ampere's law and the Lorentz force equation, the momentum equation that we can get from Ref.[27] is

$$f = \frac{\hat{m}}{2\pi r}\ddot{r} = -\frac{\mu I^2}{8\pi^2 r^2} \tag{38}$$

where μ is the vacuum permeability. To explain Eq. 38, we change it to the form

$$\hat{m}\ddot{r} = -\frac{\mu I^2}{8\pi^2 r^2} \cdot 2\pi r = -\frac{1}{2\mu} \cdot (\frac{\mu I}{2\pi r})^2 \cdot 2\pi r = -\frac{B^2}{2\mu} \cdot 2\pi r \tag{39}$$

where $\hat{m}\ddot{r}$ is the force per slice f, $\frac{\mu I}{2\pi r}$ is the magenetic field B, $\frac{B^2}{2\mu}$ is the magenetic pressure per slice, and the $2\pi r$ is the perimeter of the slice. The momentum equation tells the force per

doi:10.6844/NCKU202000512

slice f is the magenetic pressure of the slice $\frac{B^2}{2\mu}$ times the area per slice which is the perimeter of the slice $2\pi r$. Note that the area is the area of the cyclinder side wall $2\pi r \cdot l$ and the area per slice is the area divided by the length of the cyclinder $\frac{2\pi r \cdot l}{l} = 2\pi r$. To simulate Eq. 38 using the computer, it is rewritten in a dimensionless form

$$\widetilde{r}\ddot{\widetilde{r}} = -\Pi\, \widetilde{I}^2 \tag{40}$$

where $\widetilde{r} = \frac{r}{r_0}$, $\widetilde{t} = \frac{t}{\tau}$, $\widetilde{I} = \frac{I}{I_{\max}}$, and $\Pi = \frac{\mu I_{\max}^2 \tau^2}{4\pi \hat{m} r_0^2}$. The r_0, τ, and $I_{\max}$ are the characterstics

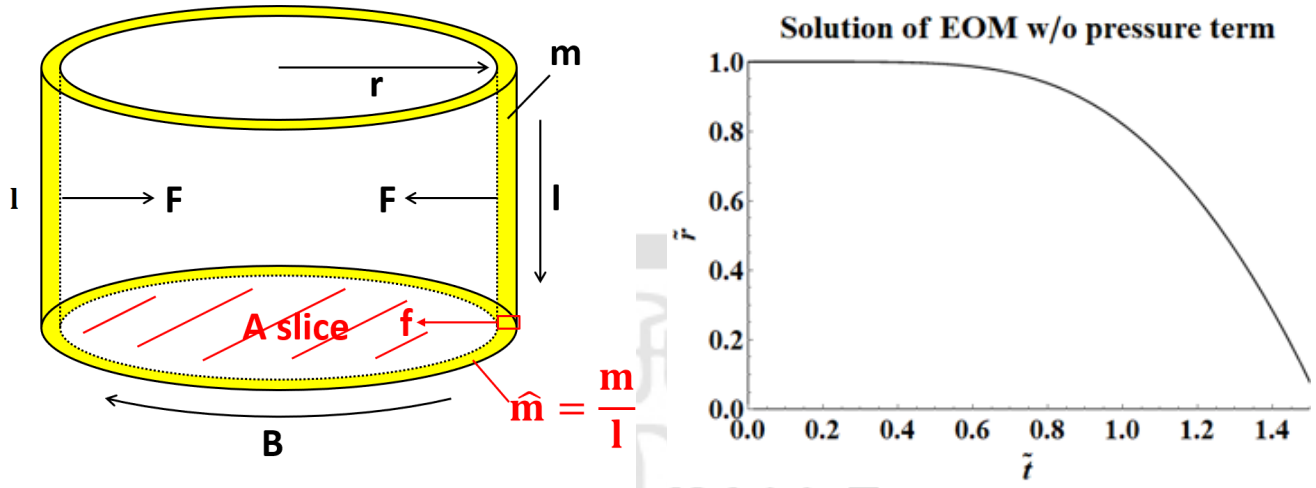

(a) (b)

Figure 72: (a) The thin cylinder shell model. (b) The solution of Eq.40 when $\hat{m}$ is 10 μg/m.

parameters. Note that some parameters are converted back to the dimensional one, because they are easier to explain and compare with the real value. The r_0 is chosen as 11.5 mm which is the averaged radius of the conical-wire array. The τ is chosen as 1.5 μs which is the time of the peak current. The $I_{\max}$ is 110 kA which is the peak current value. $\widetilde{I}$ is chosen as $\sin^2(\frac{\pi}{2}\widetilde{t})$ but only half of the first phase was used, i.e. $0 < \widetilde{t} < 2$. The numerical method was used to find a proper $\hat{m}$ such that the minimum of the $\widetilde{r}$ is at $\widetilde{t} = 1$. In another word, it's to find a proper mass of the thin cylinder shell such that the plasma merges when the current is at peak. Therefore, the plasma jet receives the maximum energy from the capacitor bank. Figure 72(b) shows the solution of the dimensionless equation when $\hat{m}$ is 10 μg/m. The problem was that this solution didn't have a minimum $\widetilde{r}$. It's because we only consider the J×B force which direction is inward and no balancing force that can slow down the imploding plasma. Therefore, we add a gas pressure term, which direction is outward, as follows

doi:10.6844/NCKU202000512

$$\frac{\hat{m}}{2\pi r}\ddot{r} = -\frac{\mu I^2}{8\pi^2 r^2} + P \tag{41}$$

where P which is the gas pressure from the remaining gas in the vacuum chamber. The implosion happens in a short period, i.e., the implosion is an adiabatic compression. Thus, we use the adiabatic condition for simplification, i.e.,

$$P_0 \mathrm{V}_0{}^{\gamma} = P\mathrm{V}^{\gamma} \tag{42}$$

where $P_0 \approx 10^{-5}$ torr and $\gamma = \frac{5}{3}$ for monoatomic molecules which simulate the argon gas inside the vacuum chamber. The dimensionless equation for Eq. 41 is

$$\widetilde{r}\,\ddot{\widetilde{r}} = -\Pi\,\widetilde{\mathrm{I}}^2 + \Phi\widetilde{r}^{-4/3} \tag{43}$$

where $\Phi = \frac{2\pi\tau P_0}{\hat{m}}$.

Figure 73 shows the solution of Eq. 41 for $\hat{m} = 2.292$ μg/m. The plasma is bounced back by the pressure from the compressed gas. We performed many runs with different $\hat{m}$ and find the best $\hat{m}$ where the minimum time point $t^* = 1$. Besides finding the time of peak compressions, we also calculated the energy. The total kinetic energy per unit length $\hat{E}_{\mathrm{kin}} = \frac{E_{\mathrm{kin}}}{l}$ is calculated

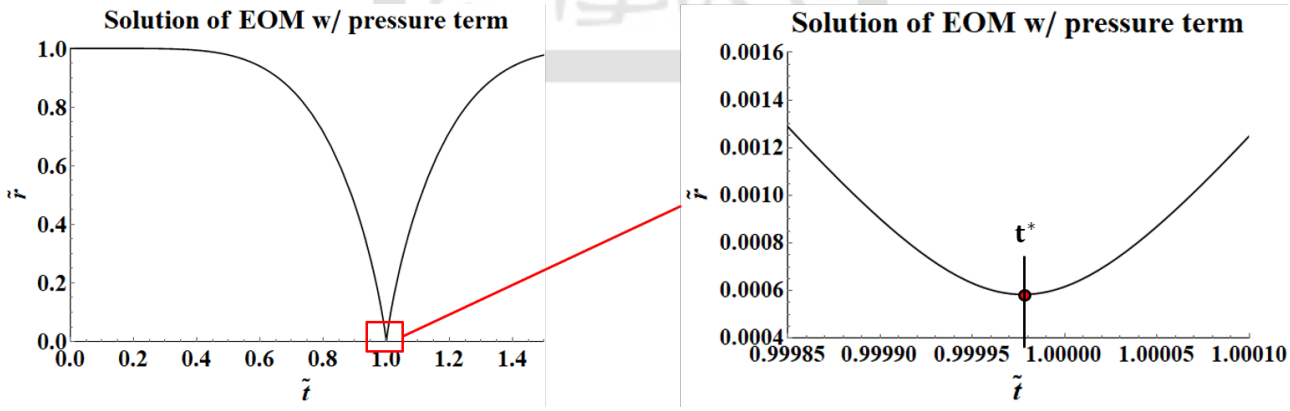

(a) (b)

Figure 73: The solution of $\widetilde{r}\ddot{\widetilde{r}} = -\Pi\widetilde{\mathrm{I}}^2 + \Phi\widetilde{r}^{-4/3}$ at $\hat{m}$ is 2.292 μg/m.

as follows

$$\hat{E}_{\mathrm{kin}} = \int \hat{F}\cdot ds = \hat{m}\int_0^{\widetilde{t}'} \dot{\widetilde{r}}\,\ddot{\widetilde{r}}\,d\widetilde{t} = W_{\mathrm{current}} + W_{\mathrm{pressure}} = u(\widetilde{t}')\,, \tag{44}$$

doi:10.6844/NCKU202000512

$$W_{\text{current}} = -\frac{\hat{m}{r_0}^2}{\tau^2}\Pi \int_0^{\widetilde{t}'} \frac{\dot{\widetilde{r}}}{\widetilde{r}} \widetilde{I}^2 d\widetilde{t} = v(\widetilde{t}') \,, \tag{45}$$

$$W_{\text{pressure}} = \frac{\hat{m}{r_0}^2}{\tau^2}\Phi \int_0^{\widetilde{t}'} \dot{\widetilde{r}}\, \widetilde{r}^{-\frac{7}{3}} d\widetilde{t} = w(\widetilde{t}'). \tag{46}$$

where $\hat{F} = \frac{F}{\mathrm{l}}$ is the force per unit length, W_{current} is the total work by current and W_{pressure} is the total work by pressure. Figure 74 shows the total kinetic energy in blue, total work by current in red and by pressure in black. Each point of the kinetic energy, total work by current and total work by pressure at time $\widetilde{t}' \in (0.9998, 1.0002)$ with a $\widetilde{t}'$ step size of 10^{-5} is calculated by $u(\widetilde{t}')$, $v(\widetilde{t}')$, and $w(\widetilde{t}')$, respectively. At peak compression, the total kinetic energy becomes 0 because the plasma stagnated at the center. Besides, the direction of force from the current is always inward. The work is positive during implosion but negative during explosion at peak compression. It is because the total work by current reaches maximum at stagnation. On the other hand, the direction of the gas pressure is always outward. The work is negative during implosion but possitive during explosion. the total work by pressure reaches minimum at peak compression. Figure 75(a) shows a series of simulation results by scanning $\hat{m}$ with a step of

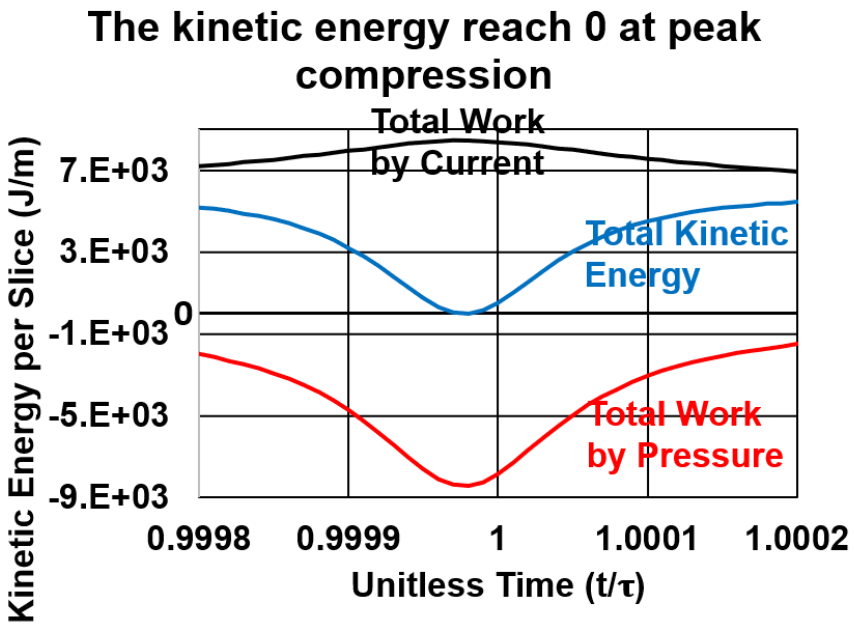

Figure 74: The total kinetic energy and the total work by current and pressure.

0.0001μg/m. The minimum time point of the solution t^* changes with different $\hat{m}$. When $\hat{m}$ is 2.292 μg/m, t^* reaches 1. Figure 75(b) shows that the total work by current per slice W_{current} changes with different $\hat{m}$. When $\hat{m}$ is 2.292 μg/m, W_{current} reaches maximum. Finally, the mass

doi:10.6844/NCKU202000512

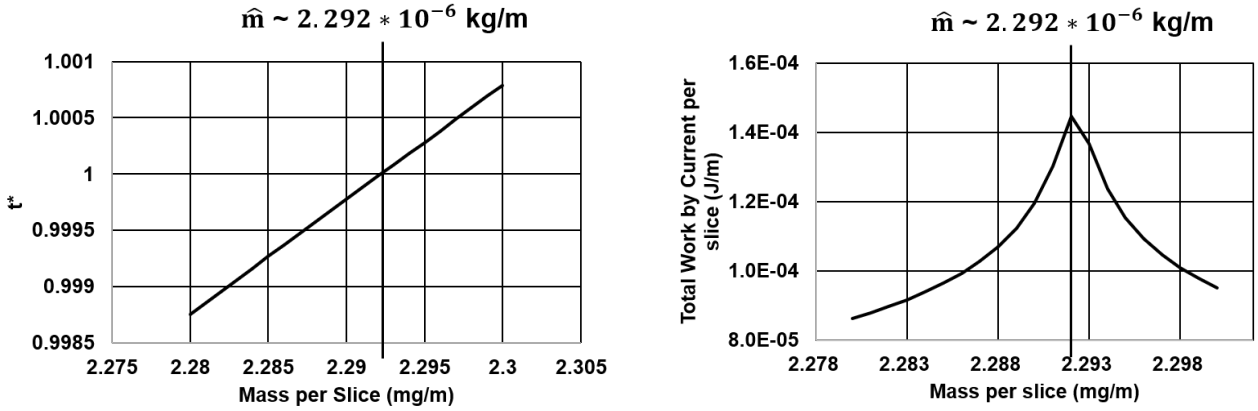

(a) (b)

Figure 75: (a) The t^*changing with different $\hat{m}$.(b) The W_{current} changing with different $\hat{m}$.

per unit length $\hat{m}$ is used to calculate the diameter of the tungsten wires by the equation

$$\hat{m} = n * \pi R^2 * \rho \tag{47}$$

where n is number of wires, R is the radius of wires, ρ is the density of tungsten. For $\hat{m} = 2.292$ μg/m, $n = 4$, and $\rho = 19.3$ g/cm^3, we get the radius R equal to 6.2 μm.

5.2 Design of our conical-wire array

Figure 76(a) shows the design of our conical wire array. It is mounted on the top of the coaxial transmission line in the vacuum chamber. The conical-wire array is mounted on the coaxial transmission line. Notice that the outer cylinder is grounded and the inner cylinder is at the negative high voltage when the system is activated. Therefore, the current goes from the outer layer of the coaxial transmission line to the support column, top support beam, top wire disk, conical-wire array, bottom wire disk, bottom support beam, and then the inner layer of the coaxial transmission line. The gap of the top wire disk is for observing the plasma jet from the window of the vacuum chamber in figure 76(b). Figure 77(a) shows the section view of the conical-wire array. There are eight grooves on the top and bottom wire disks for positioning the tungsten wires. The tungsten wires are fixed by the screws at the screw holes. 77(a) is a photo of the conical-wire array using 8 tungsten wires with 20 μm in diameter before the experiment. In this experiment, the diameter of the wire was 20 μm which was the finest we could get as far. We used 8 tungsten wires which are the maximum space utilization. Thus, this configuration

doi:10.6844/NCKU202000512

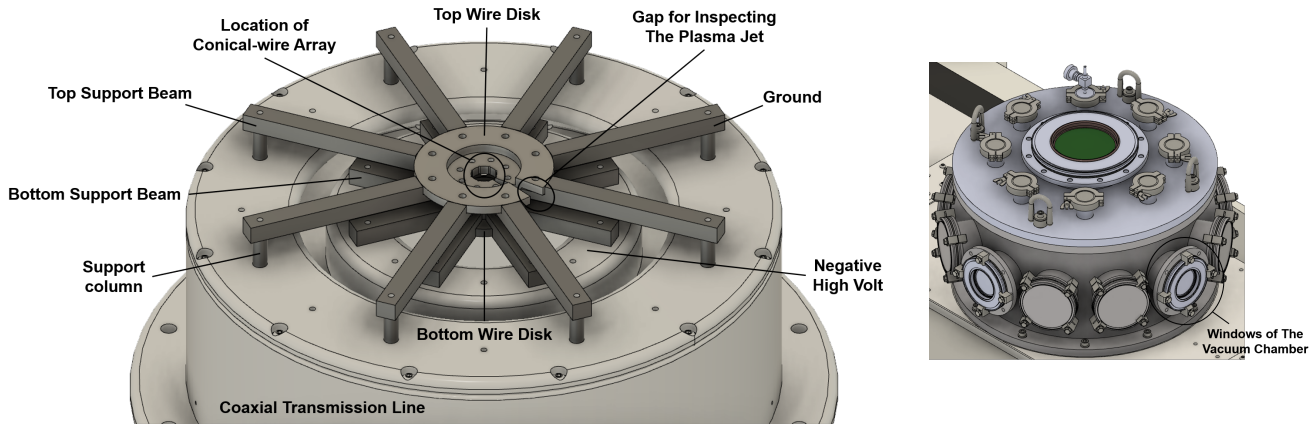

(a) (b)

Figure 76: (a) The design of the conical-wire array for the pulsed-power system. (b) The vacuum chamber and its windows.

was used to test the regular camera. The component drawings of the conical-wire array are listed in the appendix A.3.

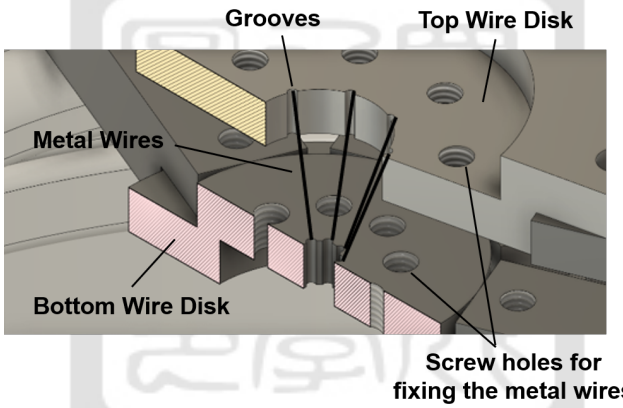

Figure 77: The section view of the conical-wire array.

5.3 Implosion of conical-wire arrays

Before finishing the x-ray pinhole camera, we used a regular camera to film the discharge of the conical-wire array in visible light. We use the whole system to drive the conical-wire array. Figure 78(a) shows the conical-wire array before the implosion. The wire width of the conical-wire array is 20 μm. This conical-wire array was built by a successor student Yen-Cheng Lin. While connecting these wires, the working space inside the vacuum chamber was quite narrow. Therefore, we decided to design a new wire disk to solve this problem. Figure 78(b) shows the time-integrated image of the implosion of the conical-wire array taken by a regular camera. The camera model is NIKON D750, the aperture was f/22, the ISO is Lo 1 (equivalent to ISO

doi:10.6844/NCKU202000512

50), the exposure time was 30 s, and the focal length is 120 mm. This image was overexposed so the detail at the conical-wire array can't be shown. There are some light traces. They should be the debris from the hot tungsten wires flying out. Figure 78(c) and (d) show the remaining wires after the discharge. Figure 78(c) is at the top wire support plate and the Figure 78(d) is at the bottom wire support plate. The discharging energy are large enough to blow up all of the wires. The remaining length of the wires are around 1.5 to 2 times of the thickness of the support plates. The regular camera could only take images in the visible light while some of the light generated by the plasma jet was in the x-ray range. Therefore, an x-ray pinhole camera will be built for taking the images of the plasma jets in the near future.

doi:10.6844/NCKU202000512

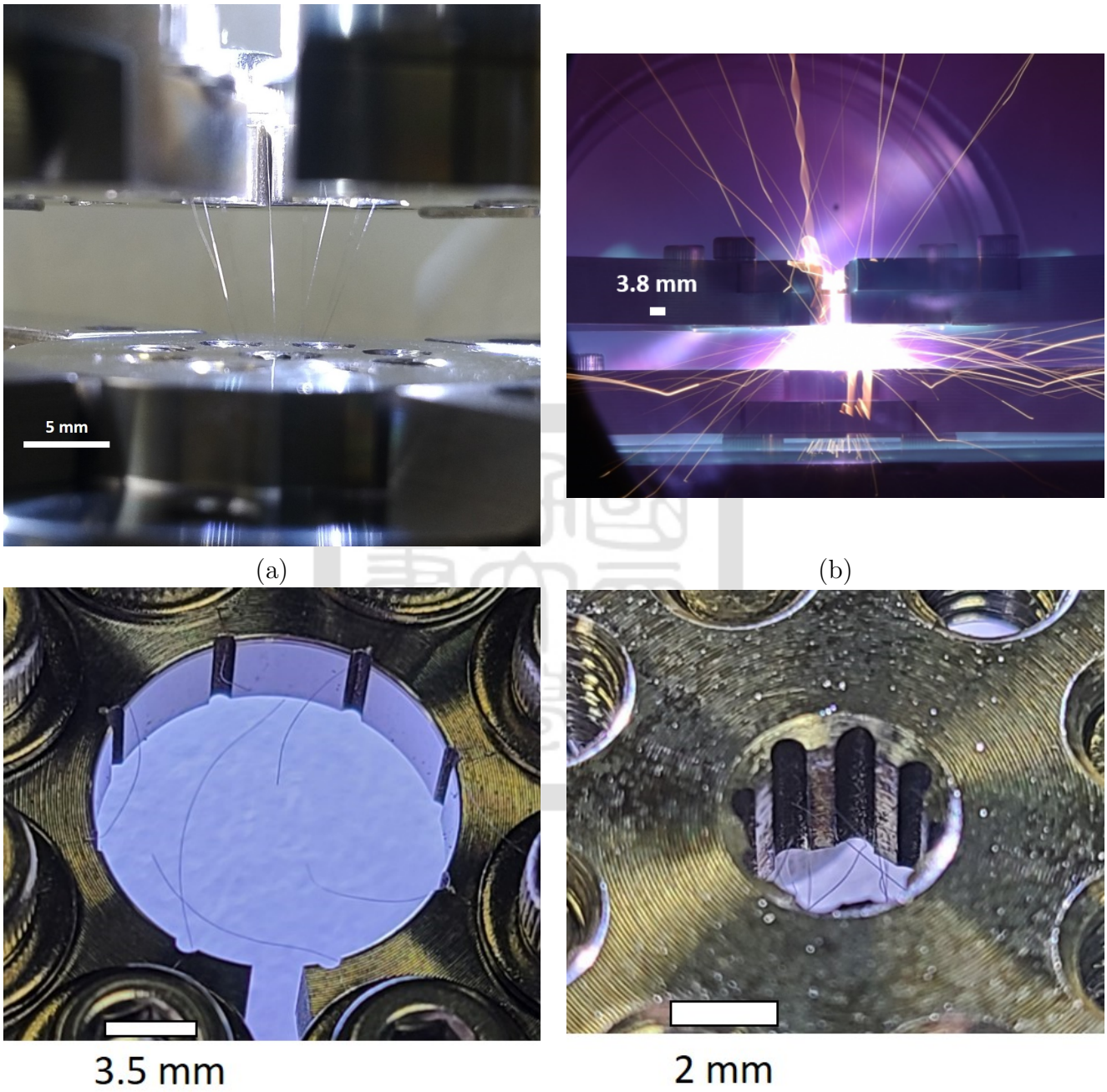

(a) (b)

(c) (d)

Figure 78: A discharging test of the conical-wire array.

doi:10.6844/NCKU202000512

6 Future work

The following are the list of future works:

1. The original design of the conical-wire array had an disadvantage while connecting wires. We needed to connect the wires in the vacuum chamber where the working space is limited. A new design will be needed. We will connect the wires to a wire disk outside of the vacuum chamber. A spacer will be used to hold wires. After installing the wire disk to the coaxial transmission line in the vacuum chamber, the spacer will be removed.

2. The original Rogowski coil we built was too big to put into the coaxial transmission line in the vacuum chamber. In figure 79, the red dots show the original location of the Rogowski coil for discharging test and the green dots show the future location of the Rogowski coil. The first Rogowski coil was built two years ago and the size couldn't fit into the coaxial transmission line at that time. After the first Rogowski coil was broken, we hadn't finished the test of the Rogowski coil and decided to make a same one to complete the test. Therefore, the size of the second Rogowski coil was unable to fit into the system. With the experience of building the Rogowski coil, a final one that can fit into the system will be built

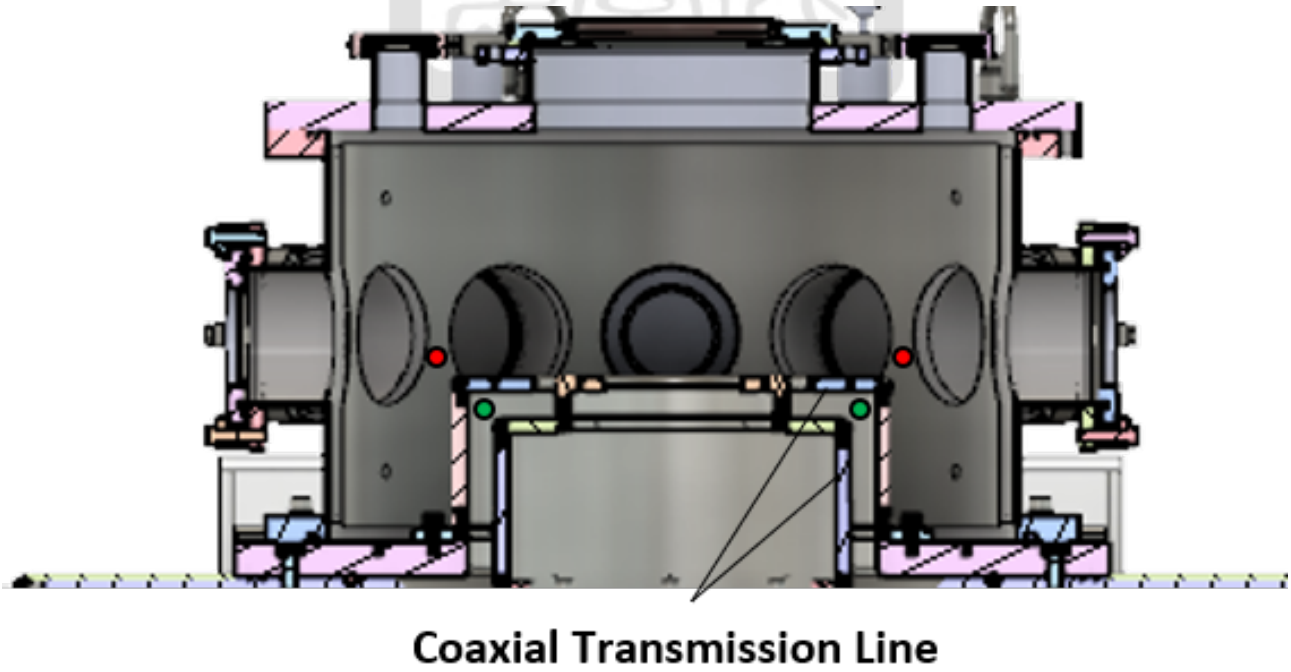

Figure 79: The original location and the future location of the Rogowski coil.

doi:10.6844/NCKU202000512

3. The last step of the x-ray pinhole camera is to put all components together. For the camera, we have the design and it's under fabrication. For the controller, all components in the x-ray pinhole camera controller was built. To preventing EMP noise going back to the power grid of the building, a bus of batteries for providing power of all components is needed. The ground of all components except the high voltage part is the metal case. The communication between the computer and DAQ need to be fixed. Another option is to use the 100 ms timer to postpone the communication problem. A high voltage test will be needed before it's ready to be used.

doi:10.6844/NCKU202000512

7 Summary

The goal of this project is to generate a plasma jet inside a vacuum chamber and forms a bow shock around an object. To generate the plasma jet, we use a pulsed-power system as the electric energy provider and the conical wire array to form plasma jets. To observe the plasma jet, we use a regular camera and an x-ray pinhole camera to take the image. In this thesis, the following work is finished and the corresponding results are shown:

1. The pulsed-power system was built. The peak current output of this system was 110 ± 20 kA with a rise time of 1.5 ± 0.1 μs.

2. The conical-wire array was designed and built. The result was shown in figure 78.

3. Three diagnostics was built. They were the Rogowski coil, the sychronized regular camera, and the x-ray pinhole camera. The Rogowski coil measured the current of the pulsed-power system. The result was shown in section 4.1.7. The regular camera was for taking images of plasma jets. The controller of the x-ray pinhole camera was built. They were shown in figure 67.

4. An image of the plasma jet was taken. Plasma jets were generated and images were taken by the regular camera.

The system parameters of the pulsed-power system is shown in Table 8. Some of the data is from the former student Ming-Cheng Jheng[4].

Table 8: The system parameters of the pulsed-power system.

Item	Value	Item	Value
Number of Capacitor	20	Charging Voltage	20 kV
Total Capacitance	5 μF	Total Energy	1 kJ
Peak Current	110 ± 20 kA	Inductance	150 ± 50 nH
Current Rising Time	1.5 ± 0.1 μs	Inductive Reactance	170 ± 30 mΩ
Current Starting Time	160 ± 50 ns	Delay Time of Pickup Coil	13.4 ± 0.1 ns

The parameters of the discharge of a conical-wire array using a regular camera is shown in Table 9.

doi:10.6844/NCKU202000512

Table 9: The parameters of the discharge of conical-wire array using a regular camera.

Item	Value	Item	Value
Wire Meterial	Tungsten	Diameter of the Bottom Wire Disk	4 mm
Wire Width	20 μm	Diameter of the Top Wire Disk	14 mm
Voltage between wires	20 kV	Distance Between Top and Bottom Disk	10 mm
Camera Aperture	f/22	Camera Exposure Time	30 s

The parameter of the Rogowski coil with an integrator is shown in Table 10.

Table 10: The parameter of the Rogowski coil.

Item	Value
Radius of the Rogowski coil	15 cm
Resistance of the RC integrator	5 kΩ
Capacitance of the RC integrator	48 nF
Ratio of the Rogowski Coil with the Integrator	$(2.071 \pm 0.005) \times 10^4$ s/H
Radius of the Currved Solenoid	2.2 mm
Turns of the Currved Solenoid	50
Time Constant of the RC integrator	0.24 s

The parameter of the x-ray pinhole camera controller is shown in Table 11.

Table 11: The parameter of the x-ray pinhole camera controller.

Item	Value	Item	Value
Battery	24 V	The Rising Delay Time at 0.6 Times of Maximum	0.34 μs
Input Signal	TTL signal	The Rising Delay Time at 0.9 Times of Maximum	0.47 μs
Pulse Voltage	1 kV	The Falling Delay Time	0.41 μs
FWHM	0.96 μs		

doi:10.6844/NCKU202000512

References

[1] SV Lebedev, JP Chittenden, FN Beg, SN Bland, A Ciardi, D Ampleford, S Hughes, MG Haines, A Frank, EG Blackman, et al. Laboratory astrophysics and collimated stellar outflows: The production of radiatively cooled hypersonic plasma jets. *The Astrophysical Journal*, 564(1):113, 2002.

[2] John R Spreiter, Audrey L Summers, and Arthur W Rizzi. Solar wind flow past nonmagnetic planets—venus and mars. *Planetary and Space Science*, 18(9):1281–1299, 1970.

[3] Christopher T. Russell Margaret G. Kivelson, editor. *Introduction to space physics*. Cambridge university press, 1995.

[4] Ming-Cheng Jheng. Development of a 400 mw pulsed-power system. Master's thesis, National Cheng Kung University Institute of Space and Plasma Sciences, 2019.

[5] Sheng-Hua Yang. Developments of high voltage switches. Master's thesis, National Cheng Kung University Institute of Space and Plasma Sciences, 2018.

[6] https://en.wikipedia.org/wiki/paschen%27s_law.

[7] I-Lin Yeh. Theoretical study of the solar wind interacting with an unmagnetized planet in space and in laboratory. Master's thesis, National Cheng Kung University Institute of Space and Plasma Sciences, 2019.

[8] Gregory G Howes. Laboratory space physics: Investigating the physics of space plasmas in the laboratory. *Physics of Plasmas*, 25(5):055501, 2018.

[9] D Ryutov, RP Drake, J Kane, E Liang, BA Remington, and WM Wood-Vasey. Similarity criteria for the laboratory simulation of supernova hydrodynamics. *The Astrophysical Journal*, 518(2):821, 1999.

[10] DD Ryutov, RP Drake, and BA Remington. Criteria for scaled laboratory simulations of astrophysical mhd phenomena. *The Astrophysical Journal Supplement Series*, 127(2):465, 2000.

doi:10.6844/NCKU202000512

[11] Benjamin Edward Stanley Hall, Mark Lester, Beatriz Sánchez-Cano, Jonathan D Nichols, David J Andrews, Niklas JT Edberg, Hermann J Opgenoorth, Markus Fränz, M Holmström, Robin Ramstad, et al. Annual variations in the martian bow shock location as observed by the mars express mission. *Journal of Geophysical Research: Space Physics*, 121(11):11–474, 2016.

[12] JA Slavin, RE Holzer, JR Spreiter, SS Stahara, and DS Chaussee. Solar wind flow about the terrestrial planets: 2. comparison with gas dynamic theory and implications for solar-planetary interactions. *Journal of Geophysical Research: Space Physics*, 88(A1):19–35, 1983.

[13] Mei-Feng Huang. Rust remover using small pulsed-power system. Master's thesis, National Cheng Kung University Institute of Space and Plasma Sciences, 2017.

[14] https://www.graser.com.tw/product_or_capture_cis.htm.

[15] ftp://ftp.grnet.gr/pub/pc/pspice/student_version_9_1/pspcref.pdf.

[16] https://en.wikipedia.org/wiki/rogowski_coil.

[17] https://en.wikipedia.org/wiki/inductor.

[18] JOSEPH LADISLAS WIZA. Microchannel plate detectors. *NUCLEAR INSTRUMENTS AND METHODS*, 162:587–601, 1979.

[19] https://baspik.com/eng/.

[20] https://pdf1.alldatasheet.com/datasheet-pdf/view/970276/rohm/sct3160kl.html.

[21] https://pdf1.alldatasheet.com/datasheet-pdf/view/837744/ixys/ixxk110n65b4h1.html.

[22] www.meanwellusa.com/productpdf.aspx?i=92#1.

[23] pdf1.alldatasheet.com/datasheet-pdf/view/509579/diodes/fod3184.html.

[24] https://pdf1.alldatasheet.com/datasheet-pdf/view/539950/ti1/sn74hc04apwr.html.

[25] https://docs.rs-online.com/b50e/0900766b813dfad9.pdf.

[26] ftp://chieh@140.116.16.6/shares/chieh/mcp%20labview/controller.vi.

doi:10.6844/NCKU202000512

[27] M. K. Matzen D. D. Ryutov, M. S. Derzon. The physics of fast z pinches. *Reviews of Modern Physics*, 72(1), January 2000.

doi:10.6844/NCKU202000512

A Appendix

A.1 The breakdown voltage

When the voltage between two electrodes with a gap between them exceeds a threshold, high-conductive channels are formed. The phenomenon is called breakdown. The threshold is called the breakdown voltage. For different gap distance, gas, and gas pressure in between the electrodes, the breakdown voltage can be obtained from the Paschen's curve as shown in figure 80. The x axis is the gas pressure P between the electrodes times the distance d between two electrodes. The y axis is the breakdown voltage V_B of the electrodes. Different gas has different Paschen's curve. Paschen's curve is used to determine the gap distance of the spark-gap switch and the rail-gap switch. Since the switches are not pressurized, the breakdown voltage is set by the distance between two electrodes.

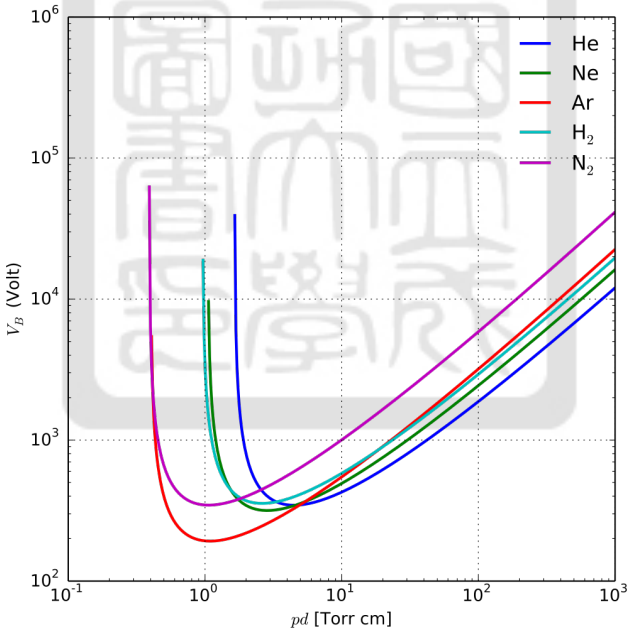

Figure 80: Paschen's law gives the breakdown voltage.[6]

doi:10.6844/NCKU202000512

A.2 The data of discharge tests

Table 12: Rail-gap switch breakdown voltage.

breakdown kV	cap kV	cap mA	breakdown kV	cap kV	cap mA
40.0	40.0	100	42.1	46.3	100
34.0	40.0	100	39.8	47.2	150
40.5	40.0	100	38.8	47.2	150
40.4	40.0	100	39.4	47.2	150
40.5	40.0	100	39.6	47.2	150
42.9	45.2	100	39.4	47.2	150
41.7	45.2	100	39.5	47.2	150
43.0	45.2	100	39.9	47.2	150
43.2	45.2	100	42.7	47.2	150
43.0	45.2	100	44.0	47.2	150
41.9	45.2	100	43.4	47.2	150
43.1	45.2	100	44.2	47.2	150
42.1	45.2	100	51.2	51.3	150
42.5	45.2	100	50.2	51.3	150
41.2	45.2	100	46.8	51.3	150
42.1	45.2	100	45.2	51.3	150
41.3	46.3	100	43.0	51.3	150
41.2	46.3	100	42.8	51.3	150

Table 13: Pickup coil signal relative to Marx generator signal.

No.	Time different (μs)	No.	Time different (μs)
30	13.2895	38	13.375
31	13.4143	39	13.3444
32	13.3143	40	13.4222
33	13.5682	41	13.5476
34	13.2429	42	13.219
35	13.7143	43	13.3
36	17.4643	44	13.5556
37	13.5455	avg	13.41805714
		std	0.147044759

doi:10.6844/NCKU202000512

Table 14: Time of the discharge current at north wing before polishing.

serial	start time	peak time	time diff	serial	start time	peak time	time diff
0	8.18E-09	1.07E-06	1.06E-06	16	8.31E-09	1.36E-06	1.36E-06
1	7.80E-09	1.03E-06	1.02E-06	17	2.80E-09	1.26E-06	1.26E-06
2	3.46E-09	1.08E-06	1.08E-06	18	6.91E-09	1.17E-06	1.16E-06
3	4.33E-09	1.24E-06	1.24E-06	19	1.67E-09	1.15E-06	1.15E-06
4	3.00E-09	1.02E-06	1.01E-06	20	3.30E-09	1.29E-06	1.29E-06
5	2.55E-09	1.30E-06	1.30E-06	21	6.92E-09	1.17E-06	1.16E-06
6	1.25E-09	1.07E-06	1.36E-06	22	2.13E-09	8.38E-07	8.35E-07
7	7.69E-09	1.02E-06	1.01E-06	23	5.67E-09	1.18E-06	1.18E-06
8	4.00E-09	9.18E-07	9.14E-07	24	3.00E-09	1.11E-06	1.10E-06
9	4.29E-09	1.02E-06	1.01E-06	25	6.00E-09	1.31E-06	1.30E-06
10	3.00E-09	1.14E-06	1.14E-06	26	8.57E-10	1.06E-06	1.05E-06
11	6.00E-09	1.18E-06	1.18E-06	27	5.56E-09	1.03E-06	1.03E-06
12	7.57E-09	1.07E-06	1.07E-06	28	1.43E-09	8.41E-07	8.40E-07
13	6.44E-09	1.17E-06	1.16E-06	29	1.03E-08	8.98E-07	8.87E-07
14	4.50E-09	1.30E-06	1.30E-06	avg	4.86E-09	1.11728E-06	1.21E-06
15	7.00E-09	1.22E-06	1.21E-06	std	2.49499E-09	1.38707E-07	5.65E-07

Table 15: The delay time and frequency of the discharging current after polishing.

#	Delay time of peak current	Frequency of current
1	3.11E-07	3.76E+05
2	2.04E-07	3.76E+05
3	2.10E-07	3.75E+05
4	1.74E-07	3.78E+05
5	1.40E-07	3.77E+05
6	2.81E-07	3.78E+05
7	1.92E-07	3.79E+05
8	2.57E-07	3.74E+05
9	2.92E-07	3.76E+05
10	3.52E-07	3.81E+05
11	2.26E-07	3.78E+05
12	1.67E-07	3.80E+05
13	2.77E-07	3.75E+05
avg	2.37E-07	3.77E+05
std	6.32E-08	1.93E+03

doi:10.6844/NCKU202000512

Table 16: Time of the discharge current at north wing before polishing.

serial	start time	peak time	time diff	peak curr
0	1.49E-08	1.03E-06	1.02E-06	-21790.81417
1	6.25E-10	1.10E-06	1.10E-06	-22064.99761
2	8.75E-09	1.02E-06	1.01E-06	-21557.46546
3	2.60E-08	9.49E-07	9.23E-07	-21610.78182
4	1.67E-10	9.44E-07	9.43E-07	-21742.07584
5	2.63E-08	9.10E-07	8.83E-07	-21970.60977
6	2.64E-08	9.00E-07	8.74E-07	-21709.26651
7	-2.00E-09	9.77E-07	9.79E-07	-22414.92354
8	2.53E-08	9.55E-07	9.29E-07	-21370.3949
9	1.40E-08	9.88E-07	9.74E-07	-20433.52297
10	5.46E-17	9.86E-07	9.86E-07	-22690.86362
11	-1.60E-09	1.05E-06	1.05E-06	-22238.18704
12	5.67E-09	9.35E-07	9.29E-07	-22421.34148
13	2.67E-08	9.14E-07	8.88E-07	-21879.51467
14	7.00E-10	9.99E-07	9.99E-07	-22062.35461
avg	1.26E-08	9.78E-07	9.65E-07	-21863.8076
std	1.25E-08	6.68E-08	6.33E-08	535.9486627

Table 17: Time of the discharge current at south wing after polishing.

serial	start time	peak time	time diff	peak curr
1	-9.75E-09	8.98E-07	9.07E-07	-21187.22347
2	-1.89E-09	8.95E-07	8.97E-07	-21677.9293
3	-9.63E-10	9.14E-07	9.15E-07	-15911.07731
4	-1.65E-09	8.90E-07	8.92E-07	-21018.91109
5	-1.00E-09	9.00E-07	9.01E-07	-22183.37105
6	-1.00E-09	9.12E-07	9.13E-07	-20479.18861
7	-9.80E-09	9.79E-07	9.89E-07	-21260.16492
8	-1.77E-09	9.40E-07	9.42E-07	-21337.57809
9	-8.10E-10	9.34E-07	9.35E-07	-21287.36448
10	-7.65E-10	9.30E-07	9.30E-07	-20917.15888
11	-1.00E-09	9.87E-07	9.88E-07	-21473.18927
12	-1.41E-09	9.04E-07	9.05E-07	-21349.25118
13	-1.53E-09	9.04E-07	9.06E-07	-21214.7882
14	-9.01E-09	9.15E-07	9.24E-07	-20910.06906
avg	-3.02E-09	9.21E-07	9.21E-07	-20871.94749
std	3.54E-09	2.99E-08	3.23E-08	1480.783878

doi:10.6844/NCKU202000512

Table 18: The results of the 1-1 discharging test.

#	Peak current	Peak current time	peak current occurred
0	-3.72E+04	1.07E-06	1.69E-07
1	-3.42E+04	1.03E-06	7.65E-08
2	-3.83E+04	1.02E-06	1.60E-07
3	-4.07E+04	9.53E-07	1.71E-07
4	-4.10E+04	9.81E-07	2.05E-07
5	-4.17E+04	9.51E-07	1.90E-07
6	-4.13E+04	8.68E-07	8.71E-08
7	-4.09E+04	1.00E-06	2.21E-07
8	-4.05E+04	9.65E-07	1.79E-07
9	-4.10E+04	9.05E-07	1.17E-07
10	-4.25E+04	9.44E-07	1.81E-07
11	-4.22E+04	9.52E-07	1.94E-07
12	-3.88E+04	1.02E-06	1.68E-07
13	-3.97E+04	9.86E-07	1.96E-07
14	-4.20E+04	9.15E-07	1.28E-07
15	-4.13E+04	9.08E-07	1.18E-07
16	-4.22E+04	9.07E-07	1.30E-07
17	-4.16E+04	9.34E-07	1.67E-07
18	-4.24E+04	9.08E-07	1.31E-07
19	-4.21E+04	9.33E-07	1.59E-07
20	-4.22E+04	9.56E-07	1.85E-07
21	-4.19E+04	9.54E-07	1.94E-07
22	-4.19E+04	8.79E-07	9.81E-08
23	-4.20E+04	9.95E-07	2.26E-07
24	-4.23E+04	9.61E-07	1.91E-07
25	-4.14E+04	9.25E-07	1.43E-07
26	-4.23E+04	9.34E-07	1.65E-07
27	-4.13E+04	9.23E-07	1.32E-07
28	-4.25E+04	9.05E-07	1.24E-07
29	-4.23E+04	9.11E-07	1.29E-07
avg	-4.11E+04	9.50E-07	1.58E-07
std	1.82E+03	4.69E-08	3.84E-08

doi:10.6844/NCKU202000512

Table 19: The results of the 3-3 discharging test.

#	Peak current	Peak current time	peak current occurred
0	-3.52E+04	1.17E-06	1.14E-07
1	-3.70E+04	1.16E-06	1.12E-07
2	-3.87E+04	1.15E-06	1.31E-07
3	-3.75E+04	1.15E-06	1.25E-07
4	-3.67E+04	1.17E-06	1.34E-07
5	-3.71E+04	1.20E-06	1.37E-07
6	-3.71E+04	1.15E-06	1.26E-07
7	-3.72E+04	1.17E-06	1.24E-07
8	-3.69E+04	1.18E-06	1.39E-07
9	-3.68E+04	1.17E-06	1.13E-07
10	-3.70E+04	1.20E-06	1.37E-07
11	-3.74E+04	1.20E-06	1.56E-07
12	-5.66E+04	1.07E-06	1.30E-07
13	-3.78E+04	1.20E-06	2.24E-07
14	-3.70E+04	1.17E-06	1.19E-07
15	-3.78E+04	1.17E-06	1.38E-07
16	-3.74E+04	1.17E-06	1.39E-07
17	-3.71E+04	1.16E-06	1.19E-07
18	-3.75E+04	1.17E-06	1.37E-07
19	-3.80E+04	1.15E-06	1.25E-07
20	-3.65E+04	1.32E-06	1.93E-07
avg	-3.81E+04	1.17E-06	1.37E-07
std	4.29E+03	4.40E-08	2.64E-08

doi:10.6844/NCKU202000512

Table 20: The discharge tests of the whole system.

Serial	curr max	error	curr time	error	S time	N time	time diff
0	-1.17E+05		1.56E-06		1.15E-07	1.12E-07	2.24E-09
1	-1.11E+05		1.63E-06		1.19E-07	1.10E-07	8.86E-09
2	-9.01E+04		1.67E-06		1.23E-07	1.30E-07	-7.37E-09
3	-1.14E+05		1.58E-06		1.26E-07	1.30E-07	-3.78E-09
4	-1.20E+05		1.57E-06		1.23E-07	1.30E-07	-7.67E-09
5	-1.15E+05		1.58E-06		1.18E-07	1.31E-07	-1.29E-08
6	-1.17E+05		1.59E-06		1.26E-07	1.41E-07	-1.49E-08
7		1.94E+05		6.00E-06	1.02E-07	1.04E-07	-2.07E-09
8	-9.08E+04		1.67E-06		1.21E-07	1.23E-07	-2.35E-09
9		3.32E+05		5.99E-06	1.13E-07	1.10E-07	3.34E-09
10	-7.10E+04		1.74E-06		1.30E-07	1.39E-07	-9.50E-09
11		2.26E+05		6.00E-06	1.18E-07	1.14E-07	4.24E-09
12		4.83E+05		6.00E-06	1.22E-07	1.31E-07	-8.54E-09
13	-1.17E+05		1.63E-06		1.28E-07	1.36E-07	-7.92E-09
14	-1.22E+05		1.59E-06		1.22E-07	1.19E-07	2.61E-09
15		2.88E+05		6.00E-06	1.17E-07	1.27E-07	-9.50E-09
16	-1.19E+05		1.62E-06		1.12E-07	1.18E-07	-6.70E-09
17		1.23E+05		2.28E-06	1.30E-07	1.20E-07	1.04E-08
18	-1.21E+05		1.60E-06		1.62E-07	1.15E-07	4.67E-08
19	-1.18E+05		1.59E-06		1.16E-07	1.17E-07	-1.38E-09
20		2.40E+05		6.00E-06	1.32E-07	1.29E-07	3.78E-09
21		2.51E+05		3.11E-06	1.18E-07	1.84E-07	-6.60E-08
22	-6.80E+04		1.80E-06		1.18E-07	2.13E-07	-9.51E-08
23	-1.19E+05		1.59E-06		1.13E-07	1.19E-07	-6.27E-09
24	-1.23E+05		1.69E-06		1.26E-07	2.12E-07	-8.67E-08
25	-1.23E+05		1.60E-06		1.15E-07	1.24E-07	-8.94E-09
26	-1.09E+05		1.65E-06		1.10E-07	1.32E-07	-2.21E-08
27		2.62E+05		6.00E-06	1.22E-07	1.24E-07	-2.51E-09
28	-7.56E+04		1.71E-06		1.34E-07	1.29E-07	5.29E-09
29		3.94E+05		6.00E-06	1.34E-07	1.21E-07	1.29E-08
avg	-1.08E+05		1.63E-06		1.22E-07	1.32E-07	-9.74E-09
std	1.82E+04		6.40E-08		1.06E-08	2.62E-08	2.79E-08

doi:10.6844/NCKU202000512

Table 21: The discharge tests of the whole system.

S volt	N volt	tmin	rise t	period	period/4
1.42E+04	1.30E+04	1.12E-07	1.45E-06	5.85E-06	1.46E-06
1.42E+04	1.32E+04	1.10E-07	1.52E-06	5.88E-06	1.47E-06
1.41E+04	1.29E+04	1.23E-07	1.55E-06	5.62E-06	1.40E-06
1.40E+04	1.29E+04	1.26E-07	1.45E-06	5.78E-06	1.45E-06
1.40E+04	1.31E+04	1.23E-07	1.45E-06	5.88E-06	1.47E-06
1.41E+04	1.33E+04	1.18E-07	1.46E-06	5.88E-06	1.47E-06
1.39E+04	1.29E+04	1.26E-07	1.46E-06	5.81E-06	1.45E-06
1.42E+04	1.32E+04	1.02E-07			
1.41E+04	1.31E+04	1.21E-07	1.55E-06	5.65E-06	1.41E-06
1.42E+04	1.32E+04	1.10E-07		3.17E-06	7.94E-07
1.42E+04	1.30E+04	1.30E-07	1.61E-06	5.41E-06	1.35E-06
1.41E+04	1.30E+04	1.14E-07			
1.40E+04	1.30E+04	1.22E-07		3.61E-06	9.03E-07
1.41E+04	1.30E+04	1.28E-07	1.50E-06	5.81E-06	1.45E-06
1.41E+04	1.30E+04	1.19E-07	1.47E-06	5.85E-06	1.46E-06
1.41E+04	1.29E+04	1.17E-07		4.12E-06	1.03E-06
1.43E+04	1.33E+04	1.12E-07	1.51E-06	5.92E-06	1.48E-06
1.43E+04	1.33E+04	1.20E-07		3.56E-06	8.90E-07
1.43E+04	1.34E+04	1.15E-07	1.49E-06	5.92E-06	1.48E-06
1.42E+04	1.34E+04	1.16E-07	1.47E-06	5.92E-06	1.48E-06
1.43E+04	1.31E+04	1.29E-07			
1.46E+04	1.31E+04	1.18E-07		5.15E-06	1.29E-06
1.47E+04	1.26E+04	1.18E-07	1.68E-06	5.43E-06	1.36E-06
1.43E+04	1.33E+04	1.13E-07	1.48E-06	5.88E-06	1.47E-06
1.46E+04	1.27E+04	1.26E-07	1.56E-06	5.88E-06	1.47E-06
1.42E+04	1.31E+04	1.15E-07	1.49E-06	5.85E-06	1.46E-06
1.43E+04	1.30E+04	1.10E-07	1.54E-06	5.75E-06	1.44E-06
1.43E+04	1.33E+04	1.22E-07			
1.42E+04	1.31E+04	1.29E-07	1.58E-06	5.52E-06	1.38E-06
1.42E+04	1.29E+04	1.21E-07		2.09E-06	5.23E-07
1.42E+04	1.31E+04	1.19E-07	1.51E-06	5.28E-06	1.32E-06
1.75E+02	1.83E+02	6.75E-09	6.20E-08	1.04E-06	2.60E-07

doi:10.6844/NCKU202000512

A.3 The component drawings of the conical-wire array

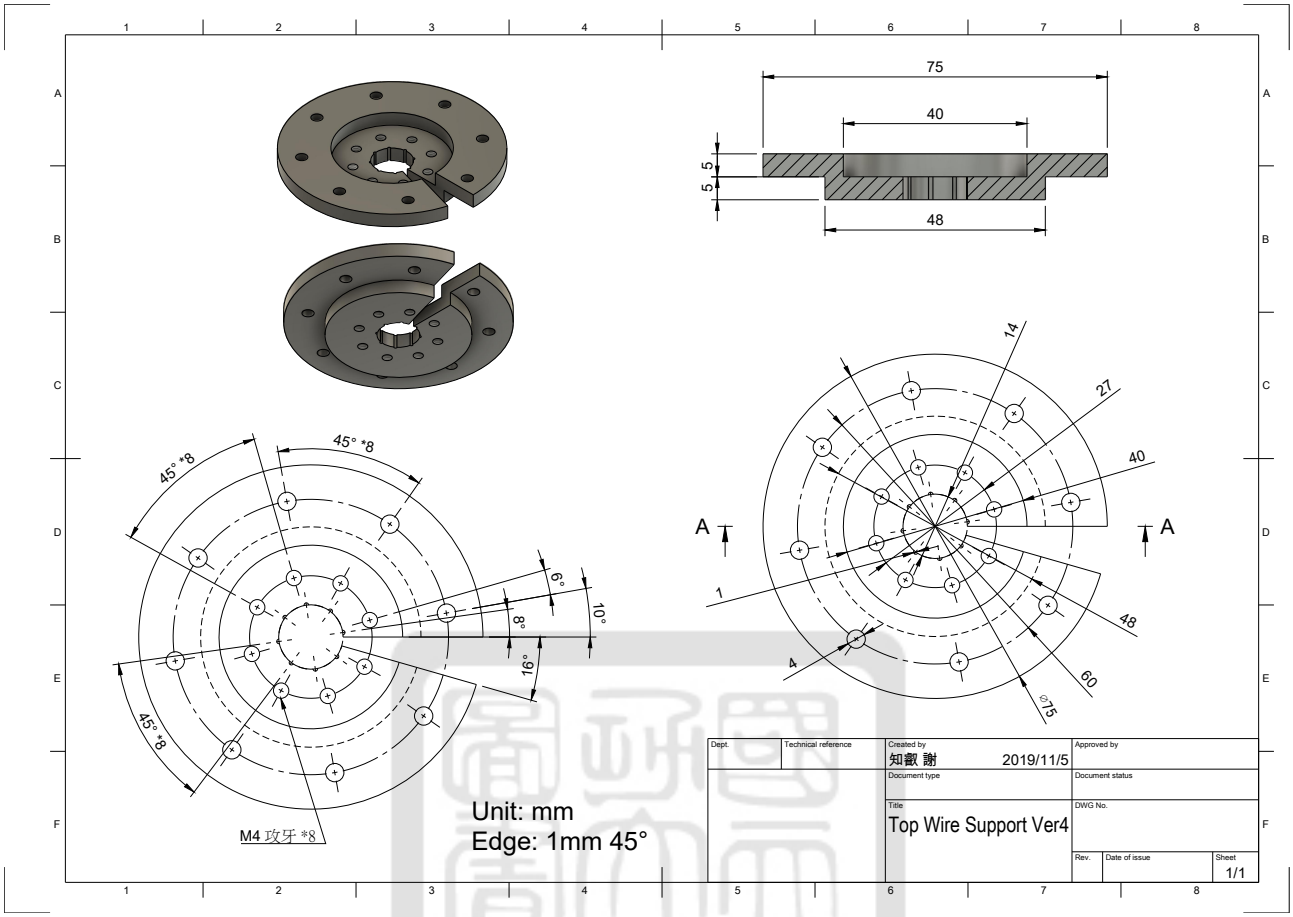

Figure 81: Top wire disk.

doi:10.6844/NCKU202000512

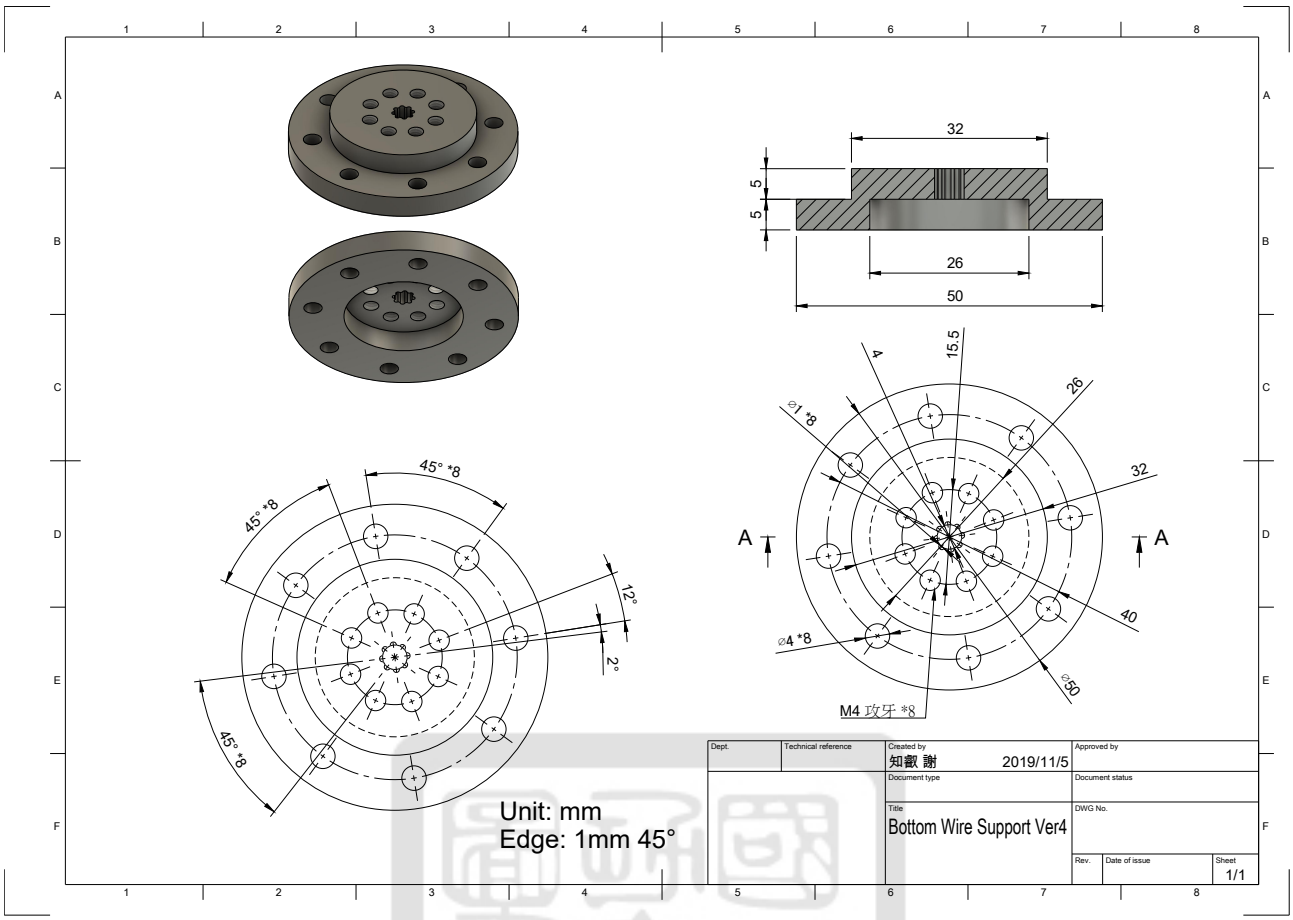

Figure 82: Bottom wire disk.

doi:10.6844/NCKU202000512

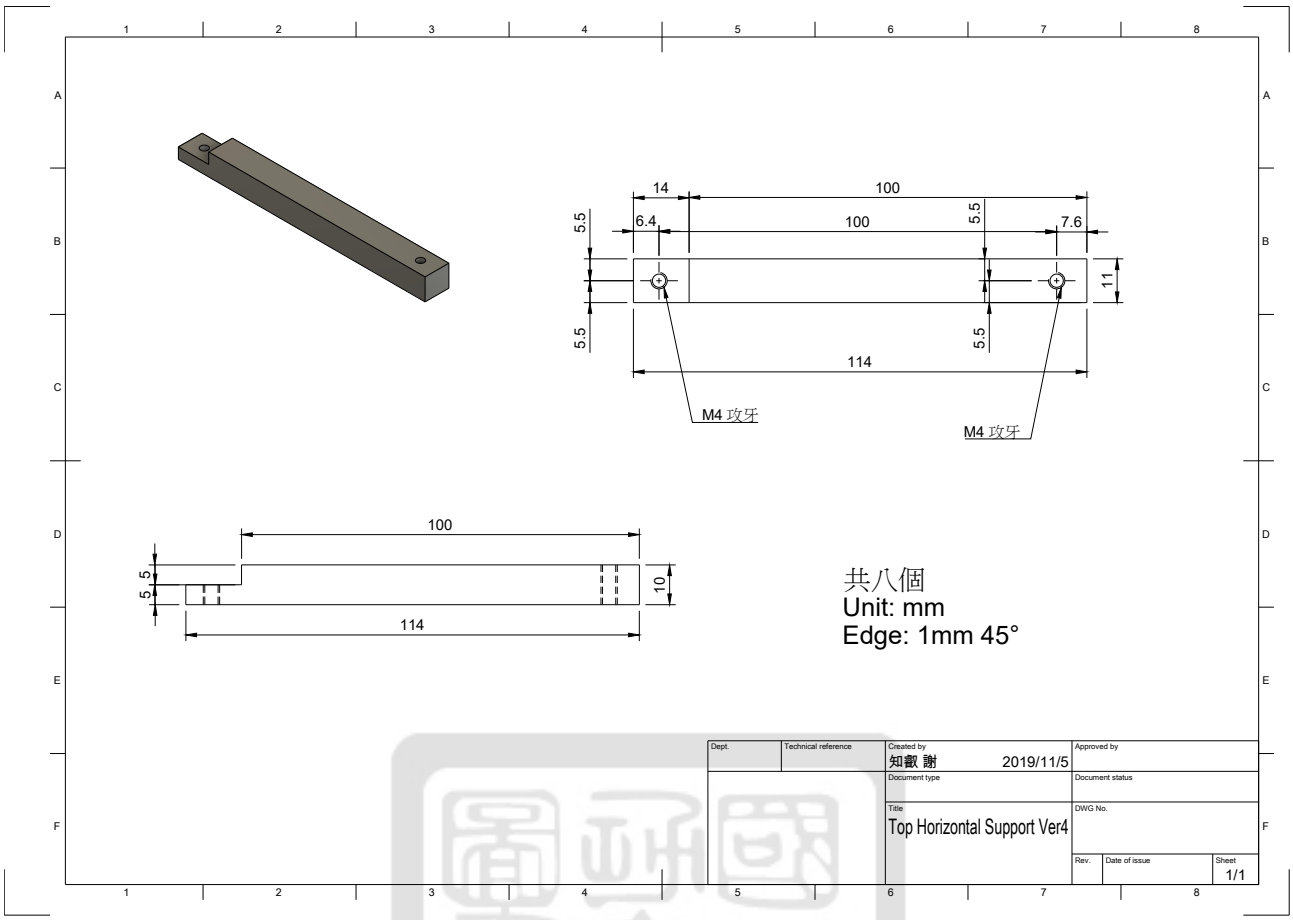

Figure 83: Top support beam.

doi:10.6844/NCKU202000512

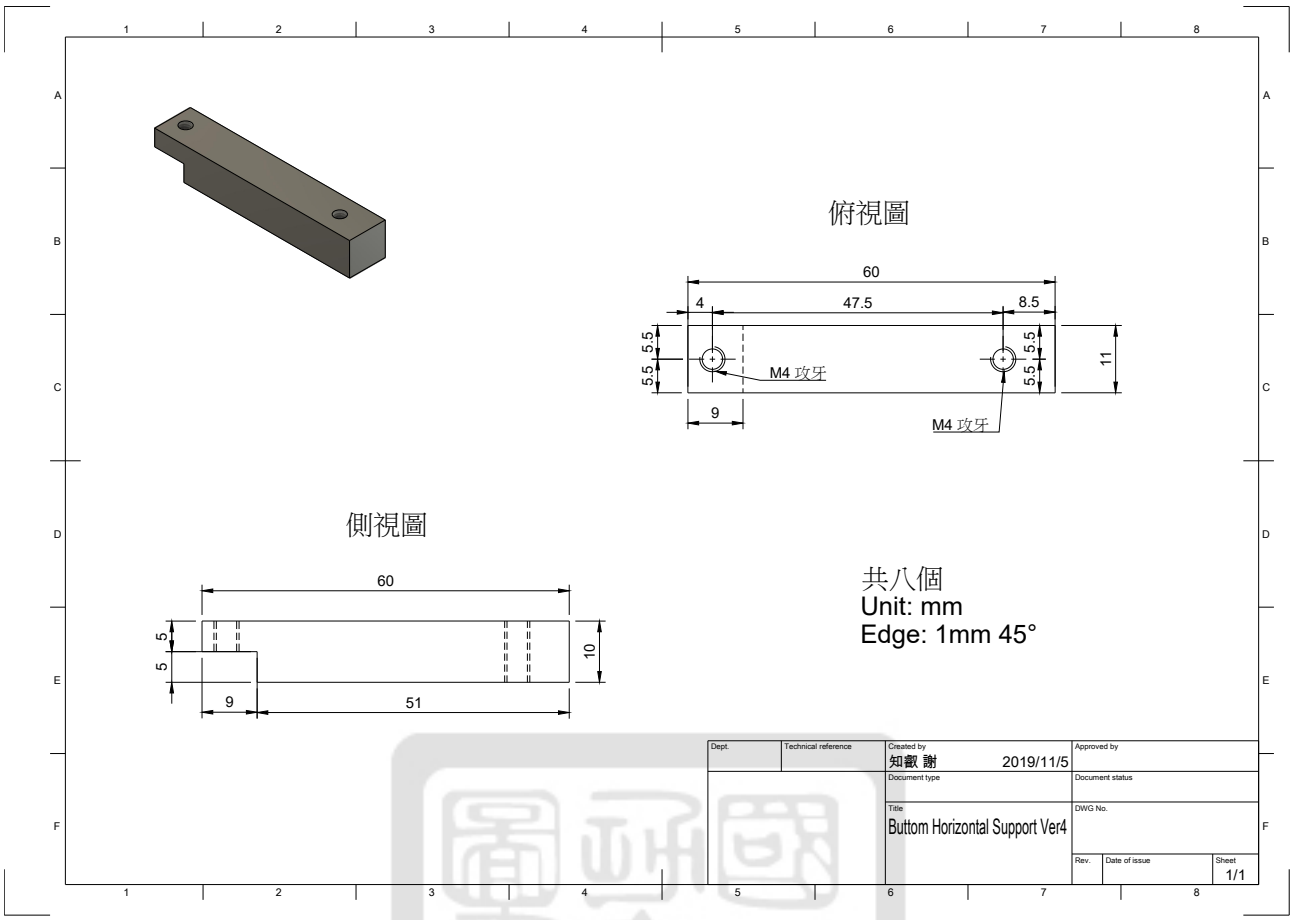

Figure 84: Bottom support beam.

doi:10.6844/NCKU202000512

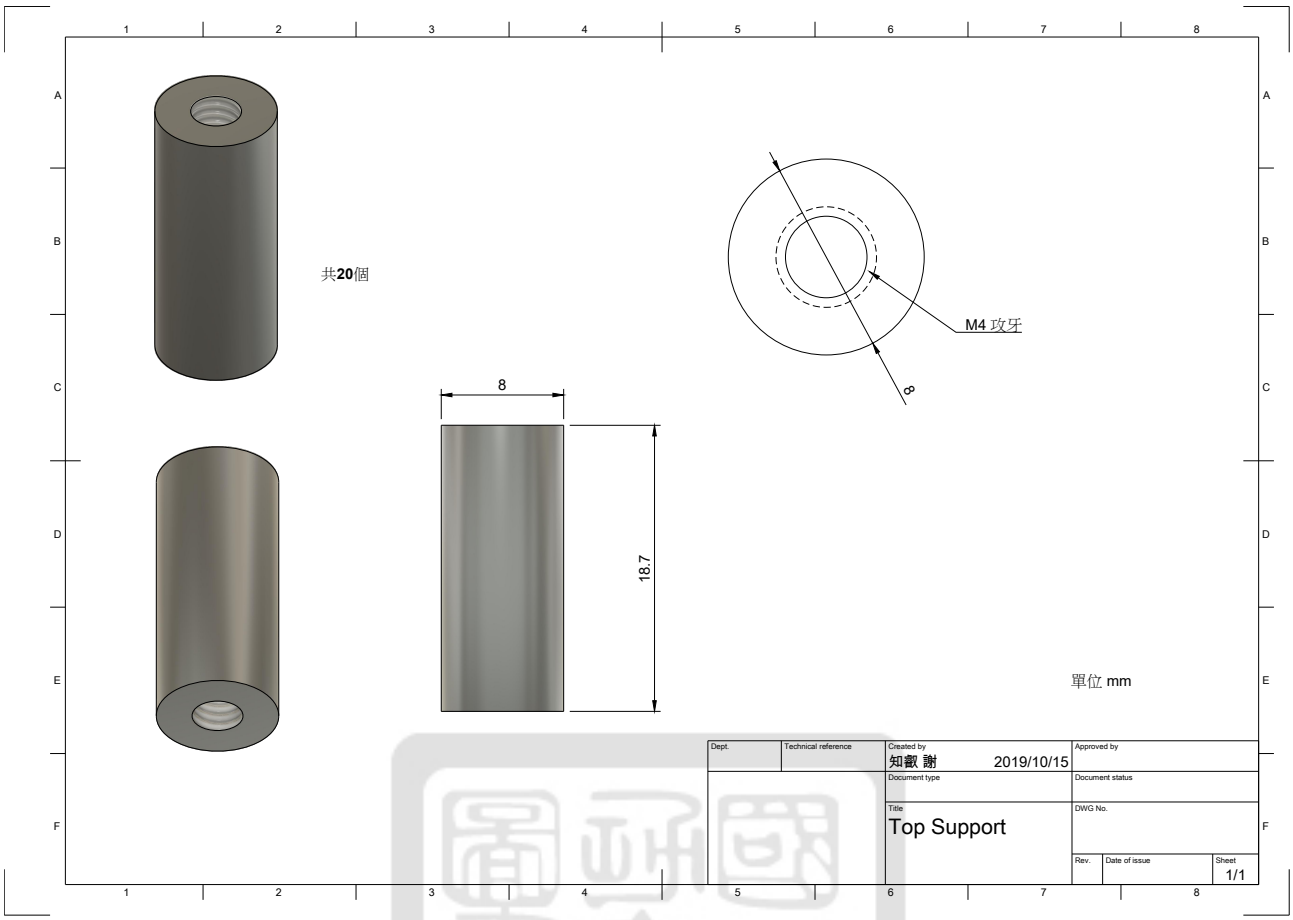

Figure 85: Support column.

A.4 The Rogowski coil

serial	A	lambda	omega	phi
1	97.43427449	-34965.57842	2.37E+06	0.616284493
2	114.8335796	-68948.14304	2.37E+06	0.49459589
3	92.60797318	-27727.59099	2.35E+06	0.070283323
4	93.48652867	-27329.64211	2.37E+06	0.648508001
5	90.0354708	-19444.22889	2.39E+06	-0.150272717
6	81.04026566	-1138.954631	2.38E+06	-0.50890895
7	94.67997563	-28146.9559	2.37E+06	0.647831245
8	109.6169687	-57652.47201	2.37E+06	0.879994992
9	98.81107781	-38181.89239	2.38E+06	0.652707211
10	107.288627	-52203.44519	2.37E+06	0.330084052
11	105.8301861	-47784.75633	2.39E+06	0.211670844
12	110.5603001	-60700.26946	2.36E+06	0.514194396
13	107.7136121	-54999.53885	2.35E+06	0.299452921
14	90.03657852	-19307.78326	2.38E+06	-0.145578662
avg	99.56967274	-38466.51796	2371824.882	0.325774789
std	9.842854421	19257.12777	10445.89384	0.39172396

Table 22: The parameters from Eq.36.

doi:10.6844/NCKU202000512

Table 23: The mutual inductance of Rogowski coil.

#	Mutual Inductance
0	-1.96E-09
1	-1.92E-09
2	-1.96E-09
3	-1.89E-09
4	-1.90E-09
5	-1.87E-09
6	-1.85E-09
7	-1.89E-09
8	-1.95E-09
9	-1.91E-09
10	-1.94E-09
11	-1.92E-09
12	-1.95E-09
13	-1.94E-09
14	-1.87E-09

serial	A	lambda	omega	phi
15	2.41E+04	-6.34E+04	2.36E+06	5.73E-01
16	2.38E+04	-5.59E+04	2.37E+06	4.64E-01
17	2.41E+04	-6.40E+04	2.37E+06	5.39E-01
18	2.34E+04	-6.46E+04	2.37E+06	6.10E-01
19	2.38E+04	-6.45E+04	2.36E+06	6.24E-01
20	2.39E+04	-6.10E+04	2.36E+06	5.19E-01
21	2.42E+04	-6.42E+04	2.36E+06	6.15E-01
22	2.34E+04	-6.09E+04	2.38E+06	8.58E-01
23	2.41E+04	-6.29E+04	2.37E+06	5.97E-01
24	2.40E+04	-6.39E+04	2.36E+06	6.56E-01
25	2.43E+04	-5.72E+04	2.38E+06	5.01E-01
26	2.36E+04	-6.13E+04	2.35E+06	7.01E-01
27	2.43E+04	-6.27E+04	2.39E+06	7.07E-01
28	2.38E+04	-6.15E+04	2.38E+06	8.53E-01
29	2.40E+04	-6.27E+04	2.39E+06	8.09E-01
avg	2.39E+04	-6.20E+04	2.37E+06	6.42E-01
std	2.94E+02	2.56E+03	1.12E+04	1.23E-01

Table 24: The parameters of I_{in} when calibrating the Rogowski coil with the integrator.

doi:10.6844/NCKU202000512

Table 25: The ratio of the Rogowski coil with the integrator and the delay time.

serial	ratio	shift
15	-0.000474743	-8.98E-08
16	-0.000475894	-8.59E-08
17	-0.000473727	-8.59E-08
18	-0.000409347	-1.17E-07
19	-0.000474509	-9.25E-08
20	-0.000474363	-8.58E-08
21	-0.000477656	-9.21E-08
22	-0.000482137	-9.40E-08
23	-0.000477717	-8.93E-08
24	-0.000480396	-9.32E-08
25	-0.000478292	-8.44E-08
26	-0.000477487	-8.92E-08
27	-0.000482899	-9.17E-08
28	-0.000481939	-9.22E-08
29	-0.000480425	-9.07E-08
avg	-0.000473435	-9.16E-08
std	1.80E-05	7.58E-09

A.5 The pinhole camera controller and the MCP driver

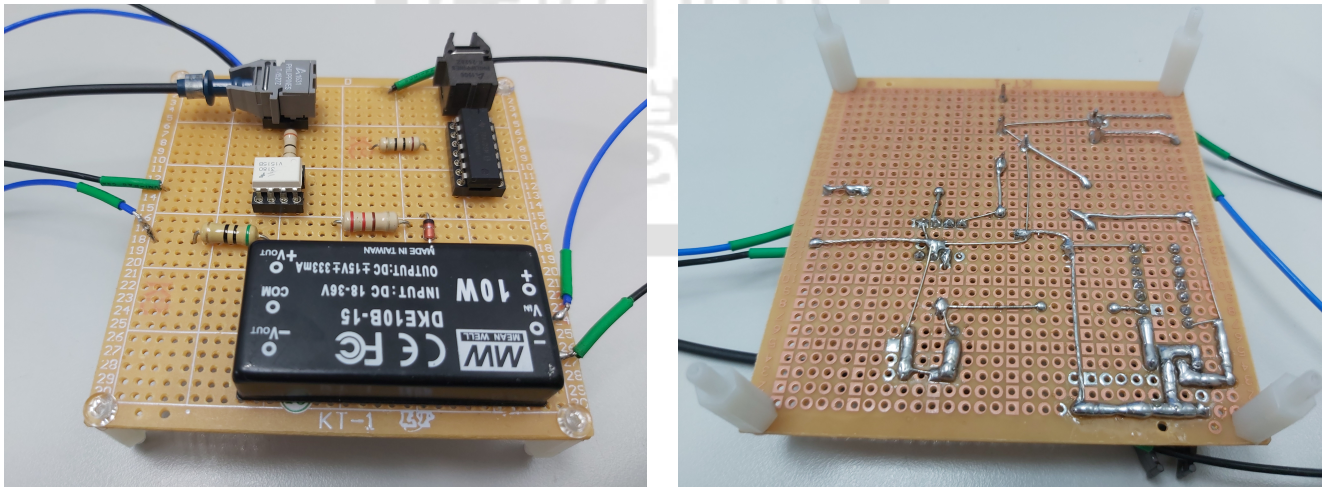

(a) (b)

Figure 86: The low voltage part of MOSFET driver. (a) Front view. (b) Back view.

The blue arrows show the component pointed by the arrow is powered by the component of the upper level. The red arrows show the signal transmitted direction. The DC-DC converter has the input of 18 to 36 V and the output of 15 V. The 5 V Zener diode with a 200 Ω resistor converts the 15 V supply voltage to 5 V supply voltage for the optical receiver and the NOT gate. The other resistors is important for controlling the current through the components.

doi:10.6844/NCKU202000512

Table 26: The parameters of the square pulse from the MCP driver using IGBTs.

Volt	delay 0.6x	delay 0.9x	final delay	highest voltage	falling speed	FWHM
100	1.90626894	5.48440632	0.529226327	67.441283	127.4337264	8.815333333
150	1.423563322	4.55491702	0.554368643	110.5620882	199.4378463	9.184263937
200	1.26313654	3.225354613	0.629064231	153.8399995	244.5537225	9.282120111
250	1.258002171	2.79996609	0.660394717	192.7999994	291.9466108	9.270056077
300	1.355638589	2.62884777	0.644464091	232.340137	360.5168081	9.161940394
350	1.493125278	2.598731907	0.649914314	268.6399824	413.3467696	9.022200288
400	1.56560009	2.577750841	0.675323836	305.295046	452.0720725	8.94975476
450	1.599501018	2.579896299	0.694370211	337.77	486.4407987	8.922675357
500	1.623989751	2.524605245	0.729272189	376.660137	516.4877292	8.91055601
550	1.637668218	2.546205896	0.821400125	409.1318519	498.0908077	8.899822499
600	1.644988307	2.46577384	0.753676104	444.48	589.7493598	8.904338021

Table 27: The parameters of the square pulse from the MCP driver using MOSFETs.

Volt	delay 0.6x	delay 0.9x	final delay	highest voltage	FWHM
100	0.382984334	0.821953163	0.230847793	67.83999989	0.848044837
150	0.329097824	0.532431157	0.230445019	103.679985	0.899994685
200	0.307035556	0.556999968	0.287366849	144.330264	0.913079598
250	0.303681952	0.481451185	0.290491119	184.8	0.920266673
300	0.304405298	0.459911854	0.303376468	228.660528	0.925019338
350	0.306523481	0.466538717	0.300577333	263.3599999	0.927765332
400	0.308398384	0.450680588	0.311290036	303.522566	0.931448586
450	0.310533032	0.451039099	0.313841233	341.28	0.930990543
500	0.313795887	0.448281472	0.345475672	390.1	0.936671856
550	0.316063926	0.450365469	0.334812984	425.5999998	0.938195206
600	0.318281191	0.453019648	0.354940908	461.5999994	0.940122353
650	0.322004473	0.455375322	0.357654719	516.650264	0.945290279
700	0.321823543	0.453075603	0.375251815	524.830092	0.943730564
750	0.327441351	0.454188454	0.37682197	587.5199942	0.95293484
800	0.330770115	0.458002348	0.387539214	635.0399989	0.953438798
850	0.33375193	0.460368082	0.393786994	684.32	0.957793748
900	0.335861165	0.46209335	0.399877123	706.882566	0.959025132
950	0.339726475	0.464062672	0.40401922	755.050264	0.959562826
1000	0.342371439	0.466390501	0.411031554	782.570264	0.963138348

doi:10.6844/NCKU202000512

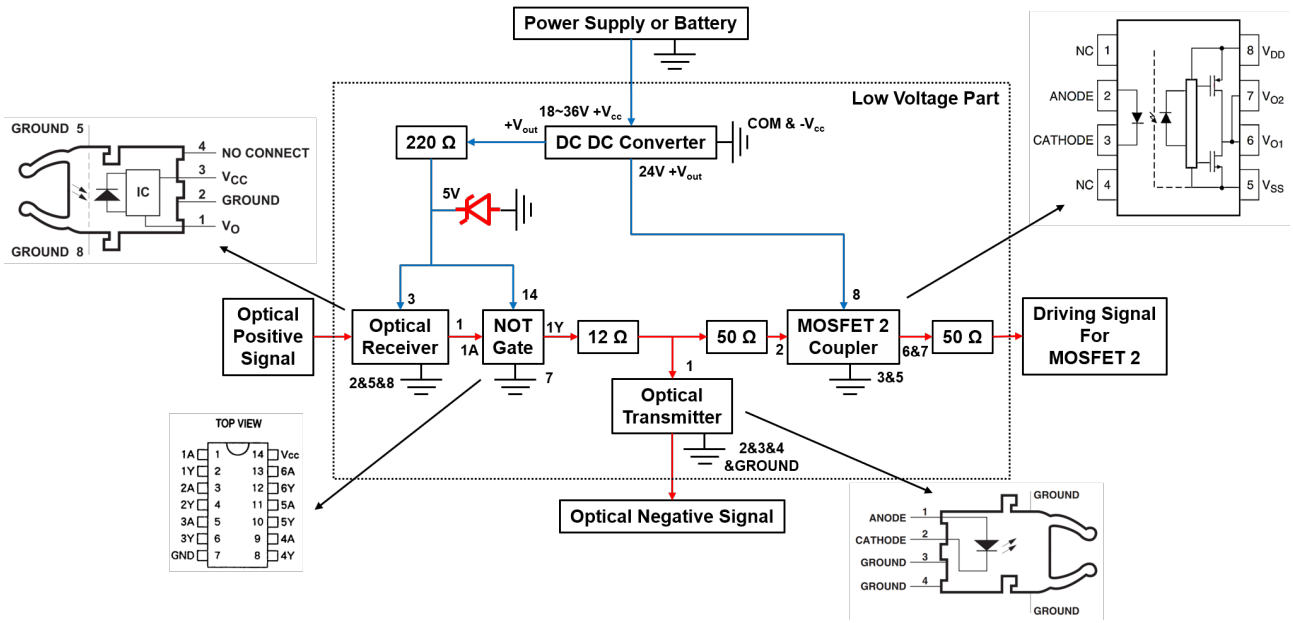

Figure 87: The Circuit diagram of low voltage part of MOSFET driver.

The input optical positive signal is connected to the optical receiver. The output optical negative signal is connected to the optical transmitter. The output driving signal for negative MOSFET is connected to the MOSFET coupler through a 50 Ω resistor.

doi:10.6844/NCKU202000512

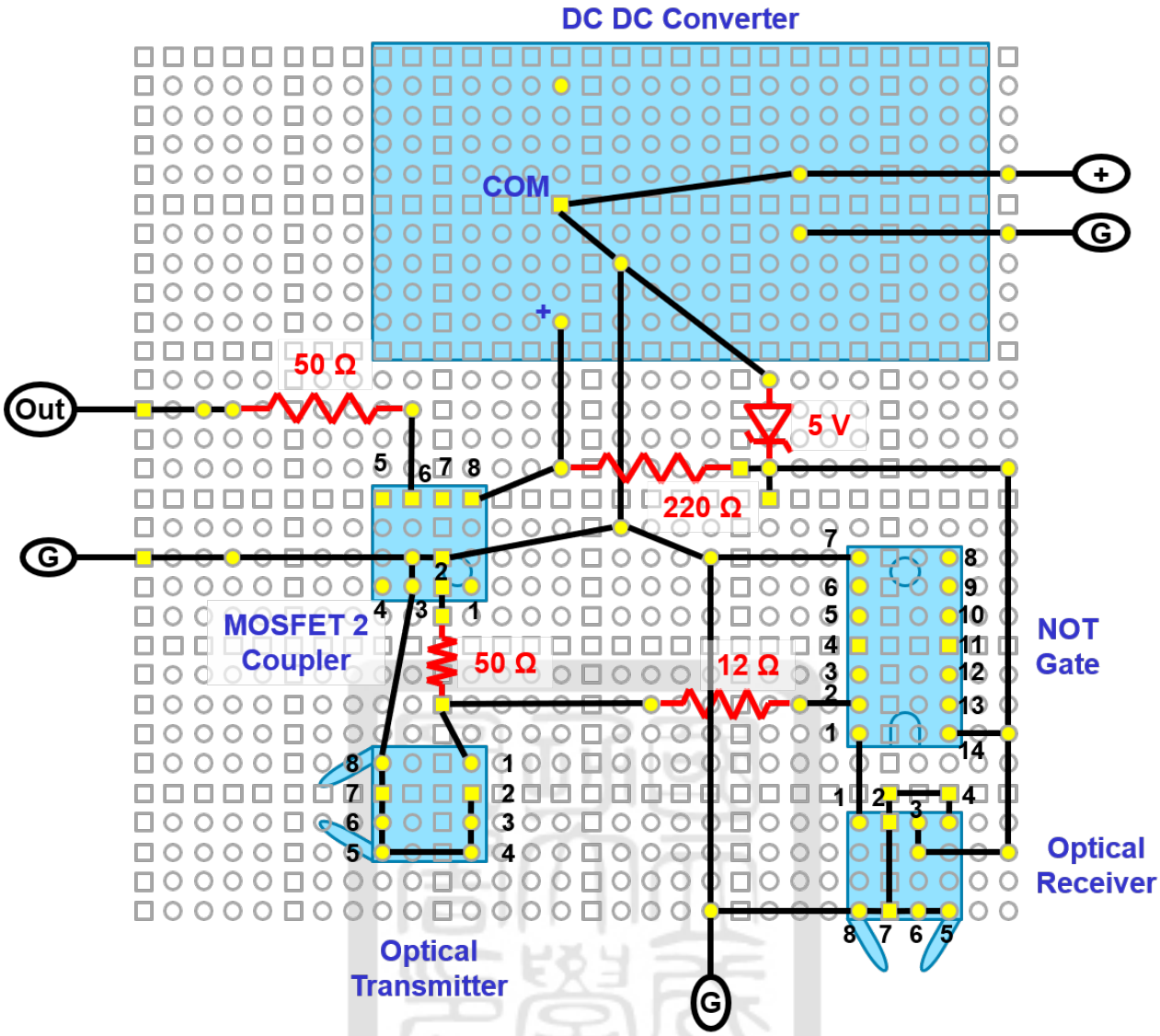

Figure 88: The Circuit layout of low voltage part of MOSFET driver.

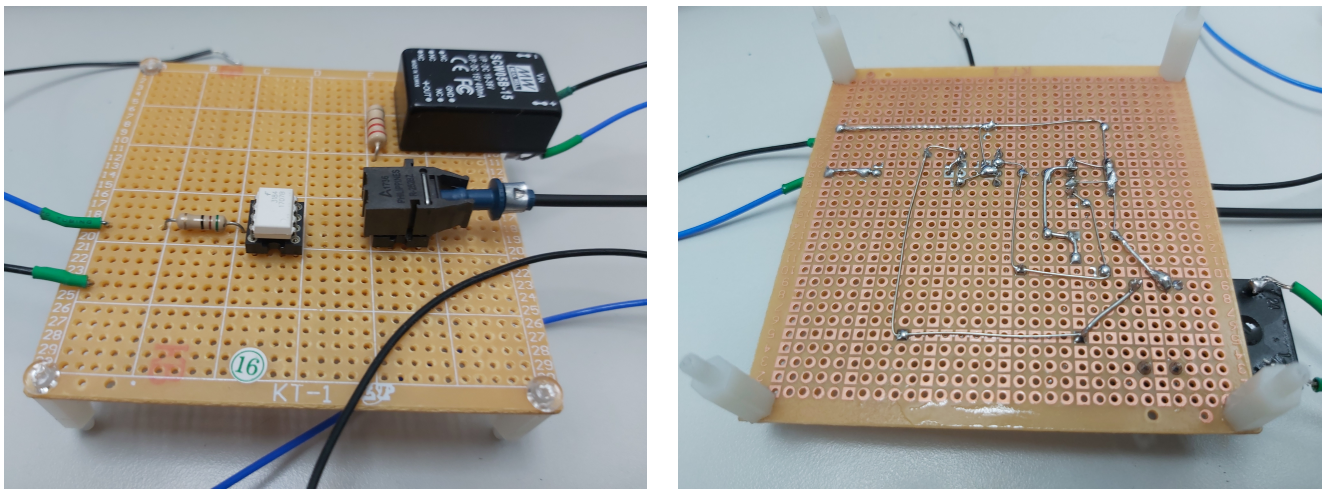

(a) (b)

Figure 89: The high voltage part of MOSFET driver. (a) Front view. (b) Back view.

doi:10.6844/NCKU202000512

The red note on the right shows the ground of the high voltage part is not connected to the general ground but it is connected to the output of the MCP driver which is shown in figure 93. The DC-DC converter has the input of 18 to 36 V and the output of 15 V. The high voltage and the ground are seperated by this DC-DC converter.

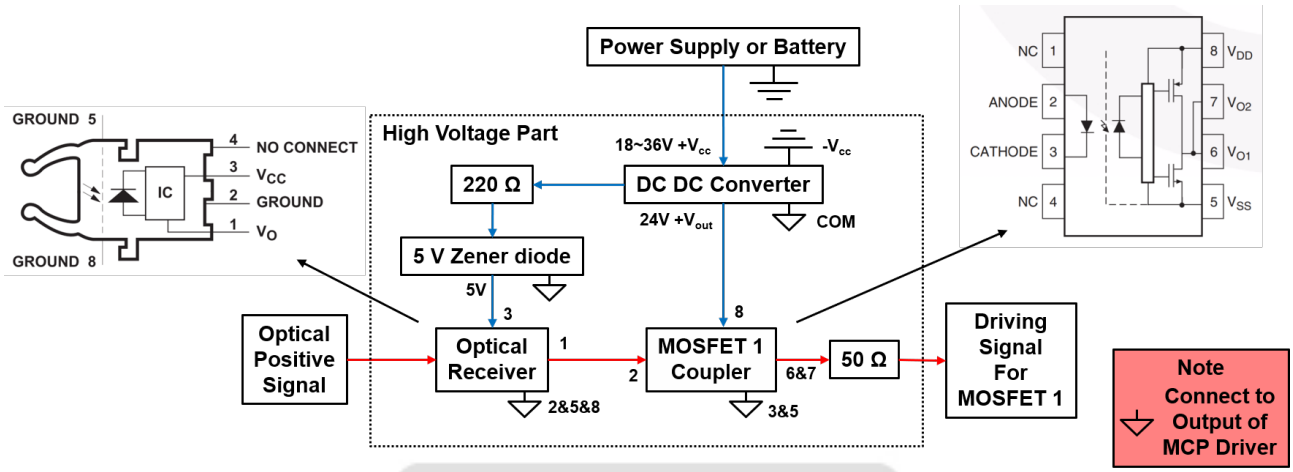

Figure 90: The Circuit diagram of high voltage part of MOSFET driver.

The input optical positive signal is connected to the optical receiver. The output driving signal for positive MOSFET is connected to the MOSFET coupler through a 50 Ω resistor.

doi:10.6844/NCKU202000512

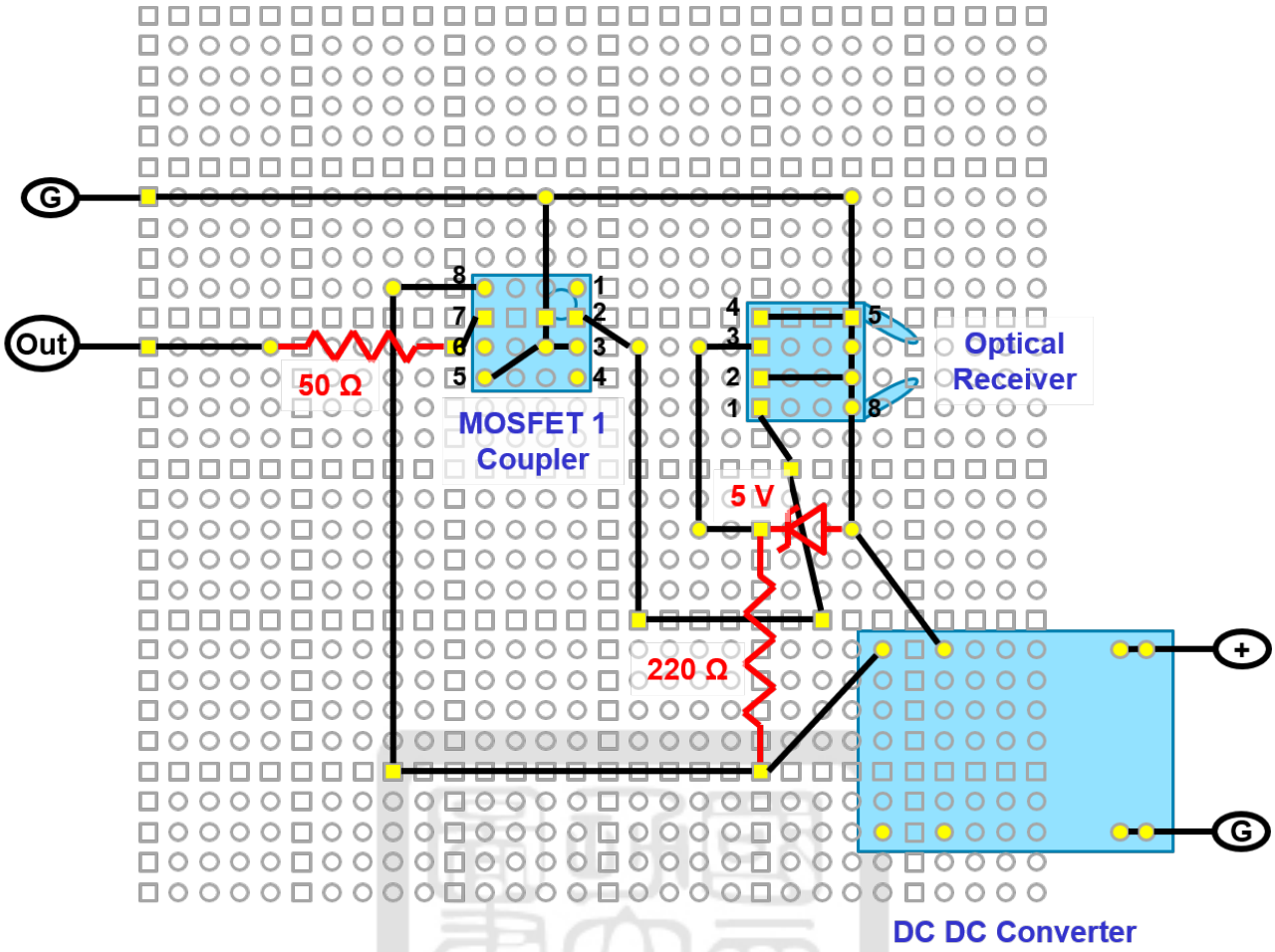

Figure 91: The Circuit layout of high voltage part of MOSFET driver.

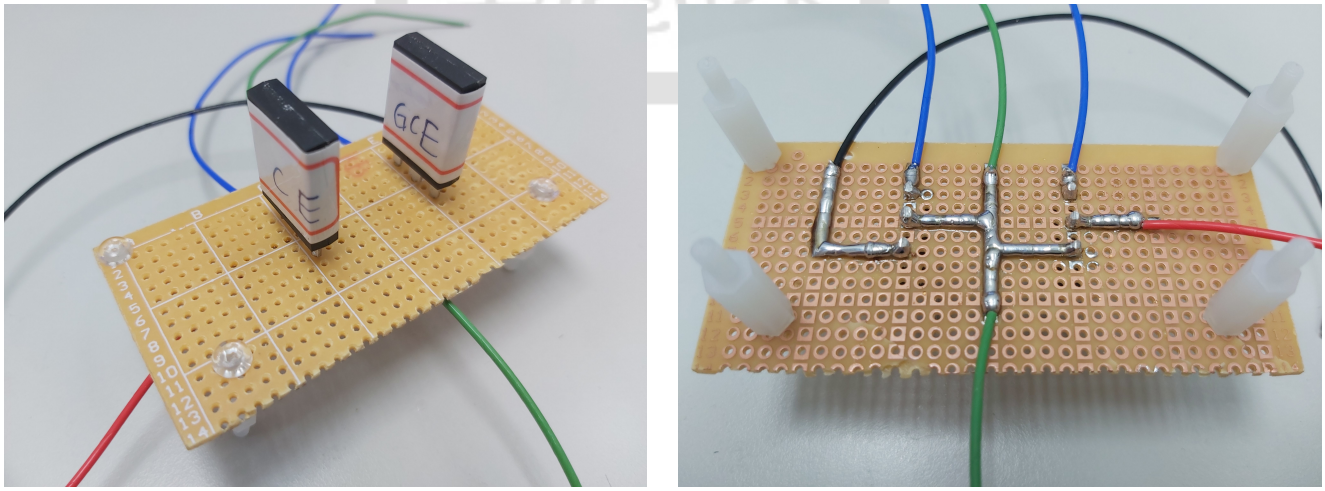

(a) (b)

Figure 92: The plate of MOSFETs. (a) front view. (b) back view.

The MCP driver output is also connected to the high voltage part.

doi:10.6844/NCKU202000512

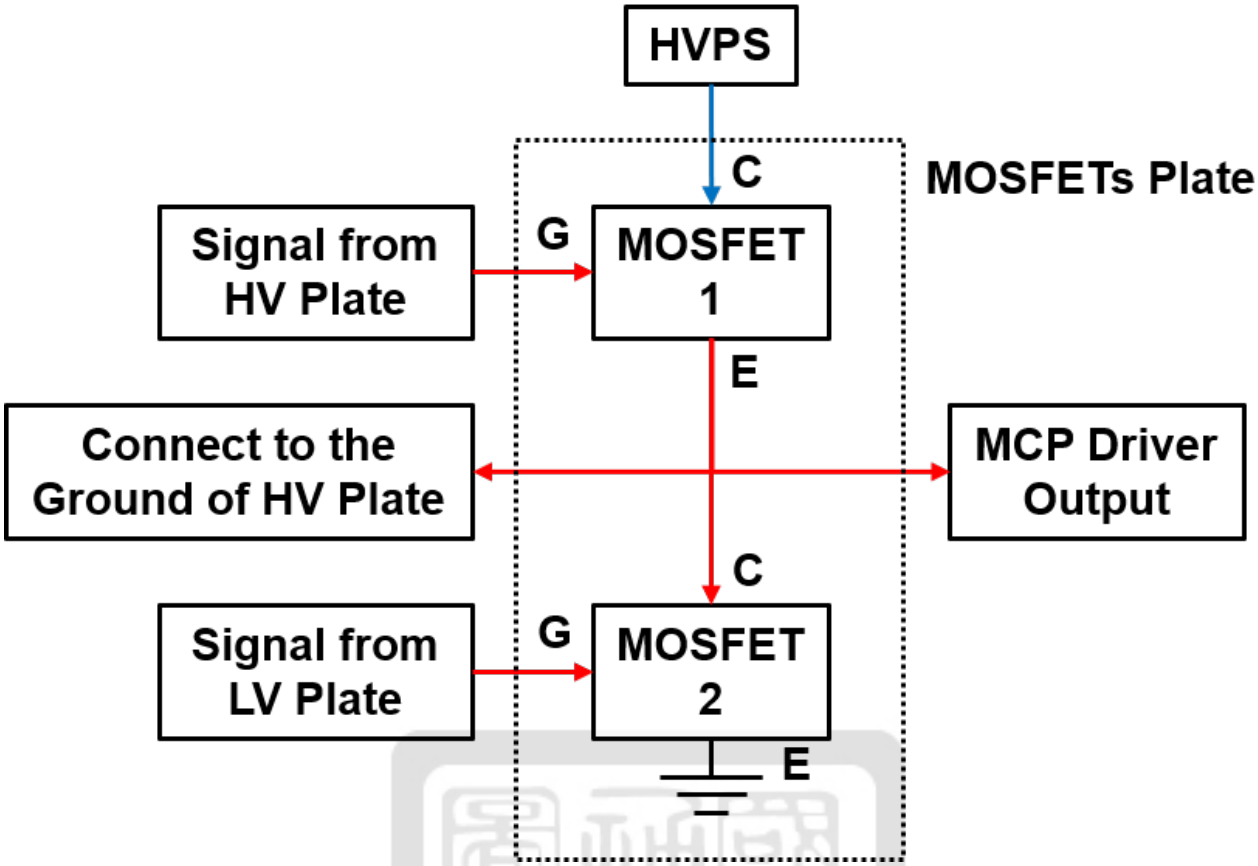

Figure 93: The circuit diagram of plate of MOSFETs.

doi:10.6844/NCKU202000512

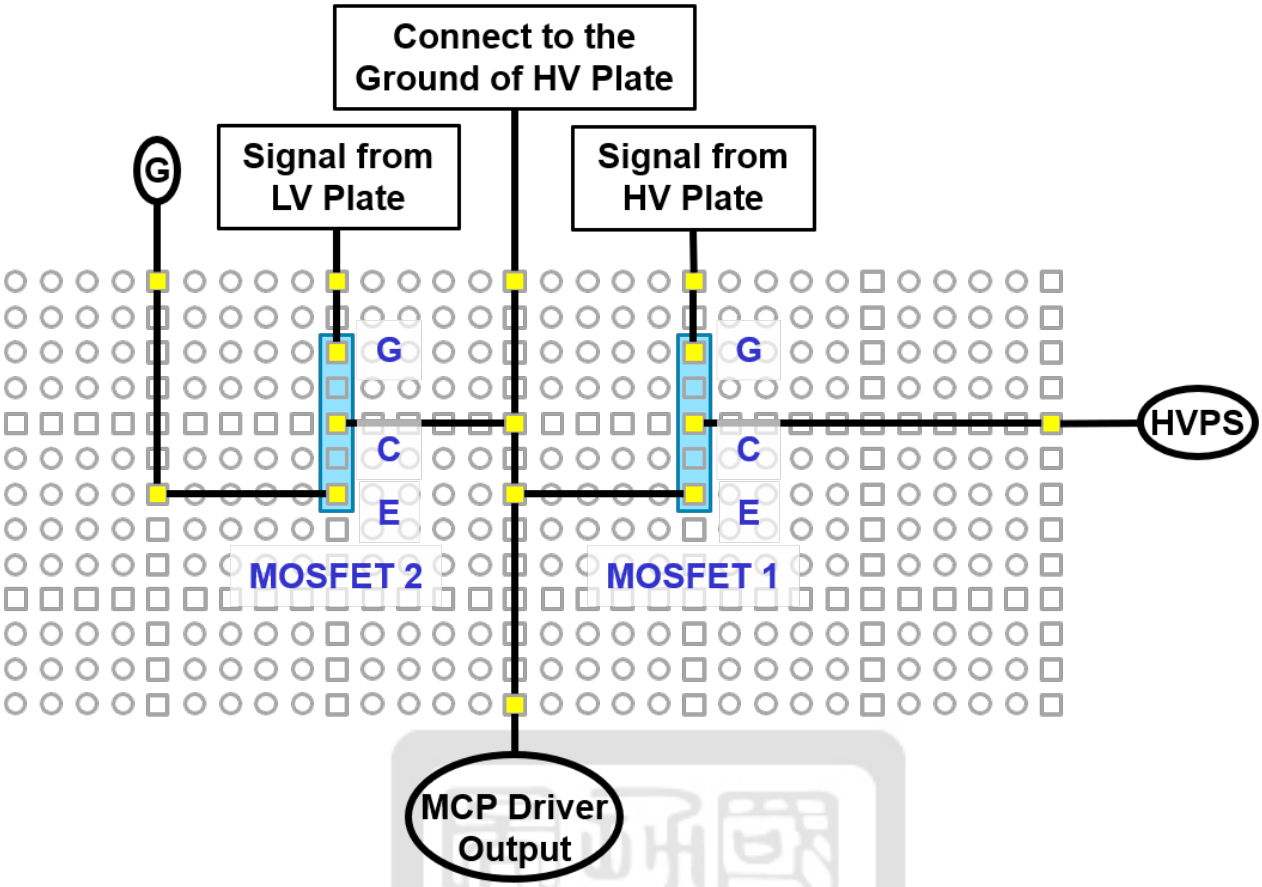

Figure 94: The circuit layout of plate of MOSFETs.

A.6 The venders of all components

Component	Vender	Note
Screws for PPCB system	鈺峰螺絲	
Vent screws for vacuum chamber	明利科技	
Polyimide tape	露天	keyword: 金手指膠帶 or 茶色絕緣膠帶
Alumium foil tape for Rogowski coil	蝦皮	keyword: 鋁箔膠帶
Electronic components (resistors, capacitors ...)	南一 or 美和	
O ring for vacuum chamber	金吉全	
ICs for pinhole camera controller	RS	use Po-Yu Chang's account
metal of conical-wire array	三川金屬	

doi:10.6844/NCKU202000512

A.6.1 Locations of the experimental data in the lab drive

The experimental data is located in /Shares/chieh/project in the lab drive. The information is separated by different sections in different directories. The directories are listed below:

- The information about chapter 3: the pulsed-power system is in the "Capacitor Discharge test" directory.
- The information about section 3.1.2: the rail-gap switch is in the "Marx generator" directory.
- The information about section 4.1: the Rogowski coil is in the "Rogowski coil" directory.
- The information about section 4.3: the x-ray pinhole camera is in the "MCP" directory.
- The information about chapter 5: plasma jet generations is in the "Conical Wire Array" directory.

The location of figures about the experimental data is shown in table 28.

doi:10.6844/NCKU202000512

Table 28: The location of figures about the experimental data.

Figure No.	Location (/Shares/chieh/project/...)
26	/Capacitor Discharge test/Before June /rail gap breakdown voltage/avgAndStd.xlsx
31, 32, 37, 51, 52	/Capacitor Discharge test/20190731_N-wing_capacitor_discharging_test /Data/T0030.CSV
33	/Capacitor Discharge test/20190731_N-wing_capacitor_discharging_test /Pick_up _coil_analysis.xlsx
35	/Capacitor Discharge test/20190812_N-wing_capacitor_discharging_Polishing /Data/T0000.CSV
36 (a)	/Capacitor Discharge test/20190731_N-wing_capacitor_discharging_test /Delay time and frequency.csv
36 (b)	/Capacitor Discharge test/20190812_N-wing_capacitor_discharging_Polishing /Delay time and frequency.csv
39, 41	/Capacitor Discharge test/20190827_1-1_Discharge_with_two_probe /data/T0000.CSV
40	/Capacitor Discharge test/20190906_3-3_Discharge_Test /data/T0000.CSV
43	/Capacitor Discharge test/20191002_5-5_Discharge_Test /Data/T0000.CSV
45	/Rogowski coil/2018073001_Rogowski_coil_ measurement_using_function_generator /10. programs/magnetic_flux_is_independent_to_current_position.pro
48 (b)	/Rogowski coil/2018073001_Rogowski_coil_ measurement_using_function_generator /3.input_and_output_voltage_in_phase_diagram_change_frequency_ from_100kHz_to_1000kHz_interval_50kHz_fixed_vpp_10V
48 (d)	/Rogowski coil/2018073001_Rogowski_coil_ measurement_using_function_generator /10. programs/relation_of_input_current_and_experiment_output_voltage.xlsx
59	/MCP/MCP Driver first IGBT Ground problem/Driver/ALL0001
60	/MCP/MCP Driver first IGBT Ground problem/Driver with IGBT/ALL0002
61	/MCP/20190701_MCP_Driver_IGBT_500V_testing/ALL0010
64	/MCP/20190701_MCP_Driver_MOSFET_1kV_testing/ALL0018
72, 73, 74, 75	/Conical Wire Array/wire width

doi:10.6844/NCKU202000512